Computations of Highly Nonlinear Free-Surface Flows, with Applications to Arbitrary and Complex Hull Forms

Anil K. Subramani

Department of Naval Architecture
and Marine Engineering

COMPUTATIONS OF HIGHLY NONLINEAR FREE-SURFACE FLOWS,
WITH APPLICATIONS TO ARBITRARY AND COMPLEX HULL FORMS

by

Anil Kumar Subramani

Department of Naval Architecture
and Marine Engineering
College of Engineering
The University of Michigan
Ann Arbor, MI 48109-2145

COMPUTATIONS OF HIGHLY NONLINEAR FREE-SURFACE FLOWS,
WITH APPLICATIONS TO ARBITRARY AND COMPLEX HULL FORMS

by

Anil Kumar Subramani

A dissertation submitted in partial fulfillment
of the requirements for the degree of
Doctor of Philosophy
(Naval Architecture and Marine Engineering
and Scientific Computing)
in The University of Michigan
2000

Doctoral Committee:

> Professor Robert F. Beck, Chair
> Professor Robert Krasny
> Assistant Professor Ana I. Sirviente
> Professor Armin W. Troesch

ABSTRACT

COMPUTATIONS OF HIGHLY NONLINEAR FREE-SURFACE FLOWS,
WITH APPLICATIONS TO ARBITRARY AND COMPLEX HULL FORMS

by

Anil Kumar Subramani

Chairperson: Robert F. Beck

Computations of highly nonlinear free-surface flows, such as around arbitrary and complex hull forms, are performed using a desingularized boundary integral method which had been previously limited to simple, mathematical body geometries. Ubiquitous as wave breaking and spray are in nonlinear ship flows, the development of the method has been accompanied by studies into wave breaking, especially on ways to enable the computations to proceed unhindered by the occurrence of spray and wave breaking.

A criterion for the likely occurrence of wave breaking is devised as a means for detecting incipient numerical wave breaking. Once detected, a breaking wave is suppressed though a new technique that simply fairs through the free-surface nodes that are seen as likely to break. The technique is successfully applied to gravity waves in two dimensions.

The feasibility of the technique in suppressing wave breaking in forward-speed calculations is shown using two-dimensional transom stern flow calculations, and grid convergence is also demonstrated. A stable procedure for effecting cleanly-separating

1

transom stern flow within the inviscid flow model is also devised using these two-dimensional calculations.

Calculations for practical hull forms are enabled by a body geometry processor for modeling such forms. Results are presented for arbitrary and complex hull forms as typified by the Series 60, C_B=0.6 parent hull and two transom-sterned vessels—the DDG5415 naval combatant model and the D1 fast monohull. Specifically, calm water results at representative Froude numbers are presented, grid convergence is shown, and the computed wave profile on the hull, wave field, and wave resistance are shown to agree well with the available experimental data. The calculations also feature the successful suppression of spray and wave breaking in three dimensions.

ACKNOWLEDGMENTS

I would like to acknowledge the efforts of those who aided in the carrying out of the research in this dissertation. Firstly, I would like to express sincere thanks to my research advisor, Prof. Robert F. Beck. I am glad to have had for an advisor someone who was not only very generous with his time when it was requested, but who also gave the necessary room for independent work. The path to the completion of this dissertation has undoubtedly been arduous, even if my trying experiences have merely been typical of most Ph.D. candidates. Given that, I also count myself fortunate to be able to remember my supervisor as, first and foremost, a truly good human being.

While my interactions with the other faculty members at the University of Michigan have naturally been on a much smaller scale, I am still thankful for the many positive influences. In particular, I would like to acknowledge the supportive roles of Profs. Marc Perlin, Ana Sirviente, Armin Troesch, Robert Krasny, Michael Bernitsas, Bram van Leer, and Peter Smereka. The staff members of the Department of Naval Architecture and Marine Engineering were always helpful; for that, I thank Celia Eidex, Cora Wheatley, Luella Miller, Kathy Stolaruk, Colleen Vogler, and Marilyn Siegel.

My doctoral education would be much less complete were it not for my interactions with fellow students. I owe thanks to Steve Scorpio for his early guidance and to Kunho Kim for kind help towards the end, and I cherish deeply my involvement with the American Society for Engineering Education student chapter. I am thankful to the College of Engineering and the Horace H. Rackham School of Graduate Studies for

TABLE OF CONTENTS

LIST OF FIGURES

ix

LIST OF APPENDICES

CHAPTER 1

INTRODUCTION

Ships are important to international trade and national defense, and they also play a significant role in recreational travel and coastal transport. Due to safety, performance, and fuel consumption considerations, each new design of a ship must necessarily be tested for its hydrodynamic characteristics. Such testing may be done—as has been traditionally done—in a towing tank, using scaled ship models. However, model testing is laborious, time-consuming, and expensive. Not only that, improvements in the techniques for the design of ships have been accompanied by an increase in the demand for improved and detailed analysis tools. Computational methods facilitate the design process greatly by enabling a speedy, detailed, and relatively inexpensive analysis of the near-field hydrodynamics of candidate hull forms. This is reflected in the large degree to which computational methods are being developed and extended for use in the testing of modern naval combatant designs.

The very use of numerical hydrodynamics tools in the design process is aided considerably by the availability of many, diverse solution methodologies, each with its own different strengths and drawbacks. The wide choice in methodologies probably owes most to two factors: the essential difficulty of ship hydrodynamic computations and the relentless increases in computational power over the last few decades. The latter is recognized widely; to elaborate on the former—

Ship hydrodynamic flows are complex, highly turbulent flows, with their computations requiring the resolution of a large range of length and time scales. While theoretically possible, a Direct Numerical Simulation of these flows requires computational resources to a degree that is not expected to become available even in the foreseeable future. Increasing efforts have been, instead, directed towards computational fluid dynamics (CFD) methods involving the solution of the incompressible Reynolds-averaged Navier-Stokes (RANS) equations and Large-Eddy Simulations. Progressing from calculations of ship stern boundary layers (Larsson et al., 1991), it has become feasible to solve with confidence (albeit at model-scale Reynolds number) for the steady-state free-surface flow around a ship advancing in calm water (CFD Workshop Tokyo, 1994; Gothenburg 2000). Recently, successful extensions have also been realized in the solution of the unsteady RANS equations for seakeeping problems (e.g., Gentaz et al., 1999)

However, a detailed solution of the entire flow field is often unnecessary. It can also be prohibitively expensive. Haussling et al., 1997, for example, required 400 hours on a CRAY C-90 supercomputer for a single steady-state calculation of the flow around a naval combatant model. Now, typical ship hydrodynamic flows involve Reynolds numbers on the order of 10^9, such that viscous effects are confined to a narrow boundary layer and the wake, rendering the bulk of the flow essentially irrotational. Recognizing the enormous simplifications that result, wide recourse has been taken to inviscid methods based on potential flow theory. In fact, these methods remain the dominant ones in the design process to this day. A potential flow calculation, it may be noted, is usually implemented within a boundary element formulation, which reduces the size of the problem by a whole dimension and is generally easier to solve.

Yet, even the reduction to potential flow leaves behind significant challenges because of the nonlinear nature of the free surface boundary conditions—which are to be solved on a boundary that is not known a priori—and the complex geometric features of typical marine vehicles. One additional difficulty common to most of the prevalent methodologies (due to inherent limitations in the mathematical model) lies in coping with wave breaking and spray, which are characteristic of highly nonlinear ship flows. For, even a fleeting occurrence of spray may cause a computation to terminate abruptly. The present research concerns advances made with a particular potential flow method: the solving of fully nonlinear free-surface flows for arbitrary and complex hull forms, including ways to deal with wave breaking.

Common potential flow problem formulations involve a linearization of the free-surface boundary conditions, because higher-order theories (those including the higher-order derivatives in the free-surface boundary conditions) are, understandably, more difficult to solve. Examples of the simpler theories include: in two dimensions—the so-called slender body theories; and in three dimensions—the Neumann-Kelvin, body exact, and Dawson methods. These theories have indeed given good results for some problems but have been shown to compare poorly with experimental results for many other problems. Their shortcomings led naturally to the consideration of the full nonlinearities in the free-surface boundary conditions.

Fully nonlinear potential flow computations are those involving an application of the complete free-surface boundary conditions and at the exact location of the free surface. Fully nonlinear computations may be performed in many ways. For steady forward speed problems, they may be performed by using an iterative technique to solve a series of linearized boundary value problems that are based on the solution to the previous iteration and which are satisfied on the deformed free surface and the exact

wetted surface of the body. Iterative techniques have been used successfully by, among others, Jensen et al. (1989), Kim and Lucas (1990, 1992), Raven (1992), and, more recently, Scullen and Tuck (1995) or Scullen (1998). These techniques have the likely advantage of converging to the fully nonlinear solution in less computer time than a time-stepped method; however, they cannot be extended easily to unsteady seakeeping problems.

A time-domain solution of the fully nonlinear water wave problem may be obtained using the Euler-Lagrange method, which was introduced by Longuet-Higgins and Cokelet (1976) in their study of two-dimensional water wave problems. This time-stepping method consists of two major tasks at each time step: In the Lagrange phase, individual nodes on the free surface are tracked by integrating the nonlinear free surface conditions with respect to time, while in the Euler phase a mixed boundary value problem is solved to obtain the fluid velocities that in turn are needed in the time integration of the free surface boundary conditions.

Variations of the Euler-Lagrange method have been applied to a wide variety of two- and three-dimensional problems. The applications to two-dimensional problems include Faltinsen (1977), Vinje and Brevig (1981), Baker et al. (1982), Grosenbaugh and Yeung (1988), Schultz and Hong (1989), Cointe et al. (1990), Sen (1993), and Greaves et al. (1997). Three-dimensional computations have been performed by, among others, Lin et al. (1984), Dommermuth (1987), Kang and Gong (1990), Zhou and Gu (1990), Cao et al. (1991, 1993), Park and Troesch (1992), Chan and Calisal (1993), Xu and Yue (1992), DiMascio et al. (1994), Wu and Eatock-Taylor (1996), Wu et al. (1996), and Celebi et al. (1998). However, the variations arise primarily from differences in the time-integration schemes used and in the techniques used to solve the resulting mixed boundary value problem at each time step. The vast majority of results have been obtained for

applications limited to mathematical body geometries such as cylinders, spheroids, and the Wigley hull, or for water wave problems with no body at all.

At the University of Michigan, a multipole-accelerated desingularized boundary integral method—denominated UM-DELTA, for University of Michigan Desingularized Euler-Lagrange Time-Domain Approach—has been developed over the last decade to solve fully nonlinear water-wave problems including wave loads on offshore structures and nonlinear ship motions. The development of the UM-DELTA method was recently chronicled by Beck (1998). As previously indicated, in this method the fluid is assumed incompressible, inviscid and started from rest so that the resultant flow is irrotational and governed by the Laplace equation for the velocity potential.

The velocity potential is constructed by singularities distributed on auxiliary surfaces separated from the problem boundaries (hence, 'desingularized') and outside the flow domain—'above' the free surface, 'inside' the body surface, and 'outside' the appropriate boundaries at infinity. The strengths of the singularities are determined so that the boundary conditions are satisfied at chosen collocation points or nodes. To ensure the convergence of the method, the desingularization distance decreases as the computational grid becomes finer. Because of the desingularization, the resulting kernel in the integral equation is nonsingular; therefore, special care is not required to evaluate integrals over the panels. Simple numerical quadratures can be used to reduce the computational effort greatly. Further, simple isolated Rankine sources may be used, allowing the direct computation of the induced velocities in the fluid without further numerical integration or differentiation. The solution is advanced in time using the Euler-Lagrange time-stepping procedure and the body position and surface normal velocities are updated from the equations of motion of the vessel.

Recent extensions to the method, leading into the current research, have included the implementation of multipole acceleration techniques (Scorpio et al., 1996). The underlying idea of multipole acceleration is that the potential due to a group of sources may be evaluated at distant points by first accumulating the influences into a single multipole expansion. By a complementary arrangement of the evaluation points into groups, the accumulated multipole expansions may be transformed into local expansions centered on each group. Using a tree-structured hierarchy of source groups and evaluation point groups, the normally $O(N^2)$ process of evaluating the influence of N sources at N points is reduced to an $O(N)$ process with only an $O(N)$ storage requirement. This leads to substantial reductions in computational time and storage, enabling the simulations to be performed on high-end workstations. However, because of the extensive requirements for logical branching, multipole acceleration disrupts the high degree of vectorization inherent in the UM-DELTA code and is not, therefore, invoked on vector supercomputers such as the CRAY C-90.

The UM-DELTA method has been successfully applied to a wide variety of problems. These include: the generation of shallow water solitons (Cao et al., 1993); wave resistance, added mass, and damping and exciting forces on a Wigley hull (Beck et al., 1994); and wave loads on a vertical cylinder (Scorpio and Beck, 1998). However, the applications had, until recently, been limited to simplified body shapes such as spheroids, cylinders, and parabolic hull forms—body shapes that could be represented mathematically.

An accurate and efficient modeling of the geometry is not a trivial task within UM-DELTA. Unlike panel methods that use flat quadrilateral panels to define the surface and the unit normal, UM-DELTA needs to be able to determine the surface location and unit normals at arbitrary node locations on the body. Determining the

surface location and unit normal at arbitrary locations on a typical ship hull has been difficult, and it has served as a hurdle in the extension of the method to arbitrary hulls. Nevertheless, one such extension was carried out by Celebi and Beck (1997), who used a NURBS (Non-Uniform Rational B-Spline) surface representation of the body surface and a variational adaptive curve grid generation method for node placement on the body. The use of this technique, when tested on the parabolic Wigley hull modified with the inclusion of bow and stern rakes, resulted in a 40% increase in CPU time when compared to a calculation that used instead the mathematical representation of the hull. Considering that the computational burden would only increase for ships with complex features such as bulbous bows and skegs, which may require more than a single NURBS surface to represent the hull surface effectively, the NURBS technique was not pursued further.

Instead, the development of a faster and more robust hull-surface processor was separately initiated (Beck, 1998) and subsequently incorporated into the UM-DELTA code along with other improvements. These have enabled free-surface flow computations for realistic hull forms incorporating raked bows and sterns and bulbous bows (as presented in Subramani et al., 1998b) and also for transom-sterned naval combatants. The computation of smoothly-separating transom flow in three dimensions has followed the approach of Scorpio and Beck (1997), who used the UM-DELTA method to investigate two-dimensional inviscid transom stern flow.

Motivated by the ubiquitous nature of wave breaking in nonlinear ship flows and the disruptive nature of wave breaking in computations, the above developments have been accompanied by studies into wave breaking. Improving upon previous related efforts—notably, Haussling and Coleman (1979) and Wang et al. (1994)—a new technique was devised to detect and to suppress the likely incidence of numerical wave

breaking. This technique, as presented in Subramani et al. (1998a) and Subramani and Beck (2000), has been successfully tested for gravity waves in two and three dimensions, while including forward speed effects.

This dissertation describes the recent developments of the UM-DELTA method on its way to becoming a useful tool for the seakeeping analysis of modern naval combatant designs, while also describing ways to handle the inherent difficulty of wave breaking.

The problem formulation and solution methodology are presented in Chapter 2. Chapter 3 discusses the wave breaking problem and the recent efforts to handle wave breaking in the computations. Chapter 4 covers a study of two-dimensional transom stern computations, as a prelude to that of the three-dimensional computations. This chapter also features an application of the wave-breaking suppression technique to forward speed computations. In chapter 5, the hull-surface processor is described and results of the fully nonlinear calculations for arbitrary and complex hull forms are presented. Specifically, calm-water results at representative Froude numbers are presented for the Series 60, $C_B = 0.6$ parent hull (typifying arbitrary hull forms) and for two transom-sterned vessels—the D1 fast monohull and the DDG5415 combatant (which also has a bulbous bow). The calculations are verified through grid convergence and also compared with the available experimental data. Finally, in chapter 6, concluding remarks are made and future work is discussed.

CHAPTER 2

PROBLEM FORMULATION AND SOLUTION METHODOLOGY

Consider a vessel floating on a free surface and translating with speed $U_o(t)$ in the negative x-direction with respect to a right-handed space-fixed coordinate system. The problem set-up is shown in figure 2.1. For the (x, y, z) system translating with the body, the z=0 plane coincides with the load water line and defines the calm water level, with +z directed upward and the x-z plane coincident with the centerplane of the vessel.
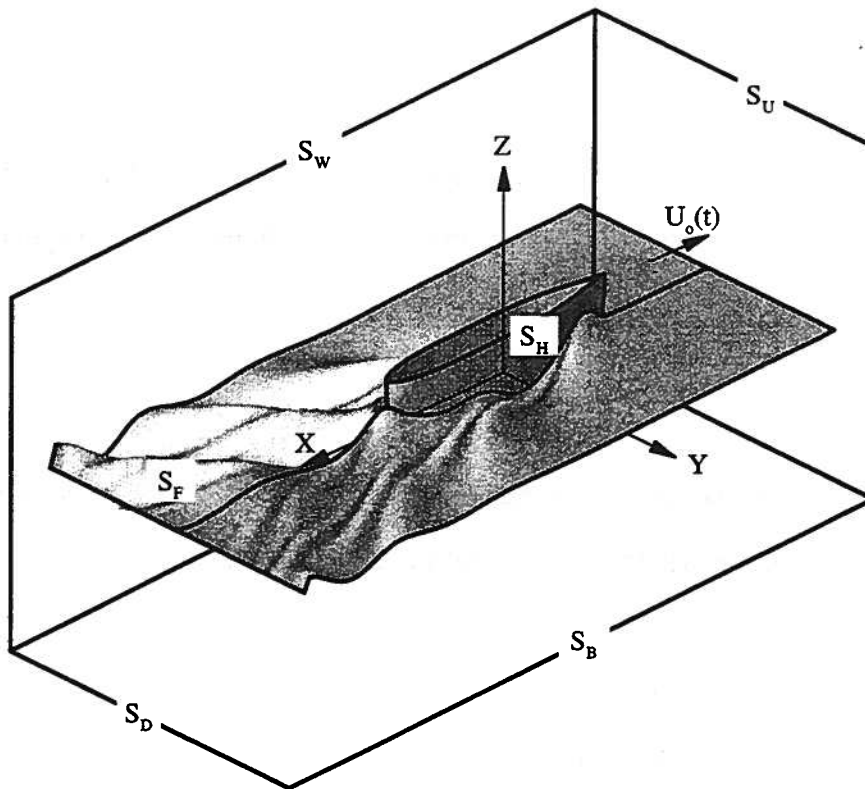
Figure 2.1: Problem set-up

2.1 Problem Formulation

Assuming the fluid to be incompressible, inviscid, and started from rest, the resultant flow is irrotational and governed by the Laplace equation for the velocity potential. The total velocity potential describing the fluid motion is then

$$\Phi(x, y, z, t) = U_o(t)x + \phi(x, y, z, t) \tag{2.1}$$

where $U_o(t)x$ is the potential due to the free-stream velocity and $\phi(x,y,z,t)$ is the perturbation potential. In the fluid domain, both potentials Φ and ϕ satisfy Laplace's equation,

$$\nabla^2 \Phi = 0 \tag{2.2}$$

In order to define a well-posed problem, initial conditions and boundary conditions on all surfaces surrounding the fluid domain must be specified.

2.1.1 Initial Conditions

With the problem started from rest, the initial values of the potential and free surface are specified to be as follows in the fluid domain:

$$\phi = 0 \quad t \le 0 \tag{2.3}$$
$$\eta = 0 \quad t \le 0$$

2.1.2 Boundary Conditions

On the body wetted surface (S_H) and on the bottom (S_B), the boundary conditions are:

$$\frac{\partial \phi}{\partial n} = -U_o n_1 + \bar{n} \cdot \bar{V}_H \quad \text{on } S_H \tag{2.4}$$

and

$$\frac{\partial \phi}{\partial n} = -U_o n_1 + \bar{V}_B \cdot \bar{n} \quad \text{on } S_B \tag{2.5}$$

where $\bar{n} = (n_1, n_2, n_3)$ is the unit normal out of the fluid and $\bar{V}_H$ is the local velocity—including rotational effects—of points on the body and $\bar{V}_B$ is the velocity of the bottom relative to the $0(x,y,z)$ system. Because we are solving an initial value problem, the boundary condition on the surface at infinity (S_∞) is

$$\nabla \phi \rightarrow 0 \quad \text{as} \quad |x^2 + y^2| \rightarrow \infty \tag{2.6}$$

Other far field boundary conditions are possible; for example, incident waves may be prescribed at the upstream boundary (S_U). The boundary condition on an outer wall (S_W) aligned with the free-stream direction will have the form:

$$\frac{\partial \phi}{\partial y} = 0 \quad \text{on } S_{WALL} \tag{2.7}$$

Downstream, an absorbing beach may be used; although, for forward speed problems, an open boundary condition is often used.

The kinematic and dynamic free surface boundary conditions are prescribed on the free surface (S_F), although they are numerically implemented in a special form for an improved description of the free surface as the solution evolves. In this form, the free-surface nodes are prescribed to move, along pre-ordained tracks, with velocities chosen so as to minimize the inaccuracies that may result from errors in the computation of the spatial free-surface derivatives. See Beck et al. (1994) for details. The kinematic condition is written as

$$\frac{\delta\eta}{\delta t} = \frac{\partial\phi}{\partial z} - (\nabla\phi - \bar{v})\cdot\nabla\eta - U_o(t)\frac{\partial\eta}{\partial x} \qquad (2.8)$$

where

$$\frac{\delta}{\delta t} = \frac{\partial}{\partial t} + \bar{v}\cdot\nabla \qquad (2.9)$$

$z=\eta(x,y,t)$ is the free-surface elevation, and $\bar{v} = (v_x(t), v_y(t), \delta\eta/\delta t)$ is the velocity with which the free-surface nodes are prescribed to move; the dynamic condition is

$$\frac{\delta\phi}{\delta t} = -g\eta - \frac{1}{2}\nabla\phi\cdot\nabla\phi + \bar{v}\cdot\nabla\phi - \frac{P_a}{\rho} - U_o\frac{\partial\phi}{\partial x} \qquad (2.10)$$

where ρ is the fluid density, g, the gravitational acceleration, and P_a, the atmospheric pressure.

It becomes important to ensure that the free-surface nodes remain on their prescribed tracks as they convect downstream in the numerical tank (even if they are

regridded back to their original x-locations at the end of a full time step). This is done by determining the component velocities of $\bar{v}$ along the track and having the free-surface nodes move according to these component velocities. This treatment is detailed in Appendix A. Also, as evident from equation (2.8), an accurate computation of the spatial free-surface derivatives , $\nabla\eta$ is important for an accurate time stepping of the free-surface elevation. Improvements were made in the numerical estimation of $\nabla\eta$; the way in which the free-surface derivatives are computed is described in Appendix B.

The pressure on the body can be computed at each time step using a form of Bernoulli's equation that accounts for body motion:

$$\frac{p}{\rho} = -\frac{\hat{\partial}\phi}{\hat{\partial}t} - gz - \frac{1}{2}\nabla\phi\cdot\nabla\phi + \bar{V}_H\cdot\nabla\phi - U_o\frac{\partial\phi}{\partial x} \qquad (2.11)$$

where

$$\frac{\hat{\partial}\phi}{\hat{\partial}t} = \frac{\partial\phi}{\partial t} + \bar{V}_H\cdot\nabla\phi \qquad (2.12)$$

Forces and moments on the body can be computed by integrating the pressure over the body surface:

$$\bar{F} = \iint_{S_H} p\bar{n}\,ds \qquad (2.13)$$

$$\bar{M} = \iint_{S_H} p(\bar{r}\times\bar{n})\,ds \qquad (2.14)$$

where $\bar{n}$ is the unit normal pointing out of the fluid and into the body.

2.2   Solution Methodology

2.2.1   Euler-Lagrange Time-Stepping Procedure

A solution to the above nonlinear initial boundary value problem is obtained using the Euler-Lagrange time-stepping procedure introduced by Longuet-Higgins and Cokelet (1976). The solution procedure consists of repeatedly performing the following two steps:

(1)   Solving the linear mixed boundary value problem for the perturbation potential at a fixed instant in time

(2)   Stepping the nonlinear free-surface boundary conditions forward in time

The linear mixed boundary value problem is solved using a desingularized boundary integral method. The body position and surface normal velocities are updated from the equations of motion of the vessel.

2.2.2   Desingularized Method

In the desingularized method (Cao et al., 1991), Rankine sources are distributed on an integration surface (Ω) that is offset from the physical problem boundary by a small distance. The potential anywhere in the fluid domain can then be calculated by integrating the influences of all the sources:

$$\phi(\bar{x}_c) = \iint_\Omega \sigma(\bar{x}_s)G(\bar{x}_c;\bar{x}_s)d\Omega \tag{2.15}$$

where $\bar{x}_c$ is a point in the fluid domain, $\bar{x}_s$ is a point on the integration surface, $\sigma(\bar{x}_s)$ is the strength of the source located at $\bar{x}_s$, and $G(\bar{x}_c; \bar{x}_s)$ is the Rankine source Green function. The Green function for three-dimensional problems is

$$G(\bar{x}_c; \bar{x}_s) = \frac{1}{|\bar{x}_c - \bar{x}_s|} \qquad (2.16)$$

An application of the appropriate Dirichlet and Neumann boundary conditions to (2.15) yields the integral equations that must be solved for the unknown source strength $\sigma(\bar{x}_s)$ at each time step:

$$\iint_\Omega \sigma(\bar{x}_s) G(\bar{x}_c; \bar{x}_s) d\Omega = \phi_p(\bar{x}_c) \qquad , \bar{x}_c \in \Gamma_D \qquad (2.17)$$

$$\iint_\Omega \sigma(\bar{x}_s) \frac{\partial}{\partial n_{\bar{x}_c}} G(\bar{x}_c; \bar{x}_s) d\Omega = \chi(\bar{x}_c) \qquad , \bar{x}_c \in \Gamma_N \qquad (2.18)$$

where ϕ_p is the given potential at $\bar{x}_c$, Γ_D is the boundary on which ϕ_p is known, χ is the given normal velocity on the solid boundaries, and Γ_N are surfaces on which χ is known. For isolated sources, the above integral equations become simple summations; when discretized over a total of N collocation points $(\bar{x}_c)$, they result in an NxN linear system of the form

$$\sum_{j=1}^{N} A_{ij} \sigma_j = b_i, \quad i = 1 \text{ to } N \qquad (2.19)$$

where: the influence matrix $A_{ij} = G_{ij} = \dfrac{1}{\left| \bar{x}_{c_i} - \bar{x}_{s_j} \right|}$ for collocation points on the

free surface and $A_{ij} = \bar{n}_i \cdot \nabla_{\bar{x}_i} G_{ij}$ for collocation points on solid boundaries; σ_j is the

vector of unknown source strengths; and b_i is the vector of boundary conditions—

$b_i = \phi_{p_i}$ for boundaries on which the Dirichlet condition is prescribed (e.g., the free

surface), $b_i = -U_o n_{1_i} + \bar{n}_i \cdot \bar{V}_H$ on the body surface, and $b_i = 0$ on a flat bottom. A

variety of options have been exercised for the solution of this system of equations. These

are the use of LU decomposition for the smallest problems (mostly two-dimensional); the

use of the iterative solver, GMRES (Saad and Schultz, 1986), for larger (three-

dimensional, especially) problems; and, more recently, the incorporation of multipole

acceleration techniques (Scorpio et al., 1998) to reduce the computational burden to

O(N).

Once the integral equations are solved for σ_j, hence $\phi(\bar{x}_c)$, the fluid velocities

can be found using

$$\nabla \phi_{\bar{x}_{cj}} = \sum_{j=1}^{N} \sigma_j \nabla_{\bar{x}_{cj}} G_{ij} , \qquad\qquad (2.20)$$

without the need for numerical derivatives.

Finally, the free surface boundary conditions, (2.8) and (2.10), are integrated in

time using the fourth-order Runge-Kutta method to obtain new values of $\phi(\bar{x}_c)$ and

$\eta(\bar{x}_c)$, and the cycle is repeated. A steady-state solution is obtained by accelerating the

vessel from rest up to steady forward speed.

CHAPTER 3

BREAKING-WAVE DAMPER

A major challenge for the UM-DELTA method has been the finding of ways to cope with breaking waves and spray in the fully nonlinear computations. In linear or higher-order expansion methods, the wave amplitudes can get unrealistically large without causing numerical difficulties. In fully nonlinear computations, however, wave breaking or spray formation at the body–free-surface intersection will cause the computations to stop promptly even though the difficulty may be confined to a small area (e.g., a breaking bow wave). This is illustrated in figure 3.1, which shows the time history of the surface displacement in a numerical simulation, using a two-dimensional variation of UM-DELTA, of shallow-water waves generated by a piston wave maker in a wave tank. The simulation corresponds to a physical experiment conducted at the University of Oslo by Grue et al. (1993). The calculations cease at about t=11.4 due to the occurrence (consistent with the physical experiment) of a breaking wave caused by the coalescing of waves of different frequencies.

Motivated by the desire to prevent even a fleeting occurrence of spray and breaking waves from curtailing the numerical simulations, a variety of artifices have been formulated in order to overcome this difficulty. Examples, prior to the current research, include the works of Haussling and Coleman (1979) and Wang et al. (1994). These approaches consist essentially of two parts, which shall be discussed in more detail in the sections to follow:

(1)   Detecting the likely incidence of wave breaking, and then

17

(2)   Controlling the wave breaking locally

Distance along tank
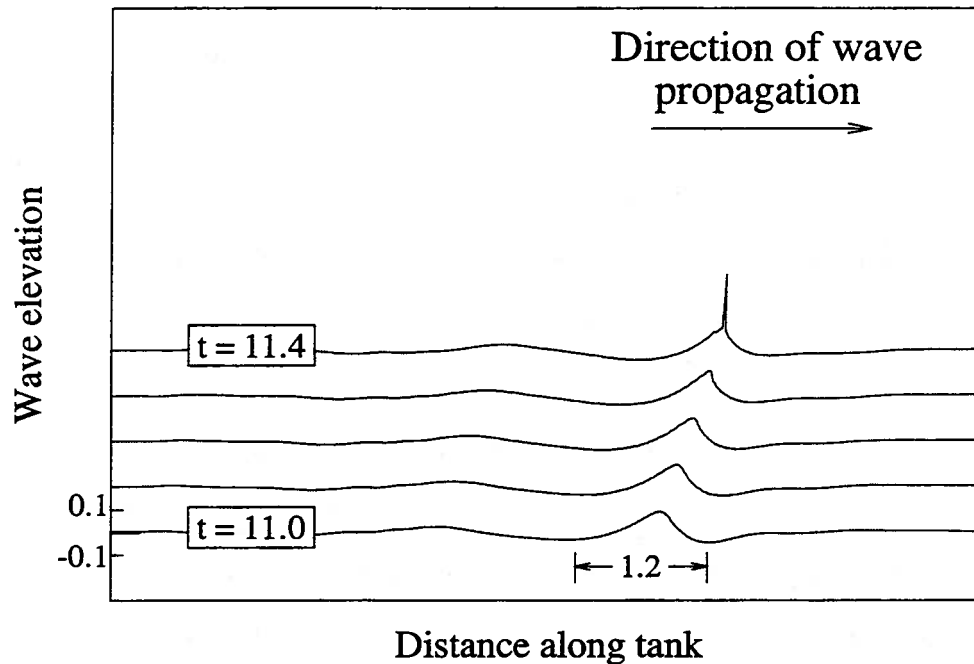
Figure 3.1: Time-history of the surface displacement in a numerical simulation, using UM-DELTA, of shallow water waves generated by a piston wave-maker in a two-dimensional wave tank.

3.1   Criterion for Wave Breaking

Important as the problem is, wave breaking has received considerable attention—in fields ranging from offshore hydrodynamics to chemical engineering. However, it has yet to be understood completely. A survey of the literature reveals that a number of studies have been conducted to understand why waves break and to determine a reliable criterion for the inception of wave breaking. See, e.g., Griffin et al. (1994) for a detailed review of some of the existing criteria.

Following Stokes' theorizing of a limiting height (H) to a wave in terms of the
wavelength (λ), the wave steepness (often measured by ak, where a is the wave
amplitude and $k=2\pi/\lambda$ is the wave number) has been the most commonly examined index
for wave breaking. Empirical data, however, show the steepness to be an imprecise
criterion—see figure 1 and table 1 of Griffin et al. (1994), which indicate that waves
break at lower steepnesses than that suggested by Stokes' criterion and also show the
scatter in the data. Another widely pursued idea has been the prescribing of a limiting
value to the fluid velocity at a crest. For example, Wang et al. (1994) provided data
obtained from a two-dimensional numerical wave tank in support of the criterion that a
wave breaks when the horizontal particle velocity reaches the local group velocity. The
possibility of breaking has also been related, by others, to the energy content in the
waves, but these last two criteria are difficult to extend to three-dimensional flows.

Criteria based on the wave slope and accelerations of the free surface have also
been suggested, but the consensus is that none of the above constitutes a simple, precise,
and universally valid criterion. In this light, we pursued (as reported in Subramani et al.,
1998a) a criterion based on the wave steepness because of its simplicity and its
applicability in three dimensions.

A steepness criterion that requires an estimate of the local wavelength, however,
is not easy to implement, especially when waves of different frequencies are present and
interact. We exploit, instead, that when waves break—or are about to break—they attain
a profile with a sharp crest of infinite curvature (κ). Furthermore, empirical studies of
steep but non-breaking regular waves indicate that waves that do not possess a sharp crest
obey the approximate non-dimensional bound, $|\kappa\lambda| \leq 6$. Figure 3.2 depicts how this
applies to waves of steepness, $H/\lambda \approx 1/12$, whose leading front went on to break. In the

figure is presented a representative snapshot (at t=18.8) of the surface displacement and

the curvature of the surface, for waves generated by a wedge wave maker of motion

amplitude 0.12m and frequency 0.559Hz (nominal λ=5m). The leading wave front broke

at about t=23.3 in the simulation. We seek, therefore, to use the exceeding of this

bound—as when any wave steepens to a sharp crest—as a "trigger" for the activation of a

localized wave damper in the fully nonlinear computations. This would also be an

improvement over the Stokes steepness criterion in the sense that the latter is an average

of the steepness over one wavelength. In wave breaking, it is the local steepness—as

measured through the present approach—that is of greater relevance.
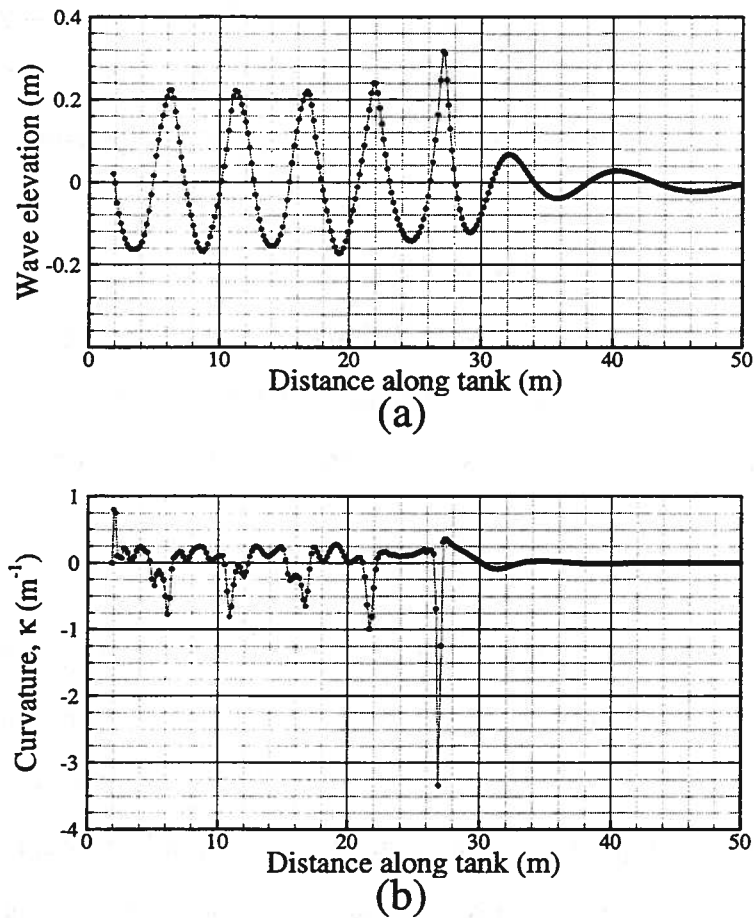
Figure 3.2: Representative snapshot of: (a) the surface displacement and (b) the curvature

of the surface, for waves as generated by a wedge wave-maker in a two-dimensional tank

To implement the idea, we then proceed to reformulate the steepness criterion in terms of a limiting value of κa: Adopting the approximate criterion that a wave breaks when its steepness, H/λ exceeds $1/12$ and using the above bound on $|\kappa\lambda|$, we obtain the condition, $|\kappa H| \leq 0.5$ for a wave not to break. We convert this into one based on κa since the crest-to-trough wave height is not as easily available. We do so on the basis of the observable geometric property of incipient breaking waves that $a \approx 0.7H$ on an average (e.g., Bonmarin, 1989), obtaining, finally, $|\kappa a| \leq 0.35$.

In order to examine the reliability of this curvature-based criterion, regular, deep-water gravity waves of varying steepnesses (as generated in a two-dimensional wave tank by a wedge wave maker) were simulated, and the variation of $|\kappa a|$ with the steepness, ak was noted. This variation is depicted in figure 3.3; for comparison, that for a second-order Stokes wave is also presented. Note that, in the evaluation of the abscissas, the nominal wave number given by $k = \omega^2/g$ was used.
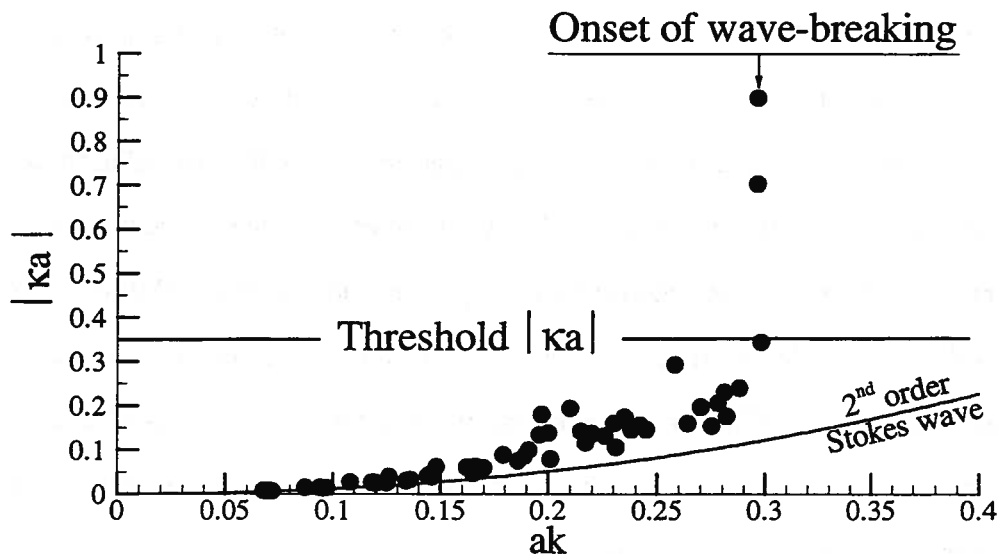
Figure 3.3: Observed variation with wave steepness, ak, of the wave-breaking index, |κa|, for regular, deep-water gravity waves

Although some of the scatter in figure 3.3 is due to the non-uniformities in fully nonlinear waveforms, it is largely due to the inevitable noise in the numerical evaluation of the curvature. The curvature is computed using a local three-point formula arising from the fitting of a circle through three consecutive free-surface nodes, as detailed in Appendix C. This formula, when implemented in double-precision arithmetic, gives results that agree closely with the analytically obtained curvatures for smoother profiles. This is shown in figure 3.4, which compares the computed curvature with the analytical value for a wave having the form, $y=0.012 \sin(\pi x)$. The calculation is indistinguishable, to graphical accuracy, from the analytical curvature. For a better assessment of the differences, the curvatures were calculated using three different node densities: 25, 35, and 50 nodes per wavelength and the root-mean-square error (compared to the true values) was evaluated. These were, for the coarse, medium, and fine calculations, 4.807 x 10^{-4}, 2.450 x 10^{-4}, and 1.199 x 10^{-4}, respectively.

The sensitivity of the curvature computations to the fineness of the node distribution, in the case of fully nonlinear water waves, was assessed through a convergence study. This was important because there may exist a large variation in the number of nodes per wavelength in a calculation, especially a calculation in which different frequencies are present. The curvature of the free surface was computed for one particular case of wave-maker motion amplitude and frequency (0.08m, 0.559Hz; the resulting waves had a steepness of about $ak=0.21$) using three different node distributions—25, 50, and 100 nodes per wavelength (the usual distribution adopted—the minimum recommended—is 30 nodes per wavelength). A representative comparison of the results is presented in figure 3.5.
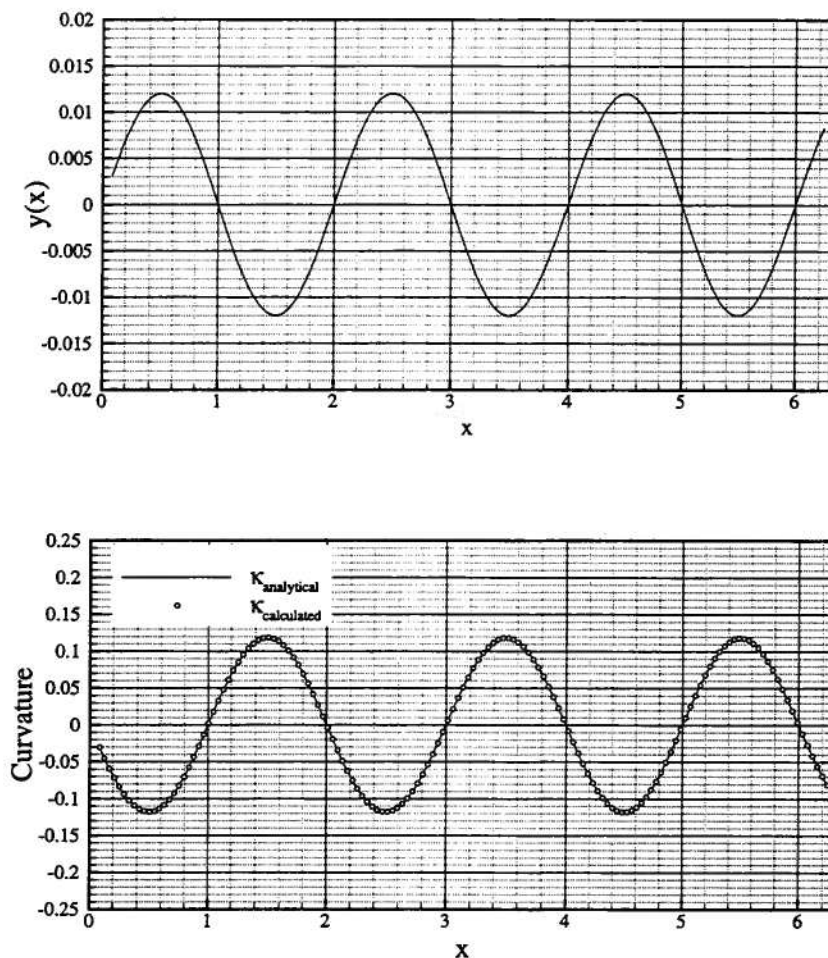
Figure 3.4: Comparison of analytically obtained surface curvature and that obtained using a local three-point formula

There is clearly a lot more noise in the calculations as the node density increases, and there are also notable differences in the maximum values of the curvature. Differences in the estimation of the curvature would undoubtedly be responsible for a wider "error band" in figure 3.3. However, given the sharp rise in the nature of the curve across the threshold value and that the present threshold value is already a conservative limit, the effect of the said differences on the results would be small. That is, the scatter does not appear to affect the nature of the $|\kappa a| - ak$ curve or the chosen limiting value of $|\kappa a|$ considerably.
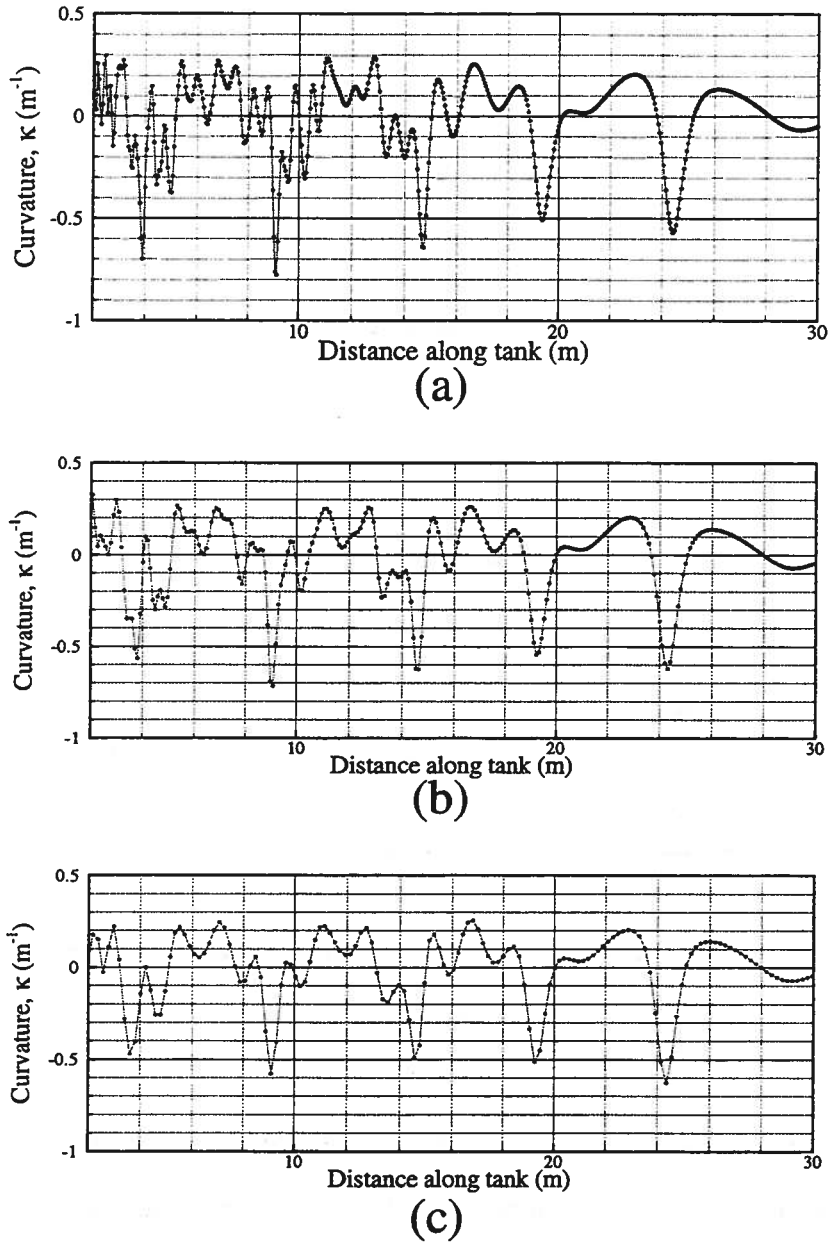
Figure 3.5: Representative snapshot of the computed curvature of the surface, using: (a) 100 nodes per wavelength, (b) 50 nodes per wavelength, and (c) 25 nodes per wavelength

Thus, we have arrived at a new, curvature-based criterion for breaking. This criterion is simple and easy to implement, even when waves of different frequencies are

present. It is also possible to apply this criterion to three-dimensional computations, including those with forward speed. A proposed approach, especially for ship flow calculations, is to detect the likely occurrence of wave breaking along the prescribed free-surface paths (the paths on which the Lagrangian nodes are convected in the UM-DELTA method; the paths generally take on the appearance of free-surface streamlines). It may also be necessary to consider the curvatures in other directions, as when a steep wave is aligned at an acute angle to the free-surface paths. This background leads us into the second part of the process of dealing with numerical wave breaking—the actual suppression of a breaking wave.

3.2   Suppressing of a Breaking Wave

Haussling and Coleman (1979) is probably the first known calculation wherein a breaking wave is explicitly suppressed so as to enable the computations to proceed. Haussling and Coleman suppressed a breaking wave by exerting an additional, external pressure on the wave in the vicinity of the location where the likelihood of wave breaking has been detected. By causing the wave to work against this external pressure, this technique in effect extracts energy locally from the waves and thereby prevents wave breaking.

Mathematically, this consists of the inclusion of an additional term, P_{damp} in the dynamic free-surface boundary condition:

$$\frac{\partial \phi}{\partial t} + \frac{1}{2}\nabla\phi.\nabla\phi + \frac{p}{\rho} + gz + \frac{P_{damp}}{\rho} = 0 \qquad (3.1)$$

This, incidentally, is also how most numerical absorbing beaches seek to minimize wave reflection (e.g., Cao et al., 1993).

It is to be noted, though, that Haussling and Coleman (1979) did not apparently attempt to devise a suitable, general criterion for the likelihood of wave breaking. They simply activated their wave damper (in their calculation for a submerged cylinder) when the wave slope of a particular breaking wave became too large.

Subramani et al. (1998a) adopted the approach of Haussling and Coleman in conjunction with the κa criterion, and demonstrated the successful suppression of the breaking wave observed in the previously described physical experiment of Grue et al. (1993). This is shown in figure 3.6. Subramani et al. used the following form for the damping term:

$$P_{damp} = s \cdot v(x) \cdot |\nabla \phi|^2 \cdot sgn\left(\frac{\partial \phi}{\partial n}\right) \tag{3.2}$$

where, the $|\nabla \phi|^2$ term determines the magnitude of the damping; s is the coefficient that may be varied to increase or decrease the amount of damping; the signum function (consistent with Haussling and Coleman, 1979) ensures that the pressure is acting against the wave; and $v(x)$ is a shape function chosen to ensure that the damper takes the form of a smoothly-varying patch:

$$v(x) = 0.5\left[1 + \cos\frac{\pi(x - x_o)}{L_o}\right] \tag{3.3}$$

Here, x_o is the location where $|\kappa a| = 0.35$ is exceeded, and L_o is half the length, centered about x_o, over which the damper acts. $v(x)$ is zero outside the bound,

$|x - x_o| > L_o$. L_o is prescribed to be $a_o/0.35$ (a_o is the wave amplitude at x_o)—again, from considerations of the geometry of breaking waves, so that the energy is extracted from approximately the portion of the wave between zero-crossings.
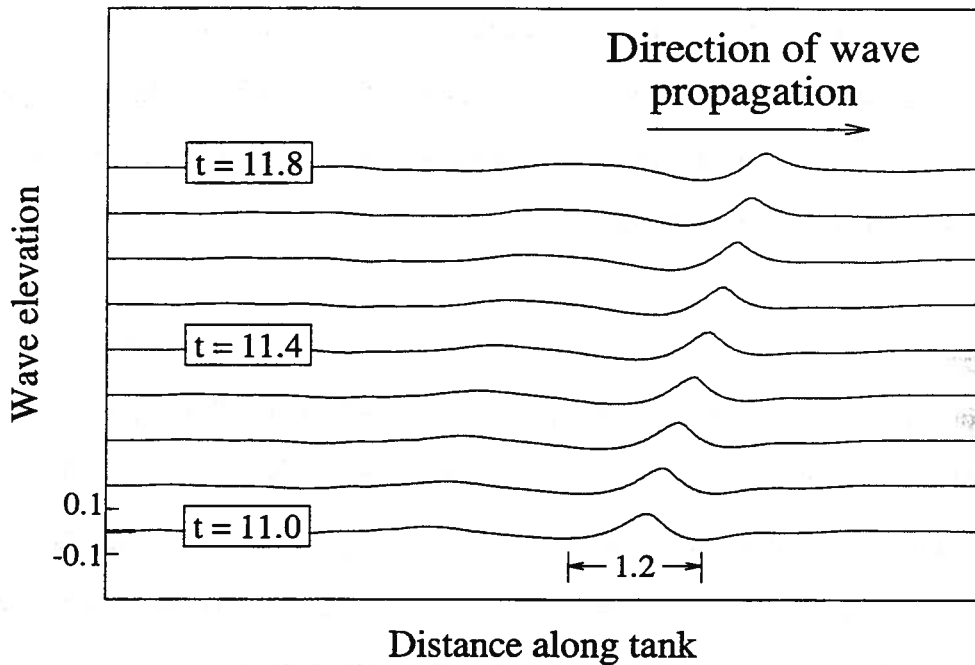
Figure 3.6: Time-history of the surface displacement in a numerical simulation involving the suppression of wave breaking using the "local absorbing patch" model

While this approach was able to provide satisfactory results, it proved not to be robust. Specifically, it was difficult to determine the appropriate amount of damping and there were also problems with extending the technique to calculations involving forward speed, especially in three dimensions. These limitations are overcome through a new and improved "localized-fairing" or "bridging" technique, which is used in conjunction with the existing, curvature-based criterion for wave breaking.

3.2.1 Bridging technique

This new technique lends itself well to Euler-Lagrange methods for solving water wave problems, but its "post-processing" nature also renders it adaptable to other kinds of methods. The technique continues to use the exceeding of the threshold $|\kappa a|$ to flag "problem" free-surface nodes. The difference lies in how a breaking wave (the growth of the flagged nodes) is subsequently suppressed. The working of the technique is depicted in figure 3.7 (a detailed snapshot of the wave surface at the end of a time step at time, t=11.30) and is described below.

For illustrative purposes, consider an instant within the UM-DELTA method when the boundary-value problem has been solved and the free surface has been updated by the growths, $\partial\eta/\partial t$ and $\partial\phi/\partial t$ (η being the wave elevation and ϕ, the velocity potential). The updated free surface, before fairing, is given by the dashed line in figure 3.7, with the free-surface nodes marked by hollow circles. Wave breaking, when it occurs, is manifested as a large growth in η at certain nodes.

The use of the curvature-based criterion enables us to flag such nodes (which satisfy $|\kappa a| > 0.35$) and simply to fair through them. As sketched in figure 3.7, we fit a cubic spline through the non-flagged nodes and re-position the problem nodes on this faired wave surface. In essence, we "bridge" through the flagged, problem free-surface nodes. Extensive tests have shown that a cubic spline gives reliable results.
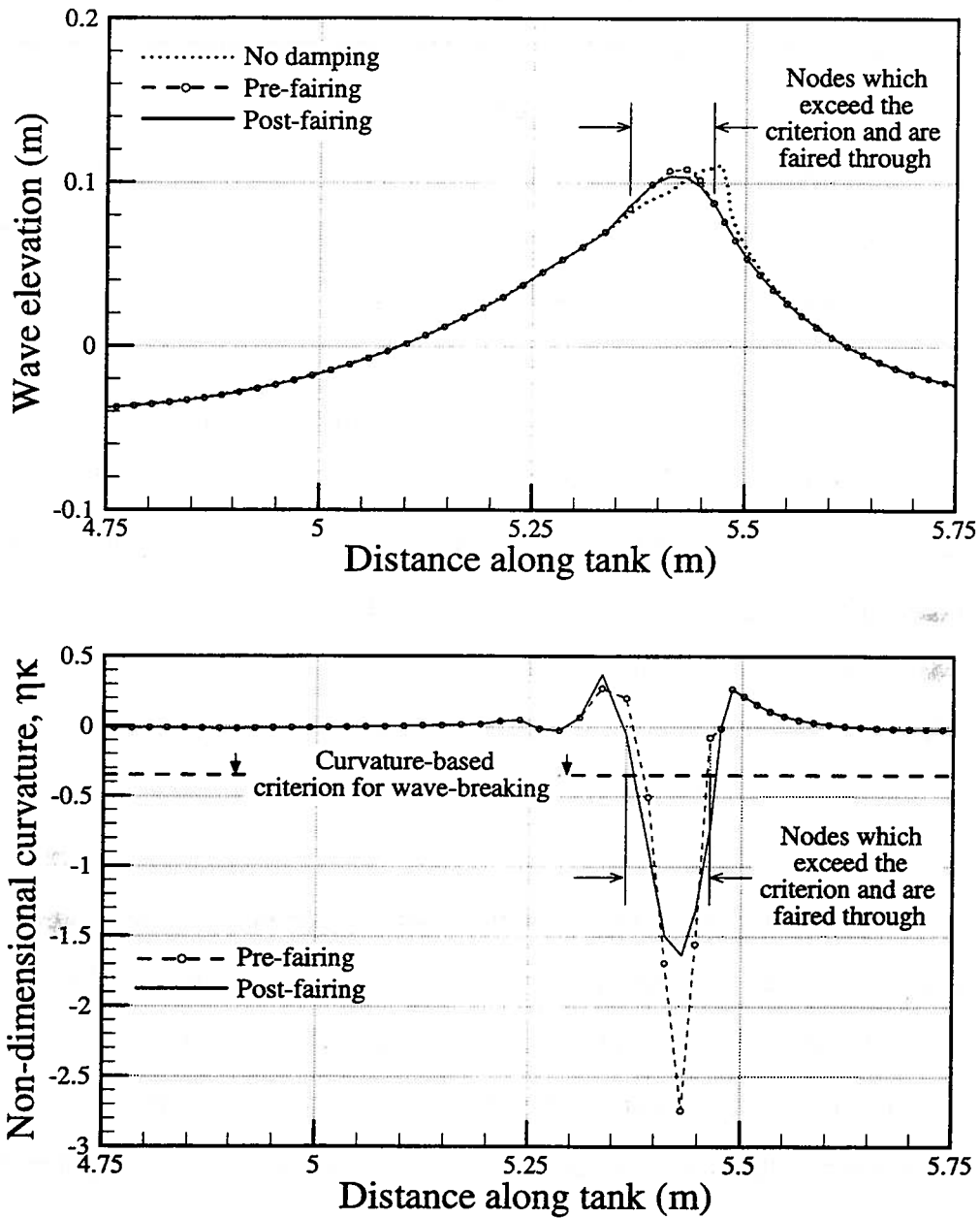
Figure 3.7: Damping of a breaking wave using the bridging technique in conjunction with the curvature-based criterion for wave breaking

This technique is essentially a variation of Wang et al.'s (1994) "peeling" technique; however, "bridging" may be more apt a description of the present treatment. In their studies on wave group evolution and deformation, Wang et al. had performed an

ad hoc reduction—based on a limiting value of ηk, where k is the wave number—of the wave crest at the leading wave front. Another important difference between the two techniques is that we do an identical fairing for ϕ – in order to ensure that there is no mismatch between η and ϕ for nodes on the new free surface. Wang et al. prescribed an exponential decay in potential when faced with evaluating ϕ for nodes on a free surface that had been lowered because of a peeling-away.

Note that implied in our technique is the discarding of the computed values of $\partial \eta / \partial t$ and $\partial \phi / \partial t$ for the nodes that seem poised—on the basis of the local curvature— to break. The flagged nodes by themselves are not discarded, it is important to add. Following the fairing and the setting of updated Dirichlet boundary conditions for the free surface, all the free-surface nodes are carried into the boundary value problem at the next time step. Also, the fairing process is carried out at the end of each intermediate time-step in the 4th-order Runge-Kutta time-stepping algorithm.

The post-fairing calculation, in which the tendency to break has been suppressed at a particular instant of time, is also shown in figure 3.7. Note also that the difference seen between the "post-fairing wave surface" and the "without damping" calculation is a cumulative result of the damper having been activated over the previous time-steps. A comparison of this new technique and the previous, "local absorbing patch" approach is made in figure 3.8.
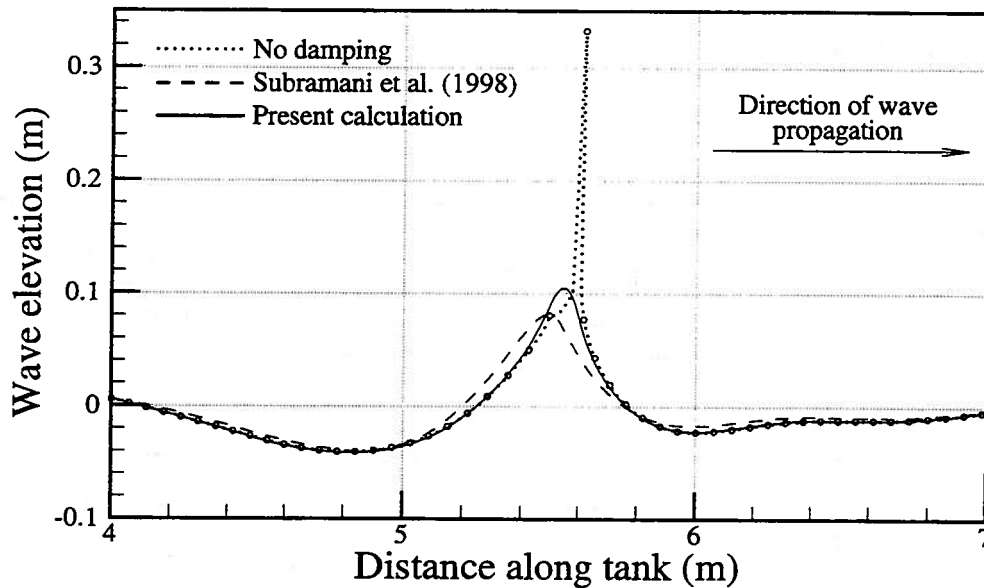
Figure 3.8: Comparison of results obtained using the local absorbing patch model and the bridging technique

Given the fairing-through of the problem free-surface nodes that occurs, there is an inevitable but slight loss of mass in our calculations. Figure 3.9 shows the extent to which mass conservation is controlled in the calculation discussed above. In the figure are plotted the percentage change of fluid volume in the tank (obtained by integrating the wave heights throughout the tank) for the following calculations: (a) one in which neither does wave breaking occur nor is the wave-breaking criterion exceeded, (b) one in which wave-breaking is not physically known to occur, but whose likely occurrence is still indicated, as a result of the conservative nature of the wave-breaking criterion, and (c) one in which wave-breaking does occur, is detected, and is successfully suppressed. For the calculation in question, the mass loss due to the wave-breaking suppression (about 0.075%) is not much more than the uncertainty that creeps into the calculations (about 0.025%) for the benign case (a). Note that the two-dimensional wave tank in the

calculation is 0.42m deep and 14.2m long, or approximately twelve times the wavelength
of the breaking wave in question.
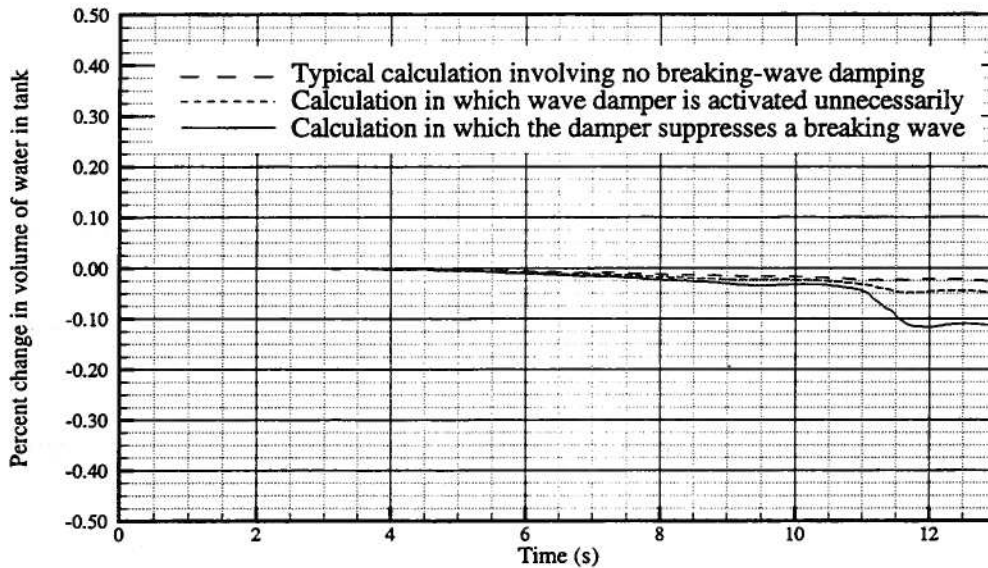
Figure 3.9: Estimation of mass lost in the process of suppressing a breaking wave using
the bridging technique

One of the advantages of the new technique is its ease of application and
robustness for instances of wave breaking in calculations involving forward speed. This
is discussed in the next chapter, along with other aspects of two-dimensional transom
stern computations.

CHAPTER 4

TWO-DIMENSIONAL TRANSOM STERN FLOW COMPUTATIONS

A study involving two-dimensional transom stern flow computations was undertaken as a prelude to UM-DELTA's extension for three-dimensional transom stern flow computations. The scope of the present work is two-fold: (1) to investigate closely and to test the transition from wetted to dry transom stern flow, and (2) to test the bridging technique for suppressing wave breaking in forward speed calculations.

The study follows Scorpio and Beck (1997), who first adapted the UM-DELTA method for two-dimensional transom stern flow computations. The cases studied by Scorpio and Beck (1997) corresponded to those in Vanden-Broeck and Tuck (1977) and Vanden-Broeck (1980), wherein nonlinear waves behind a transom stern were computed using a series expansion in the Froude number.

4.1 Problem formulation

Figure 4.1 shows the problem configuration. The x-y coordinate system is translating with speed U_o in the negative x-direction. Laplace's equation governs in the fluid domain and the velocity potential is $\Phi = U_o x + \phi$. The surfaces bounding the fluid are:

S_F = free surface;

S_H = body surface;

S_U = upstream truncation surface;

33

S_D = downstream truncation surface; and

S_B = bottom surface.
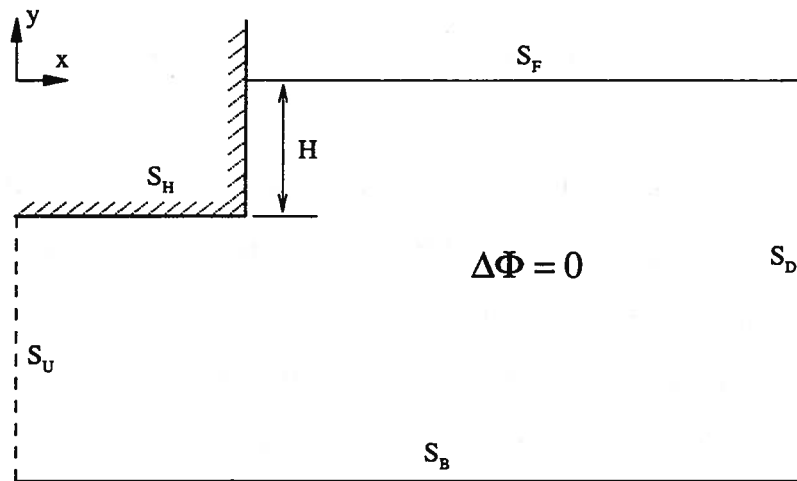
Figure 4.1: Two-dimensional transom stern calculations: problem configuration

The boundary conditions are:

$$\frac{D\eta}{Dt} = \frac{\partial \phi}{\partial z}, \qquad\qquad \vec{x} \in S_F \qquad\qquad (4.1)$$

$$\frac{D\phi}{Dt} = -g\eta + \frac{1}{2}|\nabla \phi|^2, \qquad\qquad \vec{x} \in S_F \qquad\qquad (4.2)$$

$$\frac{\partial \phi}{\partial n} = -U_o n_1, \qquad\qquad \vec{x} \in S_H \qquad\qquad (4.3)$$

$$\nabla \phi \to 0 \quad \text{as} \quad y \to -\infty, \qquad\qquad \vec{x} \in S_B \qquad\qquad (4.4)$$

The above equations relate, respectively, to equations (2.8), (2.10), (2.4), and (2.6) of the three-dimensional-problem formulation described in Chapter 2. Here,

$\dfrac{D}{Dt} = \dfrac{\partial}{\partial t} + \nabla\Phi \cdot \nabla$ is the material or Lagrangian derivative, $\bar{x} = (x_1, x_2)$ are the coordinates of control points on the problem boundary, $\bar{n} = (n_1, n_2)$ is the unit normal on the body pointing out of the fluid, g is the acceleration of gravity, η is the free surface elevation, and ϕ is the perturbation potential. The boundaries S_U and S_D are left unspecified (while placed far enough upstream and downstream, respectively), because very little differences have been observed between such calculations and those in which S_U and S_D are prescribed to satisfy continuity. The general numerical details are similar to those outlined for the three-dimensional problem.

4.2   Transition from wet to dry transom stern flow

Vanden-Broeck (1980) suggested that two realistic solutions exist for the steady flow behind a transom stern. For small values of the Froude number, the flow rises up the transom to a stagnation point. The free surface separates from the transom at the stagnation point, creating waves downstream that increase in steepness with increasing Froude number. This solution will be referred to as "A" hereafter. Solution A is physically unreasonable for large Froude numbers because the ratio of stagnation height to transom depth goes to infinity as Froude number goes to infinity. For large Froude numbers, a second, more physically-realizable solution exists wherein the flow separates cleanly from the bottom of the transom. This solution will be referred to as "B" hereafter. Solution B reduces to the uniform stream as Froude number tends to infinity and the downstream waves steepen as Froude number becomes small. In fact, Vanden-Broeck found a minimum Froude number (F_H, Froude number based on transom depth, of 2.26) below which the downstream waves exceed the theoretical breaking wave steepness limit $(2a/\lambda = 0.141)$. This variation of wave steepness with Froude number, for waves downstream of the transom, is illustrated in figure 4.2.
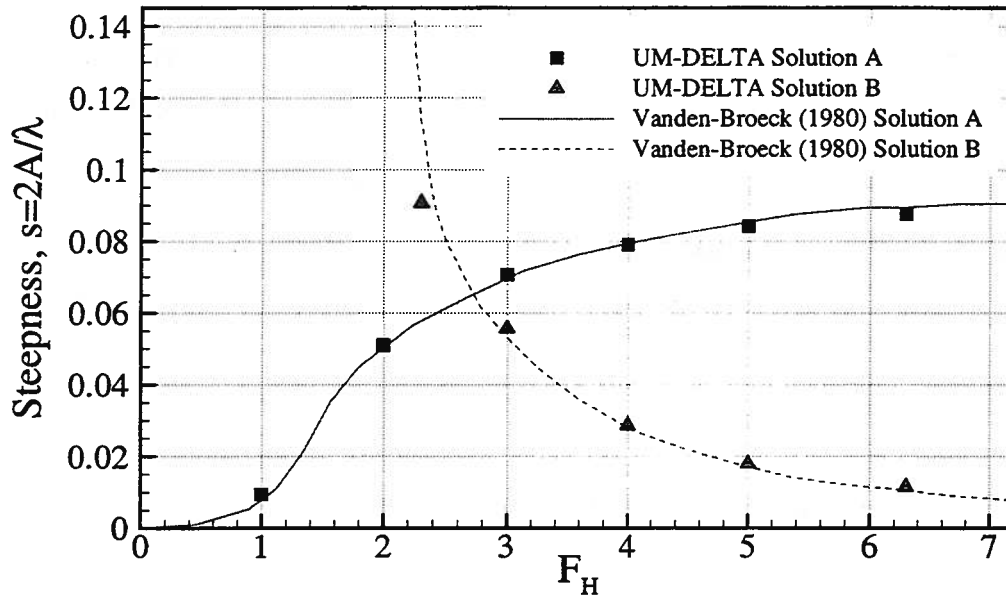
Figure 4.2: Wave steepness versus Froude number, F_H for waves downstream of a two-dimensional transom stern (adapted from Scorpio, 1997)

In the UM-DELTA method, as the problem is started from rest and the hull is accelerated up to steady forward speed (U_b), the inviscid solution always—regardless of the Froude number—tends towards solution A, as the hull reaches steady forward speed. This is shown in figure 4.3, for F_H=4.0.
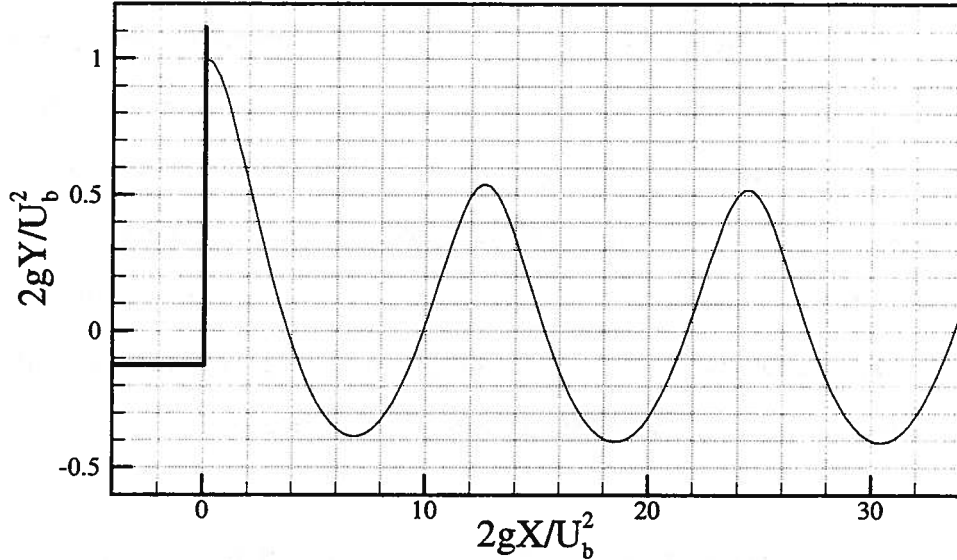
Figure 4.3: Obtaining of stagnation (type A) flow at F_H=4.0

In a viscous fluid, we know that the flow behaves like solution A at low Froude numbers and transitions to solution B as Froude number increases. As the hull speed increases from rest, the flow separating from the bottom of the transom becomes turbulent, resulting in the "dead water" region commonly observed behind transom sterns. Consequently, the pressure behind the transom is lowered. Eventually the falling pressure causes the free surface to drop to the bottom of the transom resulting in the solution B flow. Once the free surface separates cleanly from the transom, the turbulence is confined to a thin boundary layer (for high speeds) and the viscous wake. Since an inviscid flow model lacks turbulence, numerical artifices have to be devised in order to effect a transition from a transom wetted to transom dry state.

Haussling (1980) showed that solution B can be attained, within an unsteady formulation, by assuming the free surface to be fixed at the bottom of the transom for all time after an abrupt acceleration of the stern. Scorpio and Beck (1997) found two other ways by which to effect an artificial transition from solution A to solution B. In the first

method, the problem is started at steady forward speed with the transom out of the water. The hull is then slowly lowered into the water. As the hull is lowered, the free surface remains separated from the bottom of the transom and solution B results. However, this technique would not work for a problem in which the ship starts at rest with the transom immersed. To obtain solution B for a problem that starts from rest, a second technique was adopted: mimicking the effect of the dead water region by artificially lowering the stagnation pressure on the transom. This pressure drop was modeled in the inviscid flow code by modifying the boundary condition on the transom.

The stagnation pressure on the transom stems from the boundary condition,

$$\frac{\partial \phi}{\partial n} = -U_o n_1 \tag{4.5}$$

Scorpio and Beck's (1997) technique for reducing the stagnation pressure consisted of modifying this transom boundary condition to:

$$\frac{\partial \phi}{\partial n} = -U_o n_1 (2e^{-\beta t^2} - 1) \tag{4.6}$$

This modified form of the transom boundary condition was chosen arbitrarily, with there being no special significance in the exponential decay other than that it enables a smooth transition in the boundary condition. In their studies, Scorpio and Beck (1997) found that as the hull accelerates up to speed, the pressure on the transom drops until the free surface drops towards the bottom of the transom. They realized solution B (as depicted in figure 4.4) by then pulling the free-surface node down to the transom bottom as soon as it came close enough to the bottom. This step was followed by imposing one additional constraint (or Kutta condition) at the bottom of the transom in the solution B

flow. The free surface nodes, which move downstream with the fluid velocity during the intermediate time steps (4th-order Runge-Kutta), are normally regridded back to their original positions by interpolating elevations and potentials. The Kutta condition is imposed by regridding the first free surface node back to the bottom of the transom. The potential at this point is computed from the source strengths.
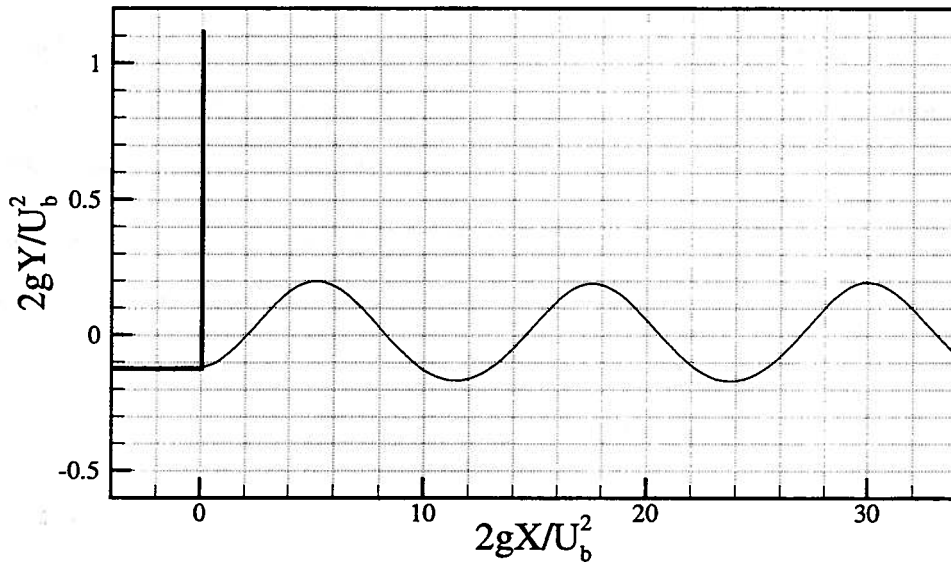
Figure 4.4: Obtaining of cleanly-separating (type B) flow at F_H=4.0 according to Scorpio and Beck (1997)

However, this technique for effecting solution B, while seemingly appropriate and effective, proved not to be robust during subsequent and more stringent tests under the current research. It was found that if the free-surface node on its way down to the transom bottom was not pulled down soon enough, it would tend to behave in an unstable manner, actually climbing back way up the transom stem again. The problem was traced to the accuracy of the induced velocities at the first free-surface node, specifically to inaccuracy in the tangential velocity. As the dominant term in (4.1) and (4.2), the induced velocities are what determine the direction in which η and ϕ grow. In the UM-

DELTA method, inaccuracy in the tangential velocity for the free-surface node at the transom face was, unfortunately, inevitable. This is because only one boundary condition (on the normal velocity) may be prescribed for that free-surface node, leaving the tangential velocity unprescribed. (Recall that, in the UM-DELTA method, there is a double node where the free surface meets the transom. One node satisfies the body boundary condition, while the other satisfies the free-surface boundary condition.)

The question arose as to whether the "right" amount of stagnation pressure reduction could be prescribed so as to effect a stable transition to cleanly-separating transom stern flow. To answer this, the steady-state velocity, $\nabla\phi$ for a free-surface node separating cleanly from the bottom of the transom was obtained by solving the quadratic equation, (4.2); the transom boundary condition was then modified correspondingly to:

$$\frac{\partial\phi}{\partial n} = U_o\left(-1 + \sqrt{1 + \frac{2}{F_H^2}}\right)n_1(1 - e^{-\beta t^2}) \qquad (4.7)$$

However, instead of resulting in cleanly-separated transom stern flow, the calculations showed the free surface fail to drop to the transom bottom, as illustrated in figure 4.5. Again, the anomaly was traced to inaccuracy in the computed tangential velocity at the transom, and hence in the computed vertical velocity for the first free-surface node.
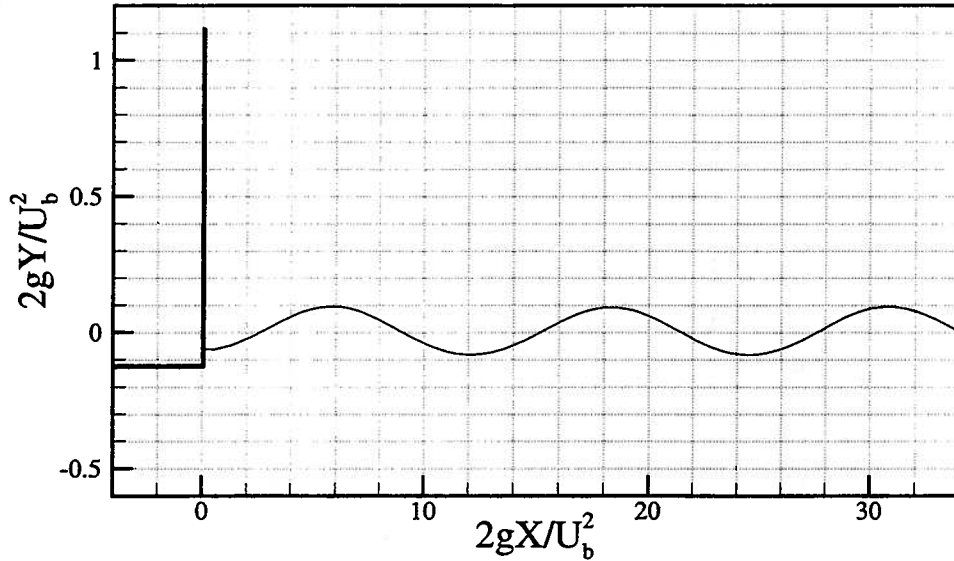
Figure 4.5: Calculations, at F_H=4.0, corresponding to the analytically expected case of

cleanly-separating transom stern flow

As a result of these investigations, the technique of Scorpio and Beck (1997) was

remedied through some slight modifications. Noting that the inaccuracy in the tangential

velocity was more pronounced during the downward motion below z=0 of the free

surface, the stagnation pressure was decreased (compared to equation 4.3) only to the

extent resulting from the following boundary condition:

$$\frac{\partial \phi}{\partial n} = -U_o n_1 e^{-\beta t^2}$$

(4.8)

This would have the effect of driving, as the transom picked up speed with time,

the free surface down to just the calm-water level, as shown in figure 4.6.
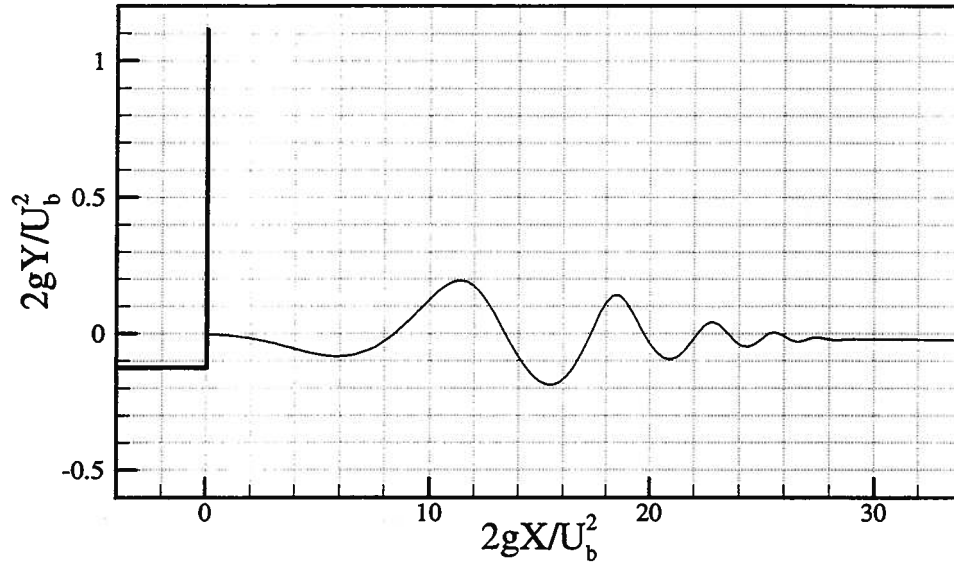
Figure 4.6: Effect of a release of stagnation pressure on the transom face

Then, once this stage was reached (at $t=t^*$, say), a second modification was phased in, through the gradual introduction of a spatially-varying "hydrostatic pressure" offset into (4.2):

$$\frac{D\phi}{Dt} = -g\eta + \frac{1}{2}|\nabla\phi|^2 + gH(1 - e^{-\alpha(t-t^*)^2})e^{-\gamma(x-x_{transom})^2} \qquad (4.9)$$

The effect of this offset is to have the p=0 level now correspond not to z=0, but to the transom bottom, z=-H. The free surface that had stabilized at z=0 as a result of (4.8) will now automatically tend to be re-located at z=-H, as shown in figure 4.7.
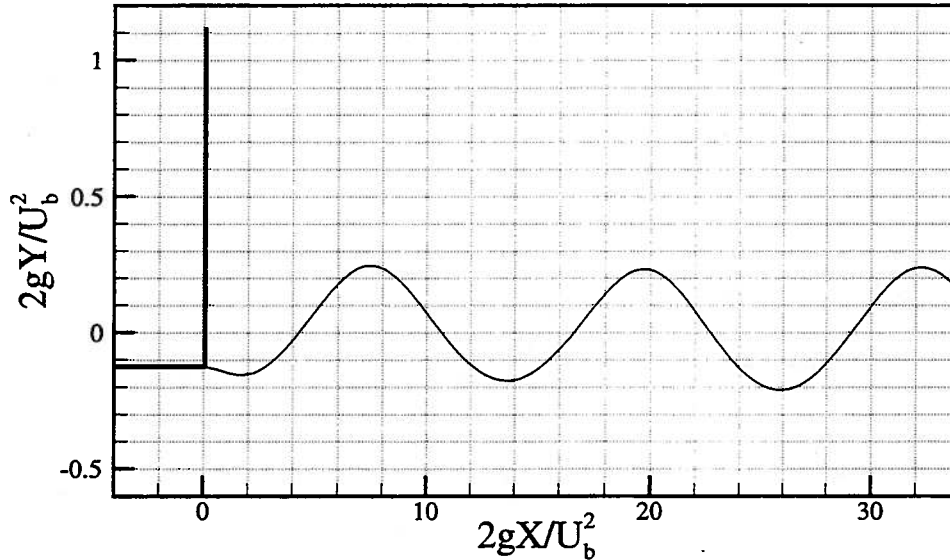
Figure 4.7: Effect of the introduction of a hydrostatic-pressure offset in the dynamic free-surface boundary condition

If left to remain, however, (4.9) would result in waves that appear to be unnaturally depressed a little downstream (due to the spatial variation in the hydrostatic offset term) of the transom. This is, of course, consistent with the fact that any applied pressure distribution on the free surface creates waves. Therefore, once the free surface has reached the transom bottom, only the previous described Kutta-condition-like regridding is carried out; the pressure offset in (4.9) is withdrawn gradually, leaving behind the desired solution B. This final withdrawal of the hydrostatic offset term and the accompanying transition to a stable solution B is shown in figure 4.8. For comparison, a successful calculation of Scorpio and Beck (1997) is also plotted. This modified technique was found to give far more reliable a transition from transom wetted to transom dry flow, and it was retained for adoption in the three-dimensional calculations to follow.
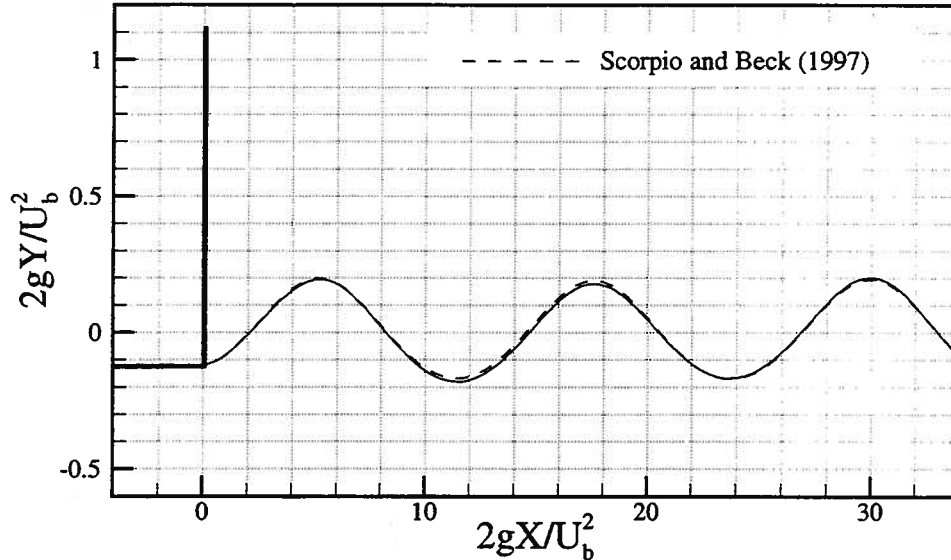
Figure 4.8: Withdrawal of the hydrostatic-pressure offset and the realizing of cleanly-

separating flow, at F_H=4.0

4.3 Suppression of a breaking wave

As previously mentioned (and as can be read from figure 4.2), there exists a minimum Froude number, in the smoothly-separating flow regime, below which the downstream waves become too steep and break. This was taken as a test case for testing the "bridging technique" breaking-wave damper discussed in the previous chapter. Figure 4.9 shows a smoothly-separating flow solution at the near-critical Froude number of 2.3, with the wave crest breaking just downstream of the transom. The application of the damper to this forward-speed test case is also shown in the same graph. As seen, the breaking has been suppressed successfully.
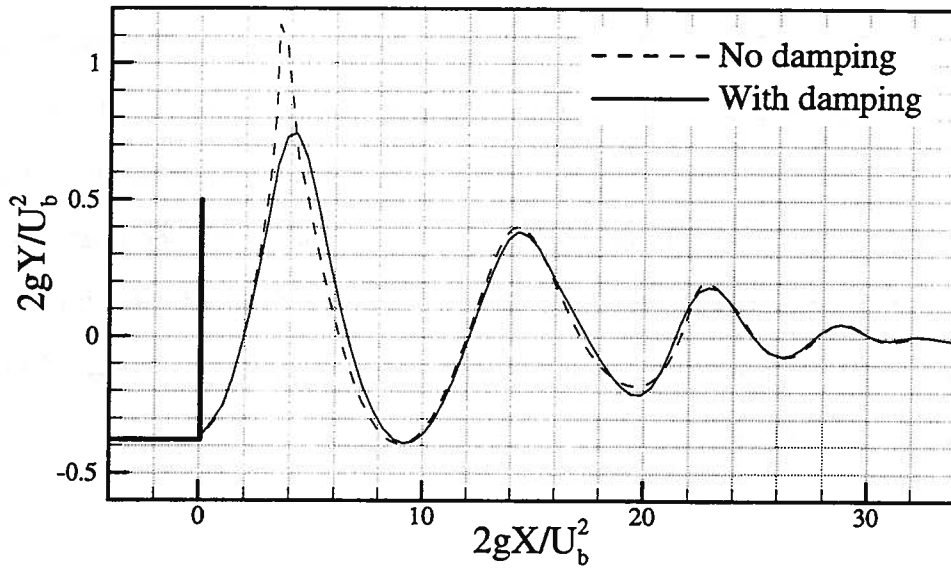
Figure 4.9: (a) Cleanly-separating flow at the near-critical F_H of 2.3; (b) suppression of the breaking wave using the bridging technique

Convergence of the damped solutions is demonstrated in figure 4.10, with calculations obtained for three different node resolutions.
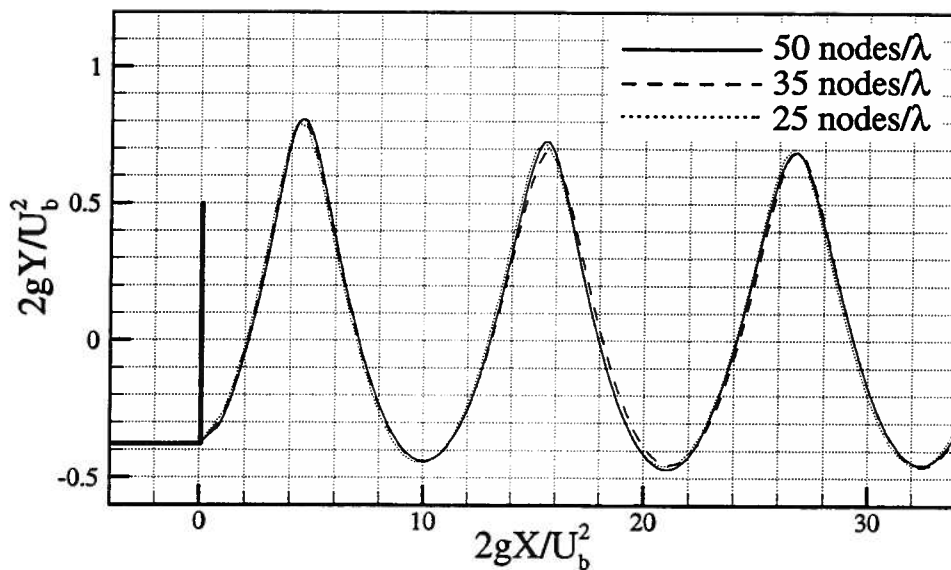
Figure 4.10: Convergence of solutions obtained using the bridging technique

The bridging technique has thus been shown to work easily and reliably for forward speed calculations. The technique holds promise for three-dimensional ship wave calculations as well. The wave-breaking criterion may be used to detect the likely occurrence of wave breaking along any predominant wave propagation direction. The fairing technique may then be used to suppress the detected wave breaking. It may also be used to overcome the numerical instabilities otherwise encountered in the calculation of a three-dimensional bow wave.

CHAPTER 5

THREE-DIMENSIONAL FORWARD SPEED COMPUTATIONS

In this chapter, the successful extension of UM-DELTA to practical, three-dimensional ship hull forms is demonstrated. First, a description is provided of the hull-surface processor that was developed to handle realistic hull forms. Results are then presented for arbitrary and complex hull forms. Specifically, calm-water results are presented for the Series 60, $C_B=0.6$ hull—which typifies arbitrary body shapes—at Fr=0.316, and grid convergence is demonstrated across three grids that feature a doubling in grid size. Wave resistance computations using two different approaches are presented and discussed. Next, results are presented for two transom-sterned vessels—the DDG5415 naval combatant and the D1 fast monohull. In this, stagnation flow and cleanly separating transom stern flow are presented for the DDG5415 at Fr=0.28 and grid convergence is shown. Lastly, cleanly separating transom stern flow calculations are presented for the D1 fast monohull at Fr=0.433—a case involving the successful application of the bridging technique to suppress a steep, breaking rooster-tail wave crest. All of the above calculations are also validated—where possible—through a comparison with the available experimental data.

5.1   Modeling of arbitrary hull shapes

As mentioned in the Introduction (chapter 1), modeling of the geometry is not a trivial task within the UM-DELTA method. Unlike panel methods that use flat quadrilateral panels to define the surface and the unit normal, UM-DELTA uses discrete

body nodes (and associated Rankine sources) to define the body surface. For purposes of illustration, figure 5.1 (a) provides a perspective view of the typical grid distribution on the body and free surface, while in figure 5.1 (b) are sketched the relative locations, at a representative cross-section, of the nodes and the desingularized sources.

(a)

(b)
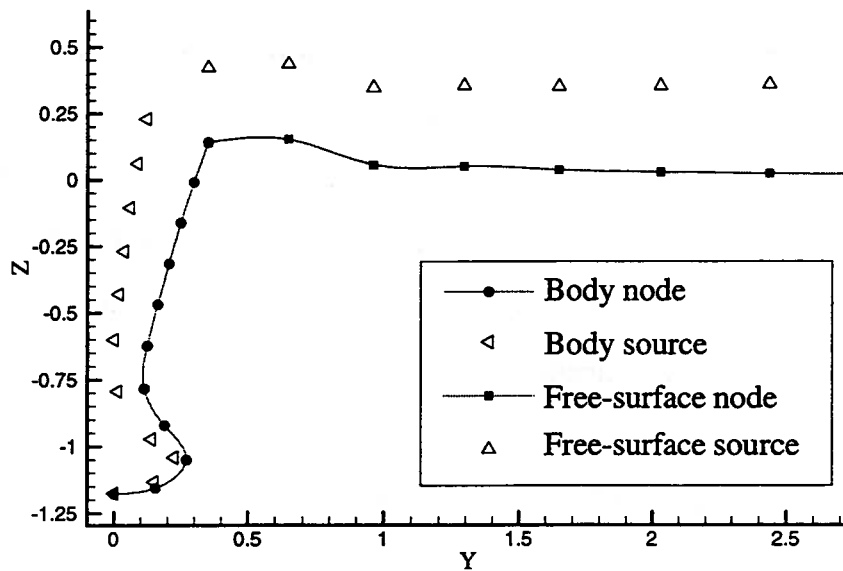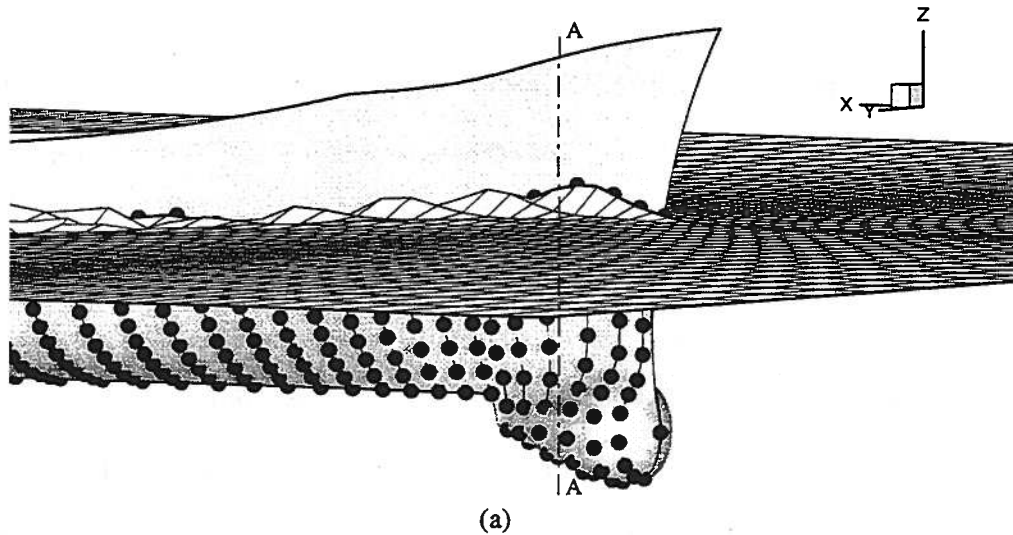
Figure 5.1: (a) Perspective view of typical grid distribution and (b) cross-section at A-A showing the relative locations of the nodes and sources

5.1.1 HULLGEO module

Determining the surface location and unit normals at arbitrary node locations on a typical (i.e., realistic, as against mathematical) ship hull is not easy, and this has served as a hurdle in the extension of the method to arbitrary and complex ship hulls. Rejecting the NURBS surface representation approach tested by Celebi and Beck (1997), a different geometry processor was independently developed (Beck, 1998) to enable UM-DELTA to handle arbitrary and complex hull forms with greater ease and efficiency. Christened HULLGEO, the geometry processor can handle bulbous bows, sterns with deadwood, and transom sterns—in addition to conventional raked bows and cruiser sterns. It can also be extended easily to multihulls or tunnel hulls.

The underlying idea is of using precomputed cubic spline fits of the waterlines and stations to return values of the unit normals at the desired node locations. Figure 5.2 shows the unit normals returned by HULLGEO for the DDG5415 naval combatant model. The unit normals have been evaluated at test nodes distributed along the stations that formed the input to the processor. As can be seen clearly, the vectors closely represent the complex geometric features of the combatant.

Given that the normals are evaluated based on cubic spline fits, some amount of noise in the results is inevitable, especially for complex geometries and if the body surface is coarsely discretized. The noise may be minimized by providing as input to HULLGEO a discretized surface of fine resolution; then, at the interface between HULLGEO and UM-DELTA, a select subset of the input stations may be retained as the stations on which collocation points are actually distributed.
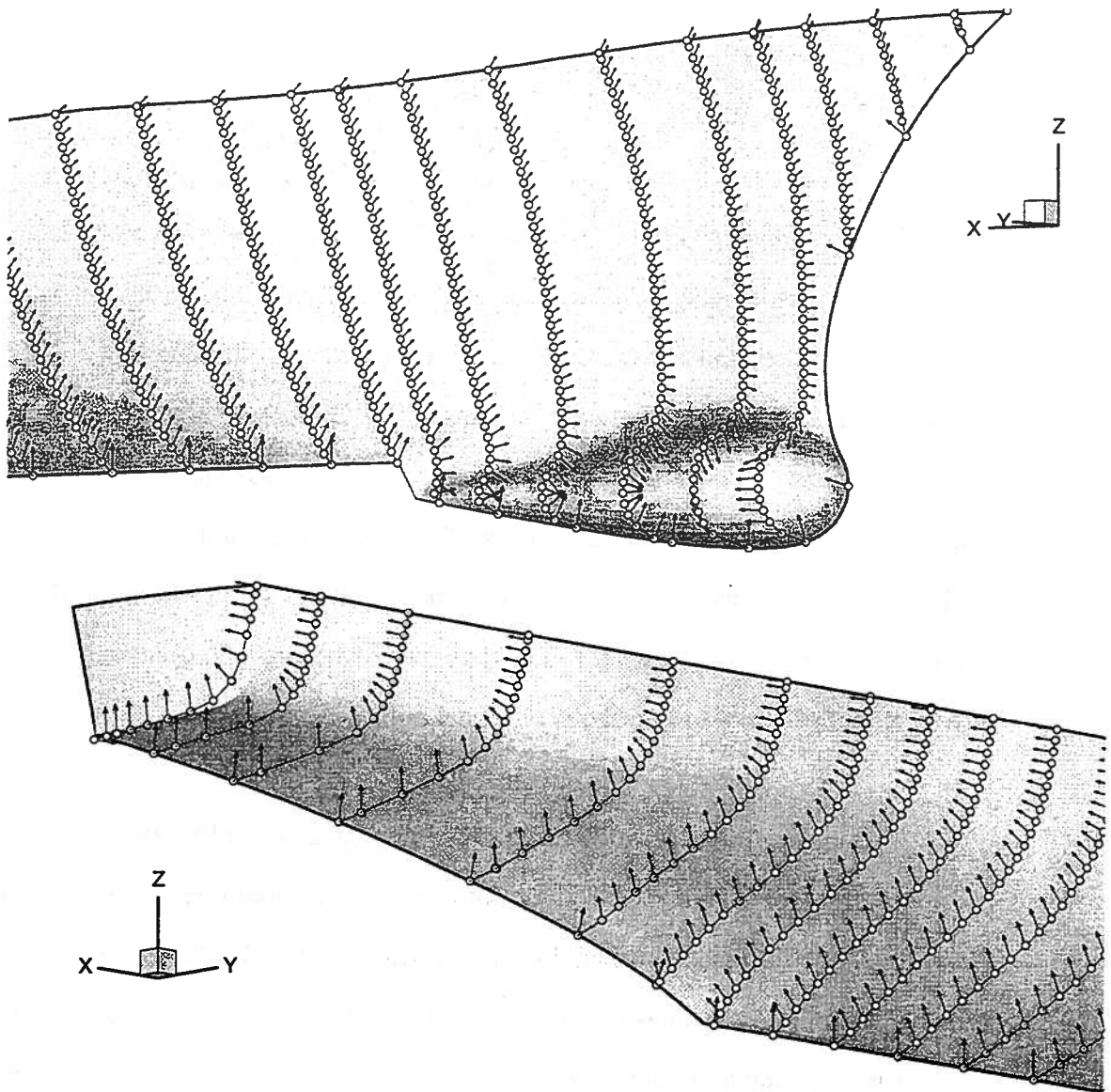
Figure 5.2: Unit normals on the body as obtained by the geometry processor: (top) bow and (bottom) stern regions of the DDG5415 combatant model

The unit normals are verified through a test for the standard Wigley hull. The Wigley hull (see figure 5.3) is a mathematical hull form with offsets defined by

$$y(x,z) = \frac{B}{2}\left(1-\left(\frac{2x}{L}\right)^2\right)\left(1-\left(\frac{z}{T}\right)^2\right)\left(1+a_2\left(\frac{2x}{L}\right)^2\right) \tag{5.1}$$

where L is the length, B is the beam, T is the draft, and a_z is a coefficient that is 0.0 for the standard Wigley hull and 0.2 for the modified Wigley hull III. $\dfrac{L}{B} = 10$ and $\dfrac{B}{T} = 1.6$ for either hull. The hulls are also wall-sided above z=0.

Consequently, the unit normals for this hull may be obtained mathematically. Table 1. shows the L_2 norm of the differences between the unit normals returned by HULLGEO and those obtained analytically. The differences are almost insignificant in the case of this simple hull. The coarse, 35-stationed grid also seems to be sufficient to resolve the body surface accurately. For the realistic Series 60, $C_B=0.6$ hull and the complex DDG5415 model, however, the body surface was resolved using about 140 stations.
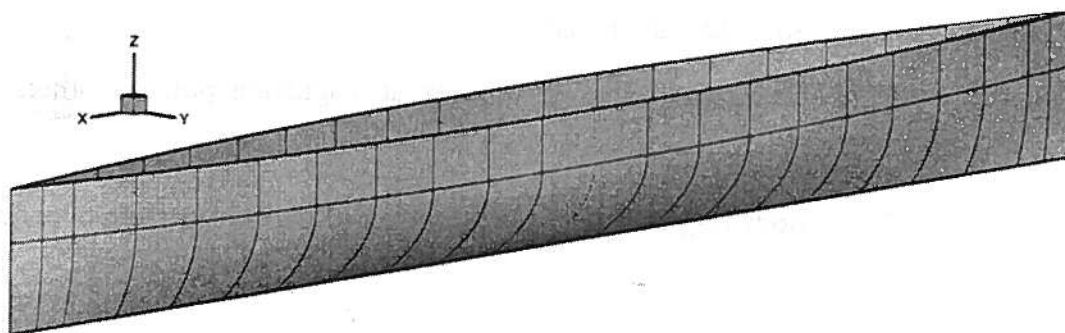
Figure 5.3: Perspective view of the standard Wigley hull

Table 1. Comparison of unit normals for the standard Wigley hull

No. of stations	$\dfrac{1}{N_{nodes}}\sqrt{\sum\limits_{i=1}^{N_{nodes}}\left(x_i - x_{analytical}\right)^2}$
35 (30 nodes/station)	5.24×10^{-8}
49 (42 nodes/station)	2.54×10^{-8}
69 (60 nodes/station)	1.98×10^{-8}

5.1.2 Additional issues

Notwithstanding that UM-DELTA obtains body unit normals using precomputed cubic spline fits, additional issues and challenges remain with regard to the body panelization itself. They are, broadly:

(1) Desingularization of sources at stagnation points, corners, and convex cross-sections

(2) Body re-gridding following the emergence/immersion of entire stations

These are discussed in depth in the sections to follow.

5.2 Series 60, C_B=0.6 hull

The Series 60, C_B=0.6 parent hull not only typified a practical hull form for the present project, but it is also one of the most widely used hull forms in the development and validation of computational methods. Developed at the David Taylor Model Basin (now Naval Ship Research and Development Center) using results deduced from

successful ships and incorporating those features considered necessary for good resistance qualities, the particulars of the Series 60 line of hull forms are commonly available. (The results of the model tests accompanying their development can be found in Todd, 1963.) The inclusion of the Series 60, C_B=0.6 model in the Cooperative Experimental Program (ITTC, 1987) for the creation of a reliable model-scale database has resulted in the availability of extensive data against which to validate the calculations. A validation of the present calculations is made possible by the availability of tabulated data from the experiments carried out at the Iowa Institute of Hydraulic Research (Toda et al., 1992; Longo and Stern, 1996) and by Kim and Jenkins (1981).

5.2.1 Treatment of stagnation points and bilges

As depicted in figure 5.4, the Series 60, C_B=0.6 is a slender hull form with a cruiser stern and a fine bow. The fine bow is near-vertical and may be reasonably approximated, within the calculations, as a plumb bow.
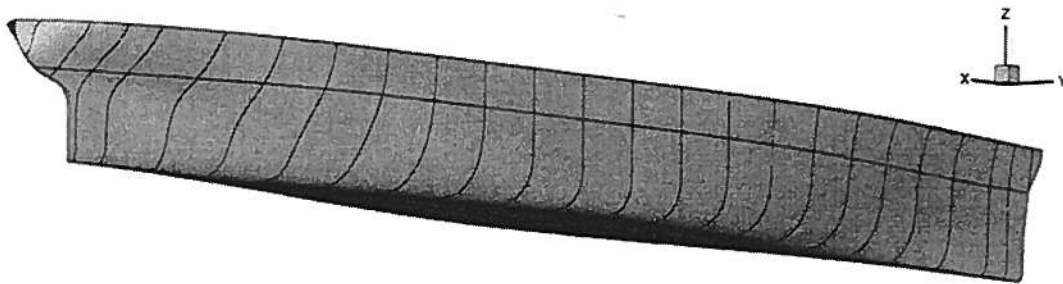
Figure 5.4: Perspective view of the Series 60, C_B=0.6 hull

In their numerical experiments on the two-dimensional Karman-Trefftz airfoil and the mathematical Wigley hull, Beck et al. (1994) recognized well the difficulties that can arise in the placement of singularities inside a body having a sharp leading edge, such as the bow of a ship. Normally, in the UM-DELTA method, the desingularization distance for the sources is proportional to the local node spacing or panel area. The constant of proportionality is a factor, L_d, usually prescribed to be equal to one.

In the placement of desingularized sources at a fine bow, however, Beck et al. (1994) proposed two modifications. These are explained with reference to figure 5.5, which shows the waterplane through z=0 of the bow of the Series 60, C_B=0.6 hull. Firstly, sources that cross over the centerline are to be moved back onto the centerline. (This is done without changing the x-coordinate of the sources.) Secondly, the source corresponding to the leading edge node is given a much-reduced desingularization distance (usually, 0.01 L_d instead of L_d). If the desingularization distance were not reduced, the source – which would have to have a suitably large strength to cancel out the free stream velocity at the stagnation point – would end up inducing an erroneously large tangential velocity at the neighboring nodes.
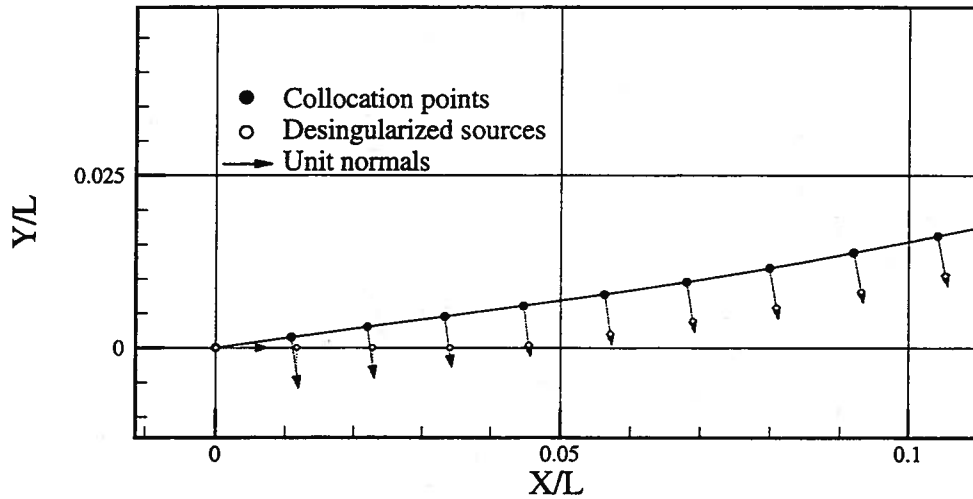
Figure 5.5: Waterplane through z=0 of the bow of the Series 60, C_B=0.6 hull, showing the placement of body nodes, desingularized sources, and unit normals

While this aspect of the treatment of fine leading edges was common to the Karman-Trefftz airfoil and the Wigley and Series 60, C_B=0.6 hulls, two additional considerations need to be given to the Series 60, C_B=0.6 hull discretization. One, this hull has a parallel middle body consisting of a flat bottom that meets the sides of the hull at a rounded bilge. If the constant desingularization distance of 1.0 L_d were maintained, there may result a piling up or crossing over of sources at the bilge. Therefore, in the discretization of this hull, the body sources along a station are prescribed not a constant L_d but one that varies smoothly (between 0.01 and 1.0). They are prescribed an L_d equal to the ratio of the local girth (measured from the keel up to their corresponding nodes) to the station girth (measured up to the uppermost body node). This is sketched in figure 5.6. Note, however, that a much-reduced L_d at the keel is necessitated only for cases where the keel is a stagnation line, as for a heaving hull. Although a reduced L_d at the keel was retained (for the present hull-fixed calculations), the emphasis was on obtaining a smooth, stable distribution of sources along the stations (see also figure 5.1.b).
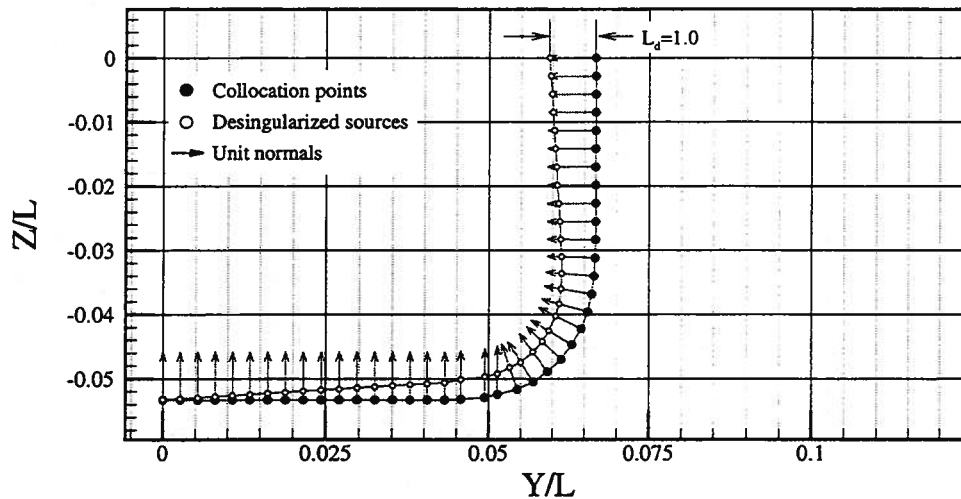
Figure 5.6: Varying desingularization distance along a station: cross-section of the Series 60, C_B=0.6 hull showing the locations of body nodes, sources, and unit normals

The other consideration pertains to the treatment of the stern rake. Unlike the Wigley hull, which has a vertical stem and stern, the cruiser-sterned Series 60 body discretization is closed off using a point node at the stern rake. Unlike the rest of the stations, this point node is allowed to move in the x-direction in a tracking of the body–free-surface intersection point, as illustrated in figure 5.7 (using the 70-stationed grid).

5.2.2 Conditions and grid parameters

Calculations for the ship advancing straight ahead in calm water were initiated for Fr=0.316, a Froude number widely used in the validation of computational methods. Three body discretizations were used, with a grid-doubling across the grids: a coarse grid consisting of 36 stations, a 47-stationed medium grid, and a 70-stationed fine grid, which are shown in figure 5.8 (drawn to scale). As previously described, however, a finer, 142-stationed body grid was used to obtain body unit normals within the HULLGEO module.

The three different body discretizations above were obtained as subsets of the 142-stationed hull, in an interface between HULLGEO and the UM-DELTA solver.

The node density along a station, in terms of nodes along a girth equal to the ship draft, was prescribed to be 10 for the coarse grid, 14 for the medium grid, and 20 for the fine grid. The total number of nodes on the body was 517 for the coarse grid hull, 968 for the medium grid, and 2073 for the fine grid.

Due to symmetry, the calculations are performed in the half-domain, Y>0. The domain of the numerical wave tank for all the three grid discretizations was bounded by an upstream end 0.5 times the ship length (length between perpendiculars, L=20.0 m) ahead of the bow, with the tank extending for 1.0 L downstream of the stern and measuring 0.6 L across (on the side, Y>0). The free-surface discretization corresponding to the coarse body grid was 61 nodes in the longitudinal direction and 16 nodes in the transverse direction. For the medium grid case, it was 86x23; and for the fine grid case, 122x32. For the coarse body grid, the number of free-surface nodes ahead of the body, across the body, and downstream of the body were, respectively, 10, 26, and 25; for the medium grid, the corresponding distribution was 14, 38, and 34; and for the fine grid: 20, 52, and 50. In all cases, the free-surface grid is set up in such a way that the grid spacing is not uniform; rather, the free-surface node distribution is (while still showing a smooth variation in node spacing) denser in regions of large gradients. Consequently, the node spacing in the longitudinal direction is smallest near the ship's bow and stern; and in the transverse direction: near the hull.
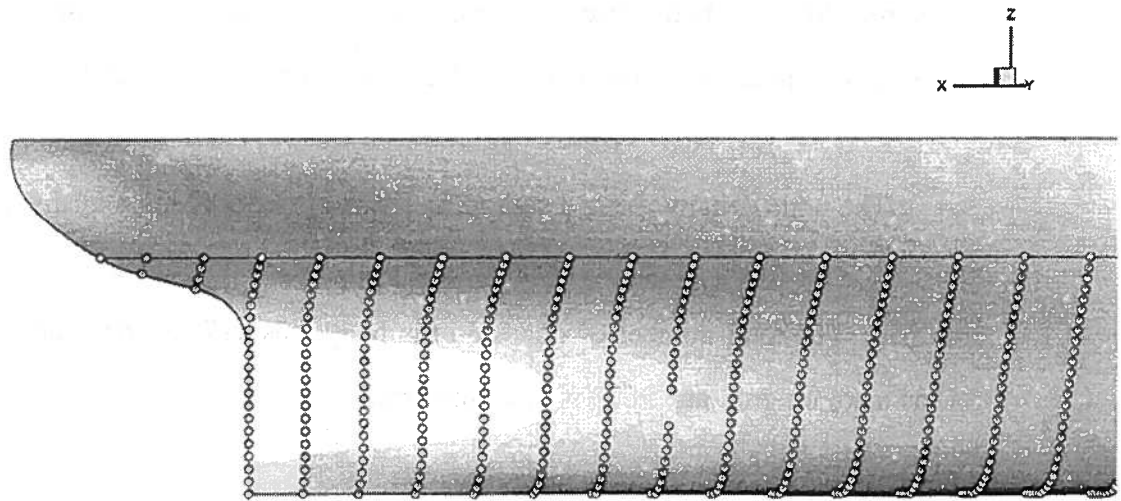
(a) At t=0
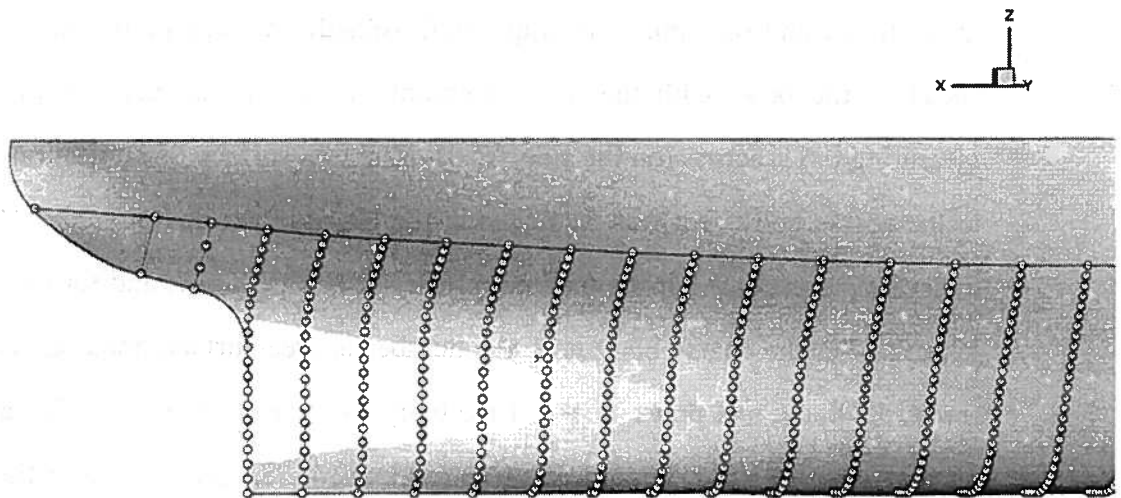
(b) At a later time

Figure 5.7: Treatment of stern (and stem) rakes: point node at the stern of the Series 60, $C_B=0.6$

(a) Coarse grid (36 stations)

(b) Medium grid (47 stations)

(c) Fine grid (70 stations)
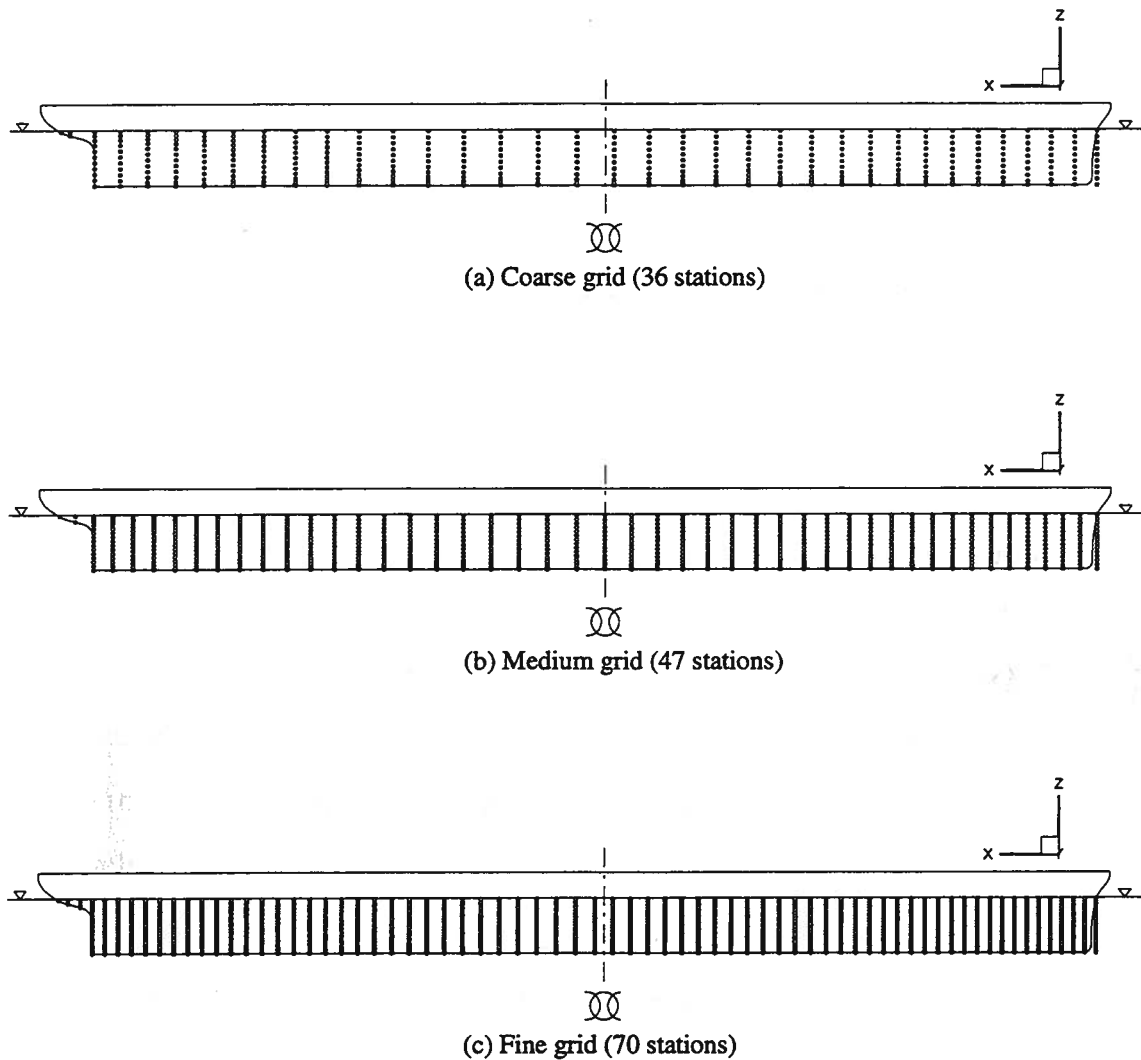
Figure 5.8: Series 60 body grids

The time-step size was to be chosen in accordance with the guideline suggested by Park and Troesch (1992), who investigated the stability of time-marching schemes for a variety of two-dimensional and three-dimensional problems. The guideline suggested

was that the time step, $\Delta t < \sqrt{8 \cdot \Delta x / (\pi g)}$, where Δx was the smallest node spacing in the domain and g, the acceleration due to gravity (9.81 m/s^2). However, in the determining of time-step size, another criterion came to be more stringent: a criterion related to how a likely bow spray sheet was to be suppressed using the previously described bridging technique.

5.2.2.1   Handling of bow spray sheet

For the Series 60, C_B=0.6 at Fr=0.316, and for many other hulls under a variety of conditions, there exists in reality a thin sheet of fluid that shoots upward at the bow (see, e.g., Stern et al., 1996). Not only is this spray sheet not easily captured in the calculations (whether using UM-DELTA or most other methods), but also, numerical instabilities are encountered in the updating of the free-surface in the vicinity of the bow. The instabilities are apparently on account of: (a) the large perturbation velocities induced at free-surface nodes at and very near the stagnation points, (b) the steep gradient in the perturbation velocities as one moves away (in either direction along the body–free-surface intersection line) from the stagnation points , and (c) the fact that the free-surface nodes convect downstream within the method and, thereby, take on slightly different x-locations over the course of a full time-step. A profile of the induced velocities along the innermost free-surface track (which wraps around the body) is shown in figure 5.9. A profile of the velocity potential at those free-surface nodes is also plotted.

Note that while ϕ, the solution in the boundary value problem, has a profile that varies very smoothly along the path, there is much noise in the computed perturbation velocities. This noise is in spite of the fact that the perturbation velocities are computed directly (equation 2.20). Numerical derivatives of ϕ may be taken, but that introduces its own errors. Besides, computing ϕ_z by differentiating ϕ numerically is not easy.
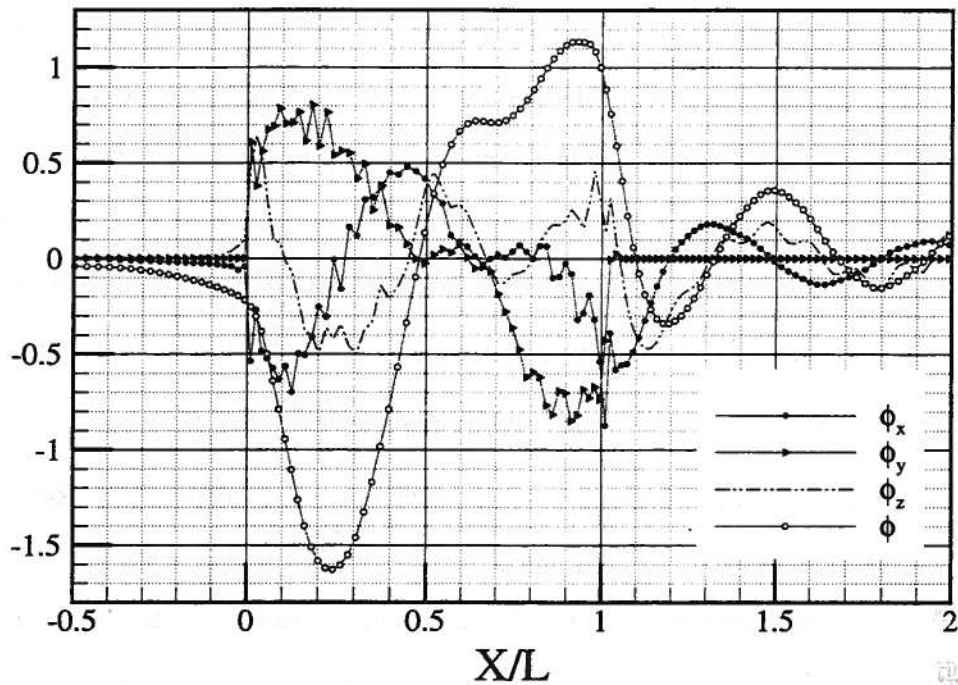
Figure 5.9: Velocity potential and computed perturbation velocities for nodes along the innermost free-surface track

Prior to the development of the bridging technique to suppress wave breaking, these numerical instabilities were smoothed out using an interpolation of perturbation velocities across the free-surface nodes on either side of the stagnation point. The method also has the free-surface grid set up in such a way that the free-surface nodes nearest to the stagnation points are slightly away (in the transverse direction) from the stagnation points. The successful calculations presented in Subramani et al. (1998b), in fact, incorporated these strategies. However, such a smoothing proved not to be robust enough to overcome the numerical instabilities all the time.

The bridging technique described in Chapter 3 not only enables a suppression of wave breaking, it may also be used to iron out such spray-sheet-related numerical

instabilities reliably. There are, however, two minor differences as regards how the technique is invoked for this application. Firstly, since the technique is to be applied at known locations, the two-dimensional curvature along the free-surface track that runs along the centerline and wraps around the body is not inspected. Rather, the bridging technique is explicitly invoked (at all times) for nodes in so-called "spray zones"— regions in the vicinity of the stem–free-surface and stern–free-surface intersections. The rest of the procedure is as before: after the boundary value problem has been solved at a particular instant of time, the computed growths, $\frac{\delta\eta}{\delta t}$ and $\frac{\delta\phi}{\delta t}$ (from the free-surface boundary conditions) are not used to update the free-surface position and potential for nodes in the spray zones. Instead, although the nodes continue to be a part of the boundary value problem, their updated η and ϕ values at each new instant of time are obtained by simply fairing through the neighboring nodes.

The second modification relates to how the spray zones are marked off; the need for the modification arises because the free-surface nodes are prescribed to convect downstream over the course of a time step. (The free-surface nodes are re-gridded back to their original x-locations at the end of each major time step.) Now, if the free-surface nodes were stationary in the x-direction, it would suffice if the spray zones were explicitly marked off as simply the regions that lie within a certain distance, Δx of the stagnation points (at the bow and stern). However, if the spray zones were so marked, it may easily arise that a free-surface node over the course of a full time step lies within a spray zone during one intermediate time step and outside during a subsequent intermediate time step. (Recall that the time-integration scheme used is the 4th order Runge-Kutta scheme, within which each major time-step consists of four intermediate time-steps.) The possible consequences are illustrated in figure 5.10.

Figure 5.10 (a) shows the free-surface nodes that lie outside a fixed-in-X spray zone (top) and the wave elevation profile that results from the fitting of a cubic spline through those nodes. Figure 5.10 (b) shows the node positions one intermediate time step later (top). As a result of the downstream convection, one of the free-surface nodes that was inside the spray zone in the previous intermediate time step is now just downstream of the spray zone. This node's elevation is not only directly computed now, but it also goes into the cubic-spline fit. Considering the difference between the faired-through elevation and the susceptible-to-noise, computed elevation at this node location, the inclusion of this node in the cubic-spline fit results in additional noise that turns out to be destabilizing.

Therefore, the modification adopted is to have the spray zone not be rigidly defined on the basis of a Δx. Instead, when the free-surface grid is set up, nodes that lie within a chosen Δx of the stagnation points are flagged as defining the spray zones. Once flagged, these nodes are faired through over the entire time step, thereby precluding the noise that crept into the problem in figure 5.10.
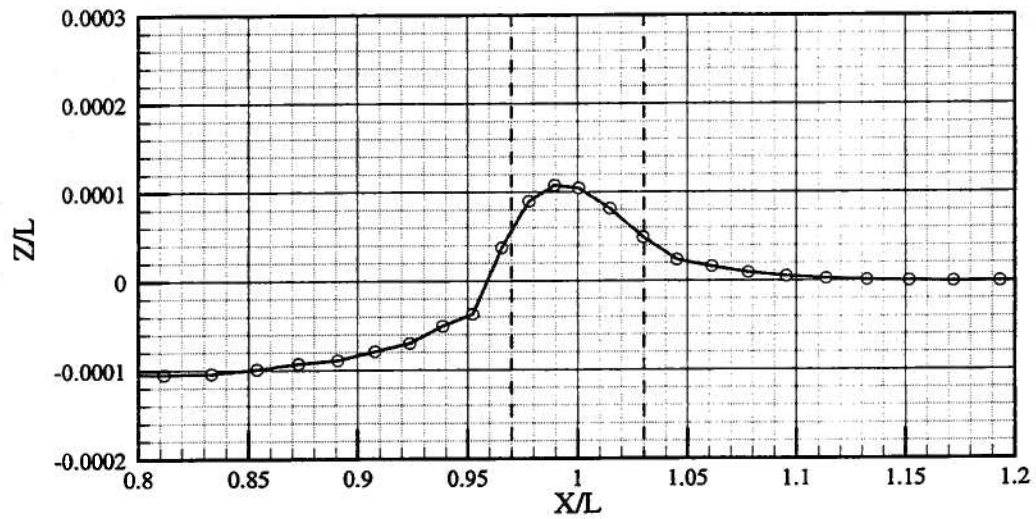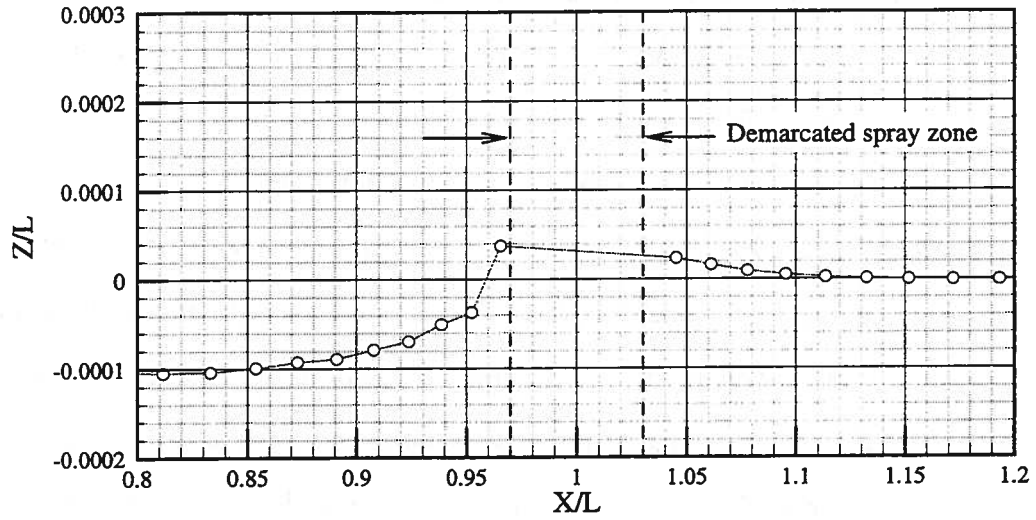
(a) At a particular instant, t

Figure 5.10: Snapshot showing the fairing process for a fixed-in-X spray zone
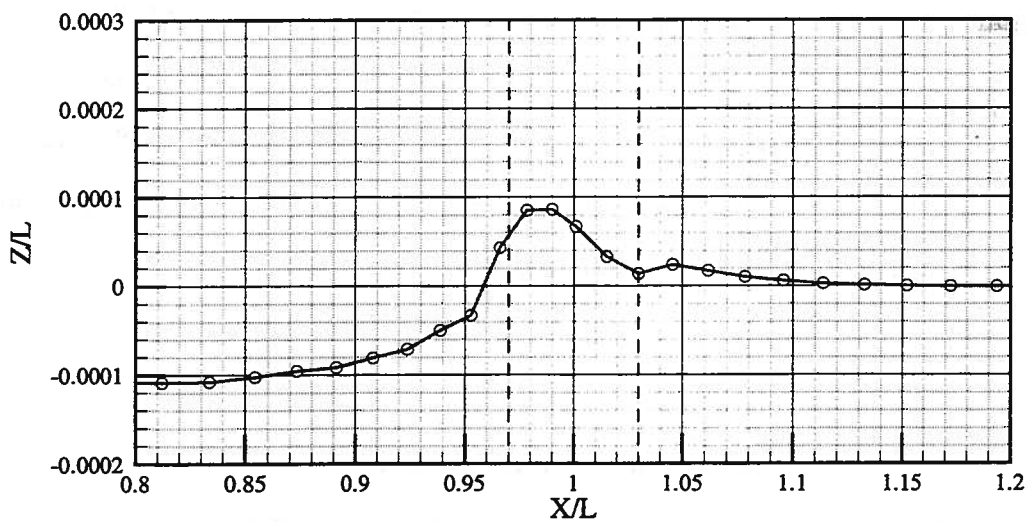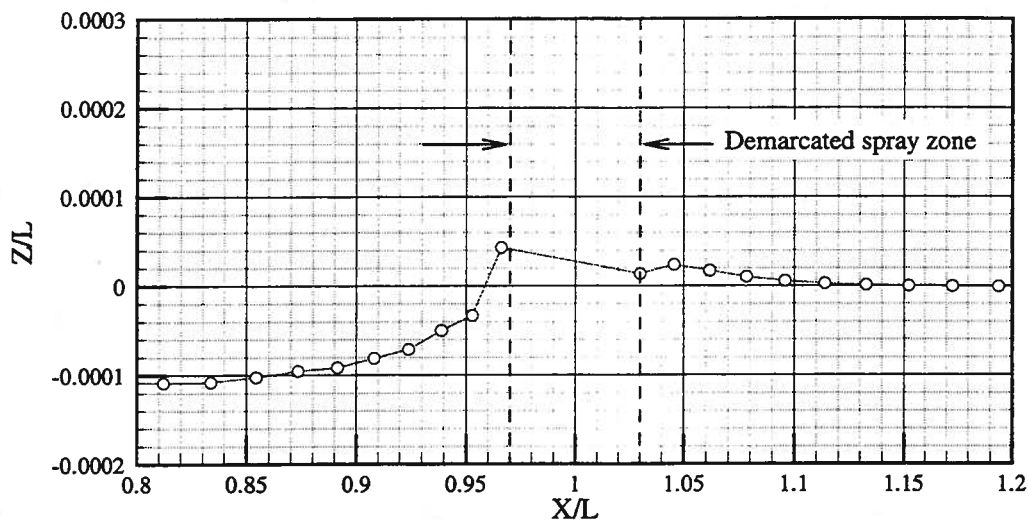
(b) One intermediate time step later

Figure 5.10: continued

The choosing of the flagged nodes is done on the basis of the following considerations. For a calm-water calculation at a chosen Froude number (the steady-state boat speed being a corresponding U_b) and time step, Δt, a free-surface node in the vicinity of the stagnation points can theoretically move downstream by a distance, $U_b \cdot \Delta t$ over the course of a full time-step. As a result, a node that is $U_b \cdot \Delta t$ upstream of the bow

at the beginning of a time step could, towards the end of a full time step, be right at the bow and susceptible to numerical instabilities. Therefore, each of the two spray zones is set up such that free-surface nodes are flagged over a distance, $\Delta x = l_s (U_b . \Delta t)$ upstream of the bow and stern stagnation points. The factor, l_s is to have a minimum value of one; in practice, it is chosen to be slightly higher (between one and two, usually). The spray zones are also extended by an equal distance downstream of the stagnation points, for stability in the calculations.

The setting up of the spray zones has implications on the appropriate time step size for the calculation. In accordance with the guideline of Park and Troesch (1992), the minimum time-step size for, e.g., the medium grid discretization described previously would be $\Delta t \leq 0.30$. For a ship of length, 20 m and for Fr=0.316 (hence, U_b=4.43 m/s), if a time-step size of 0.25 and l_s=1.5 were chosen, the spray zone would extend over 1.66 m at each end of the hull. In percentage terms, the spray zone would cover a high 8.3% of the ship length at each end, surely resulting in a large loss of resolution of the wave profile.

The time-step size was chosen instead in accordance with a more stringent consideration: having the spray zone extend to less than 4% of the ship length at either end. Therefore, for the Series 60, C_B=0.6 at Fr=0.316, Δt was picked to be 0.1 across all the three grids, with l_s set at 1.5.

5.2.2.2   Calm-water results

In the time-domain calculations, the ship is started from rest and accelerated gradually to a steady-state forward speed, while being restrained to float at its design water line. The instantaneous body velocity is given by

$$U_o(t) = U_b\left(1 - e^{-(\alpha g L)t^2}\right)$$
(5.2)

where U_b is the steady-state boat speed, g is the acceleration due to gravity, L is the ship length between perpendiculars, and α is an acceleration parameter. In the Fr=0.316 calculation, α is prescribed to be 0.05 such that steady-state flow is attained within about t=25s.

Figure 5.11 shows a perspective view of the free-surface and wave elevation contours ($\Delta Z / L = 0.0005$) at steady state for Fr=0.316, computed on the fine grid. While the calculations were performed in the half-domain, the entire domain is depicted in the figures, for illustrative purposes. The computed wave profile along the hull for the three different discretizations considered is presented in figure 5.12 and compared with the experimental measurements of Longo and Stern (1996). Like the calculation, the experimental data are for a hull restrained to float at its design water line. The differences in the results for the three different grids, while perceptible, are very small, and the calculations show reasonably good agreement with the data. However, some differences do exist between the calculations and the data: an underprediction of the body–free-surface intersection and bow wave crest, a slight shift in the bow wave trough, a slightly overpredicted and shifted stern shoulder wave, and an underpredicted stern wave crest.

(a)

(b)
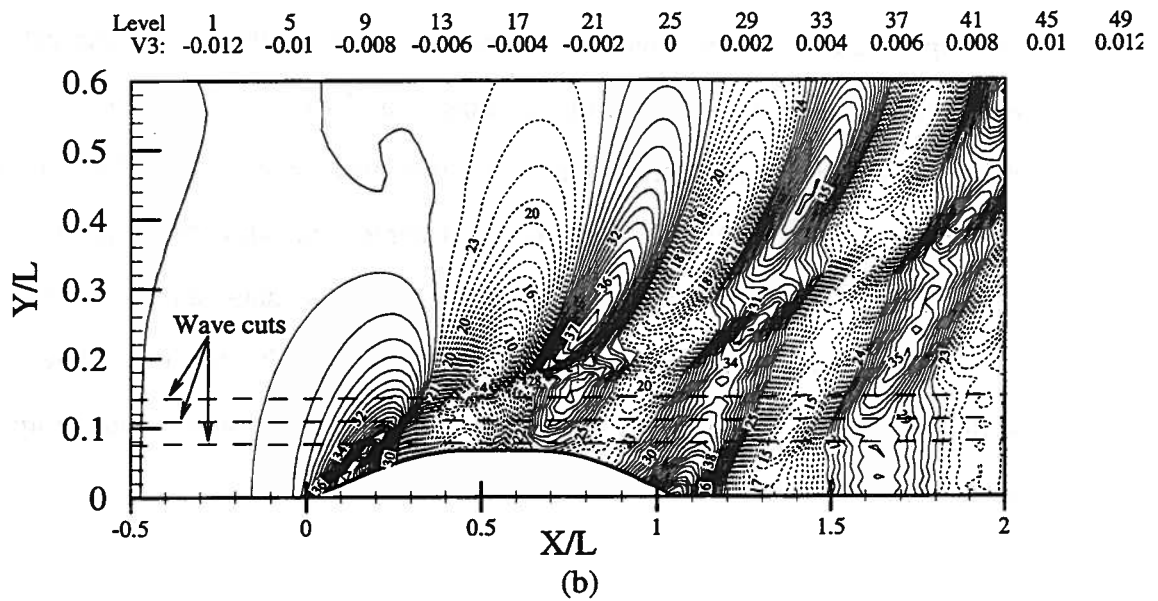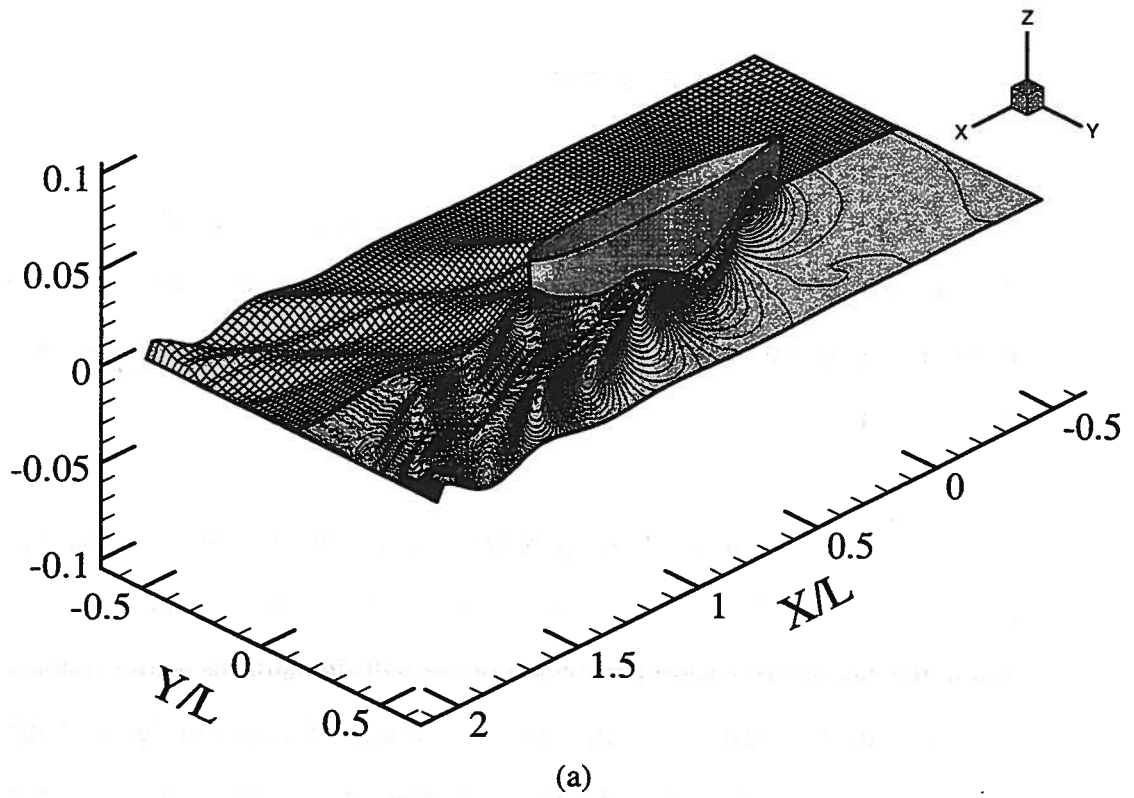
Figures 5.11: (a) Perspective view of the free surface and (b) wave elevation contours at

steady state for the Series 60, C_B=0.6 hull at Fr=0.316 (fine grid)

The underprediction of the water-level at the stem–free-surface intersection line may be due to the simplification, in the numerical method, of the Series 60, C_B=0.6's bow as a line bow of zero radius of curvature. Given the capability of HULLGEO to handle raked bows, the calculations could be repeated without the simplifications, in a more detailed study on the computed bow flow. However, there is another, significant reason for the decreased bow wave crest in the present calculation: the use of the bridging technique to suppress spray-sheet-related numerical instabilities. As previously mentioned, successful calculations had been obtained earlier for the Series 60, C_B=0.6 hull without the use of the bridging technique (Subramani et al., 1998b). Figure 5.13 compares the wave profile along the hull as obtained in the old calculations and using the present approach. The differences are most striking in the decrease of the bow and stern wave crests in the present calculation. These differences are related directly to the "conservative" treatment resulting from the bridging technique, and may be seen as part of a trade-off between accuracy and stability.

Figure 5.14, which presents a comparison of longitudinal wave-cuts (as computed on the fine grid) with the available data—at Y/L=0.0755, 0.1082, and 0.1411—provides an indication of the accuracy of the computed wave field. The inviscid calculations are in good agreement with the data over the length of the ship.
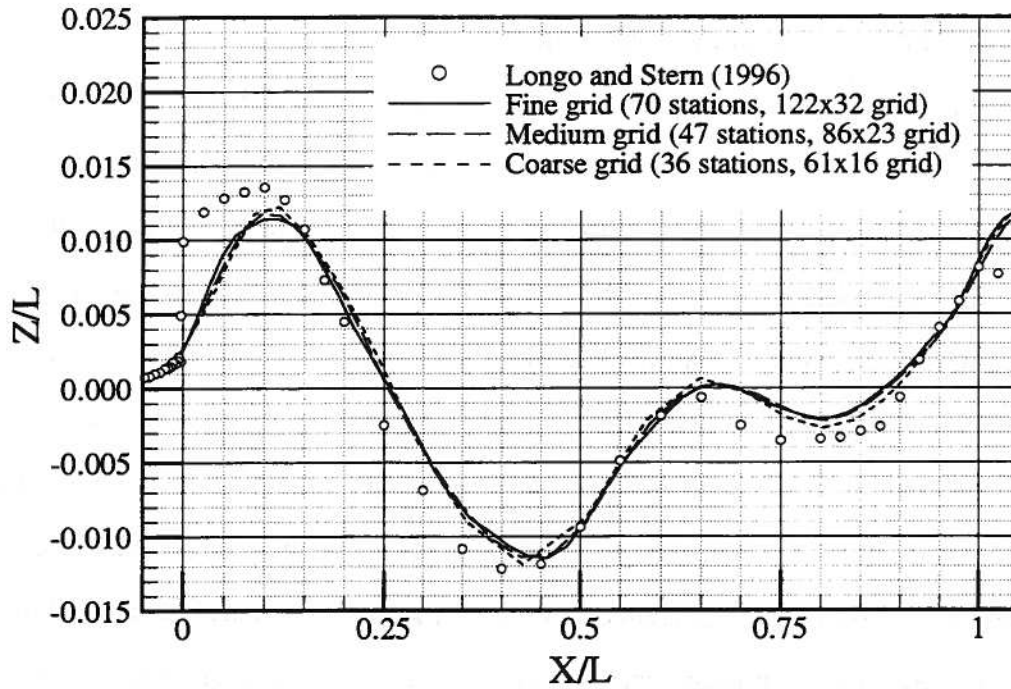
Figure 5.12: Wave profile along the hull for the Series 60, C_B=0.6 at Fr=0.316
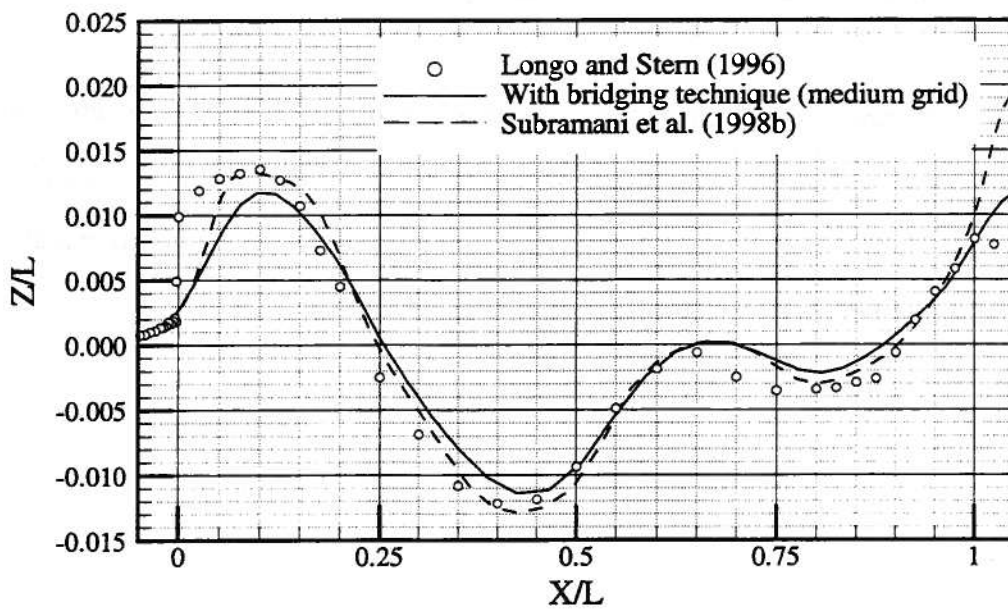
Figure 5.13: Effect of the bridging technique on the computed wave profile along the

hull for the Series 60, C_B=0.6 at Fr=0.316

(a) Y/L=0.0755

(b) Y/L=0.1082

(c) Y/L=0.1411
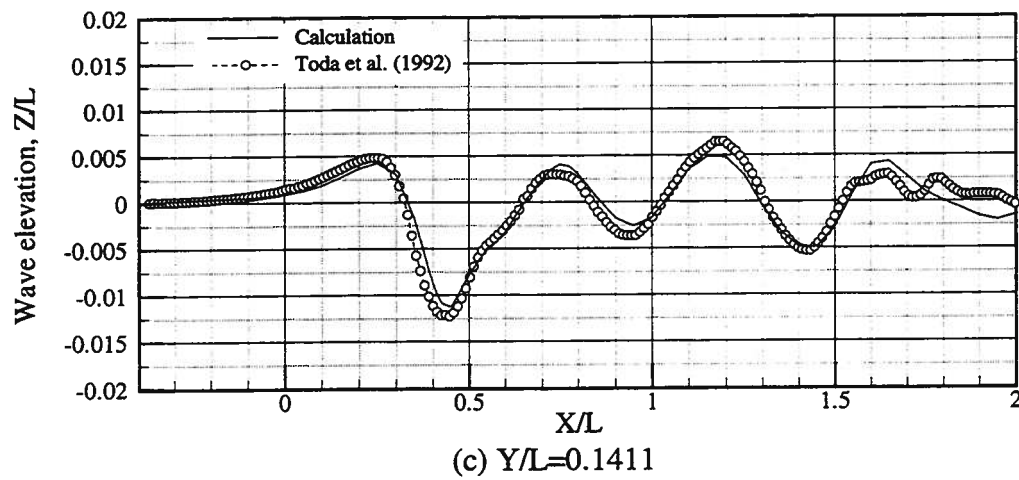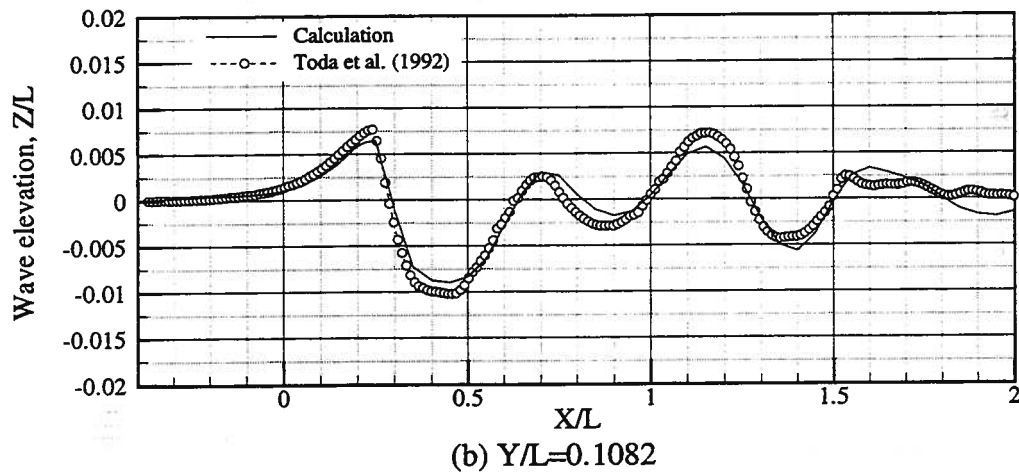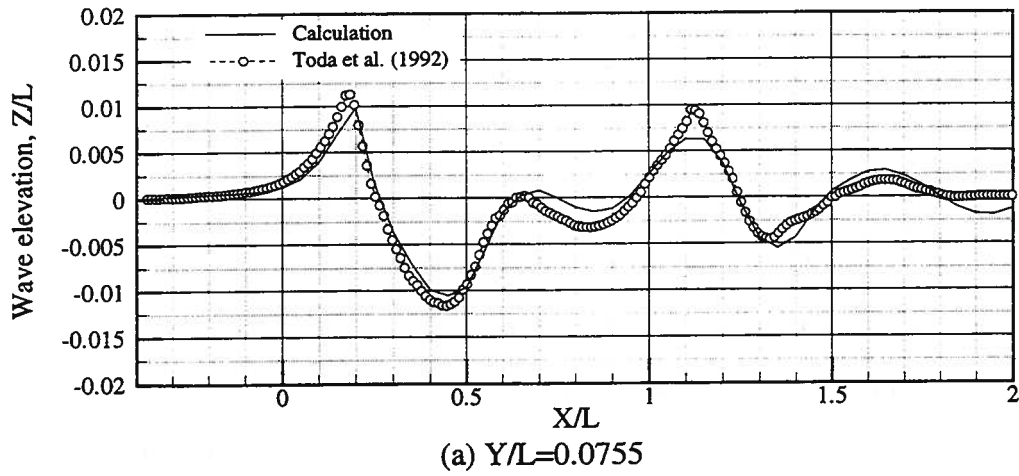
Figures 5.14: Comparison of longitudinal wave cuts for the Series 60, C_B=0.6

at Fr=0.316

5.2.2.3 Wave resistance computation

In these time domain calculations, the wave resistance, sinkage force, and trimming moment are computed at each time step by integrating the pressure over the wetted body surface. However, since the body motion is already prescribed and is independent of the hydrodynamic forces and moments, the computation of the forces and moments is allowed to lag behind the simulation by one time step. That is, if the simulation is at the nth time step, the pressure on the discretized body surface is computed at the $(n-1)^{th}$ time step:

$$p^{n-1} = -\rho \left(\frac{\delta\phi}{\delta t} \right)^{n-1} - \rho g z^{n-1} - \rho \left(U_o \frac{\partial\phi}{\partial x} \right)^{n-1}$$
$$- \frac{1}{2}\rho (\nabla\phi \cdot \nabla\phi)^{n-1} + \rho \left(\frac{\delta\bar{x}}{\delta t} \right)^{n-1} \cdot \nabla\phi^{n-1} \qquad (5.3)$$

This is done specifically so that central differencing (instead of the less-accurate backward differencing) may be used in computing the time derivatives of the potential and node positions on the body:

$$\left(\frac{\delta\phi}{\delta t} \right)^{n-1} = \frac{\phi^n - \phi^{n-2}}{2\Delta t} \qquad (5.4)$$

$$\left(\frac{\delta\bar{x}}{\delta t} \right)^{n-1} = \frac{\bar{x}^n - \bar{x}^{n-2}}{2\Delta t} \qquad (5.5)$$

where Δt is the time-step size and $\bar{x}$ is the position vector in the inertial system.

The forces and moments are then computed using equations (2.13) and (2.14), respectively. The integrations are first carried out along each body station; the sectional pressure force integrands are then integrated longitudinally, across the length of the wetted hull. All the integrations are carried out using Simpson's rule.

A few issues arise that had been hidden behind the fore-aft symmetry nature of UM-DELTA's previous applications (the mathematical Wigley hull, specifically). To illustrate the first issue, consider the plumb bow of the Series 60, C_B=0.6 hull. As illustrated in figure 5.5, the unit normals along the vertical bow at zero angle of attack are $\bar{n}$ = (-1, 0, 0). These are the right values for the stagnation flow at the bow. However, combined with the high stagnation pressure, these unit normals result in an unrealistically exaggerated contribution to the computed wave resistance. When there exists fore-aft symmetry, these high contributions at the bow and stern tend to cancel each other, and the anomaly is not noticed. The practical Series 60, C_B=0.6 parent hull form, however, lacks fore-aft symmetry, and this led to inaccuracies in the computed wave resistance, chiefly in the computing of the components (see equation 2.11) that include $\frac{\partial \phi}{\partial x}$.

Therefore, the following study was undertaken. The two portions of the hull where stagnation flow is observed ($n_x = -1$) were separated out from the pressure integration for the wave resistance, as depicted in figure 5.15. The pressure over the rest of the hull was integrated as previously described. The two omitted regions were approximated as vertical stacks of two-dimensional wedges (in the X-Y plane) in a uniform stream, and the force over each wedge-like region was determined analytically. The wedge-flow approximation is based on the Schwarz-Christoffel transformation and follows the analysis of Hildebrand (1965; sec. 10.20). The analysis is detailed in Appendix D.
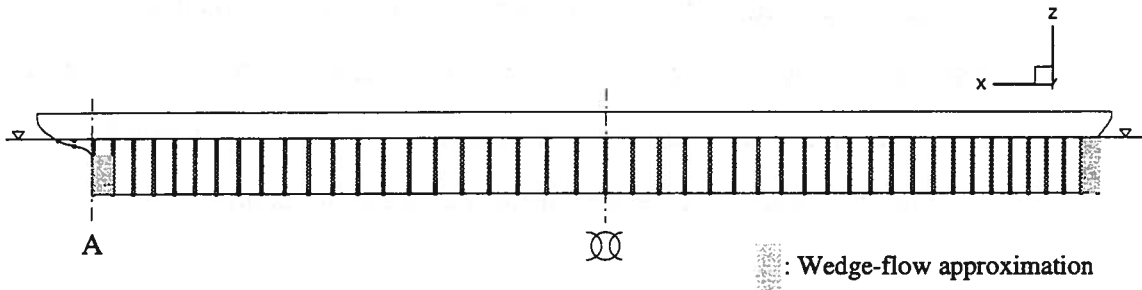
Figures 5.15: Sketch showing the wedge regions of the Series 60, C_B=0.6 hull that are separated out from the pressure integration

The analytically-obtained contributions to the wave resistance were added to the contribution obtained through the pressure integration over the rest of the hull. The total wave resistance coefficient was computed to be 1.758 x 10^{-3}. Kim and Jenkins (1981) determined the wave resistance for the Series 60, C_B=0.6, in the fixed and free-to-sink-and-trim orientations, over a range of Fr. Their experimental measurements of the wave resistance (obtained using a wave pattern analysis) and residual resistance coefficients for a fixed hull at Fr=0.32 were 1.316 x 10^{-3} and 1.850 x 10^{-3}, respectively. Note that the resistance coefficients have been obtained through a non-dimensionalization by $0.5\rho U_b^2 S$, where ρ is the density of water, U_b is the steady-state forward speed, and S is the wetted surface area (scaled down from 2534.4 m^2, which is the wetted area for the full-scale ship of length between perpendiculars, 121.92 m). This slight overprediction is consistent with the wave resistance calculations previously performed, using the UM-DELTA method, for the Wigley hull.

Following this successful study, the wave resistance was computed again and through a pressure integration over the entire wetted hull surface. The wedge-flow approximation was discarded, but the pressure integration over the stagnation regions was

modified in the following way. The unit normals at the stagnation points in the wedge regions sketched in figure 5.15 were, for use in the pressure integration alone, taken to be consistent with the shape of the local panels. These modified, *force* unit normals are depicted in figure 5.16. Also, the longitudinal pressure integration was split at the station marked A in figure 5.15. This was done so that erroneous answers did not result when the spike in the sectional pressure force integrand at that station was fed through Simpson's rule. The wave resistance computed by pressure integration was found to be 1.709×10^{-3}, comparing well with the previous calculation (a difference of 2.8%) and the experimental data. Note that the error in the hydrostatic pressure force in the x-direction—a quantity theoretically zero—was 0.084×10^{-3}. The vertical hydrostatic force differed from the still-water displacement by 0.70%.
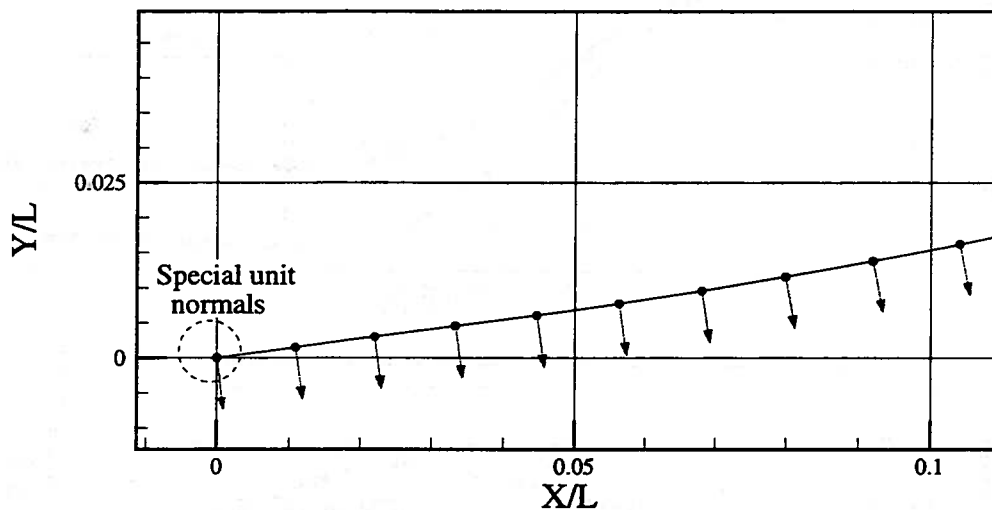
Figures 5.16: Depiction of *force* unit normals at the bow of the Series 60, C_B=0.6 hull

Lastly, the non-dimensional surge and heave forces and pitch moment (non-dimensionalized by $0.5\rho LU_b^2 S$) and their components are plotted in figure 5.17. The pitch moment is taken about the origin, with a positive moment corresponding to bow-up trim. The component forces and moments come from an integration, over the wetted hull

surface, of each term in the pressure equation (5.3). For clarity, only every fourth data point (0.4 s apart) is shown. The small but perceptible sudden jump in a few surge force components at about 10 s is a result of observed jumps in the unit normals at station A (as marked in figure 5.15).
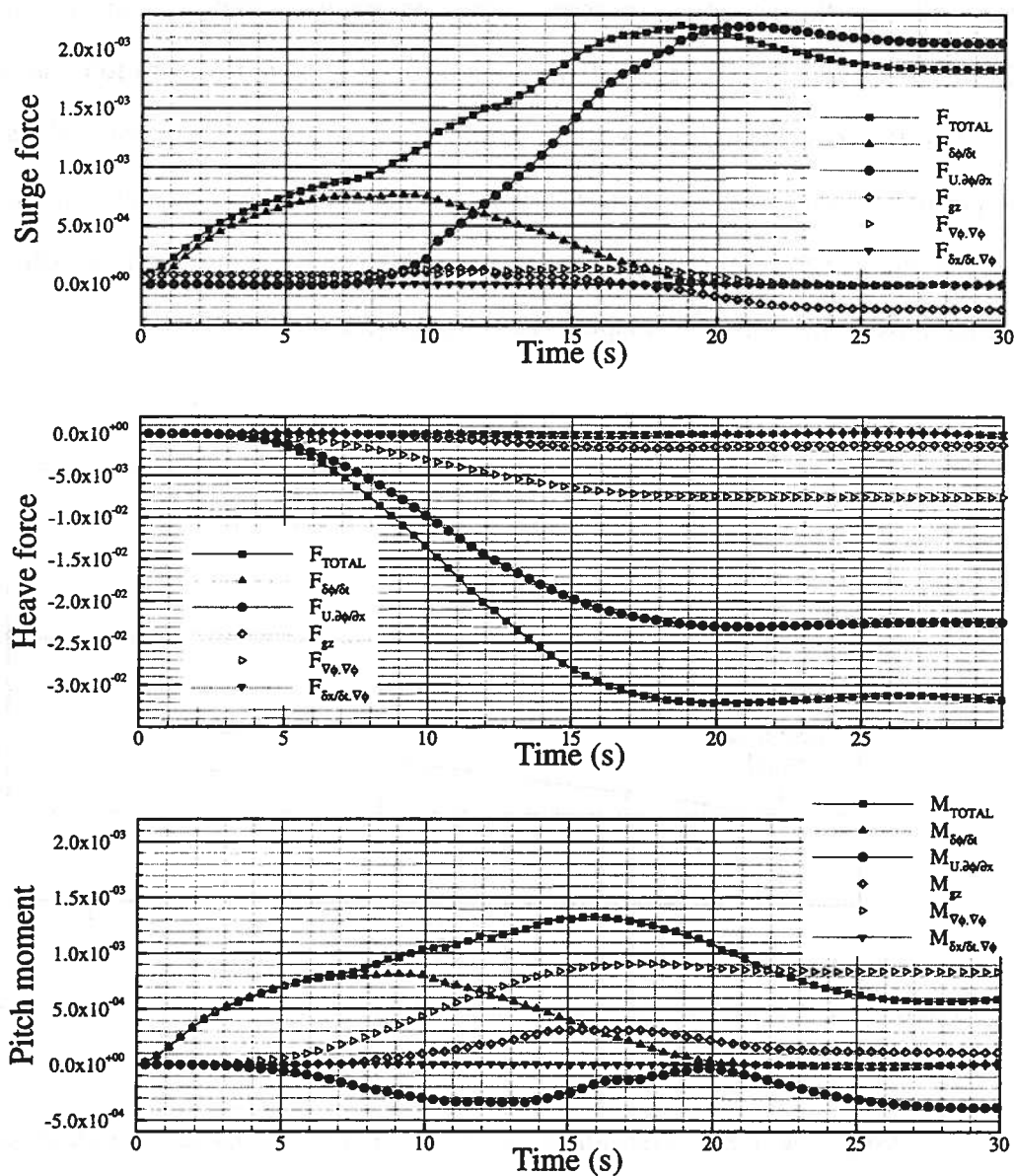
Figure 5.17: Non-dimensional surge and heave forces and pitch moment for the Series 60, C_B=0.6 hull in calm water at Fr=0.316

The computational requirements for these calm-water calculations were as follows. The coarse grid calculation required about 11 MW of memory and 24 minutes (while clocking 260 MFLOPS) on a CRAY T-90. The medium grid calculation required about 23 MW of memory and 59 minutes (while clocking 360 MFLOPS) on a CRAY T-90. The fine grid calculation required about 67 MW of memory and 3.62 hours (while clocking 494 MFLOPS) on a CRAY T-90. Note that the high degree of vectorization within the UM-DELTA has it operating occasionally at over 600 MFLOPS on a CRAY-T90 processor that has a peak speed of 2 GFLOPS.

5.3   Transom-sterned vessels: DDG5415 model and D1 fast monohull

Much of the thrust for UM-DELTA's development comes from the interest in application of the method for the seakeeping analysis of modern naval combatant designs. These are typically transom-sterned vessels with complex geometrical features such as bulbous bows, skegs, and peculiar appendages. They have distinctly different hydrodynamic characteristics from cruiser-sterned hulls such as the Series 60, C_B=0.6. In particular, as seen in the two-dimensional calculations presented in Chapter 4, these hulls are designed such that the flow separates cleanly from the edge of the transom. The calculations for real, three-dimensional transom sterns are much more difficult to model than the two-dimensional calculations. This is partly due to the geometrical complexities and partly a result of the complexities in the real flow itself. There are also limitations to inviscid flow theory, as regards an accurate modeling of such flows. Nevertheless, inviscid flow methods hold promise for useful seakeeping computations.

Two transom-sterned models were chosen for calm-water calculations under the present project: the DDG5415 naval combatant model and the D1 fast monohull. The

models are shown in figure 5.18. The DDG5415 is a towing tank model developed by the United States Navy as a representative of modern surface combatants, and it has come to be an important test case in the validation of advanced computational methods. Experimental data for this model have been collected at the Naval Surface Warfare Center (NSWC; Ratcliffe, 1998). The model is also part of an ongoing collobarative study involving the NSWC and labs at the IIHR, Iowa and INSEAN, Italy (see, Longo and Stern, 1998 and Olivieri and Penna, 1999) . The D-Series of fast displacement ships is a line of parent hull forms that have been extensively studied, through physical and numerical experiments, at the Technical University of Berlin (e.g., Nowacki et al., 1999). The studies were part of efforts to minimize ship resistance through hull-form modification.

In the sections to follow, the panelization of the hull and the free surface are first discussed. Next, results are presented for the DDG5415 at Fr=0.28, for the separate cases of stagnation and smoothly-separating transom stern flow. Lastly, results are presented for the D1 hull at Fr=0.433, a case in which a steep, breaking rooster-tail wave crest is observed aft of the transom during the transition to smoothly-separating flow. The use of the previously described bridging technique to suppress such wave-breaking is demonstrated.

(a)

(b)
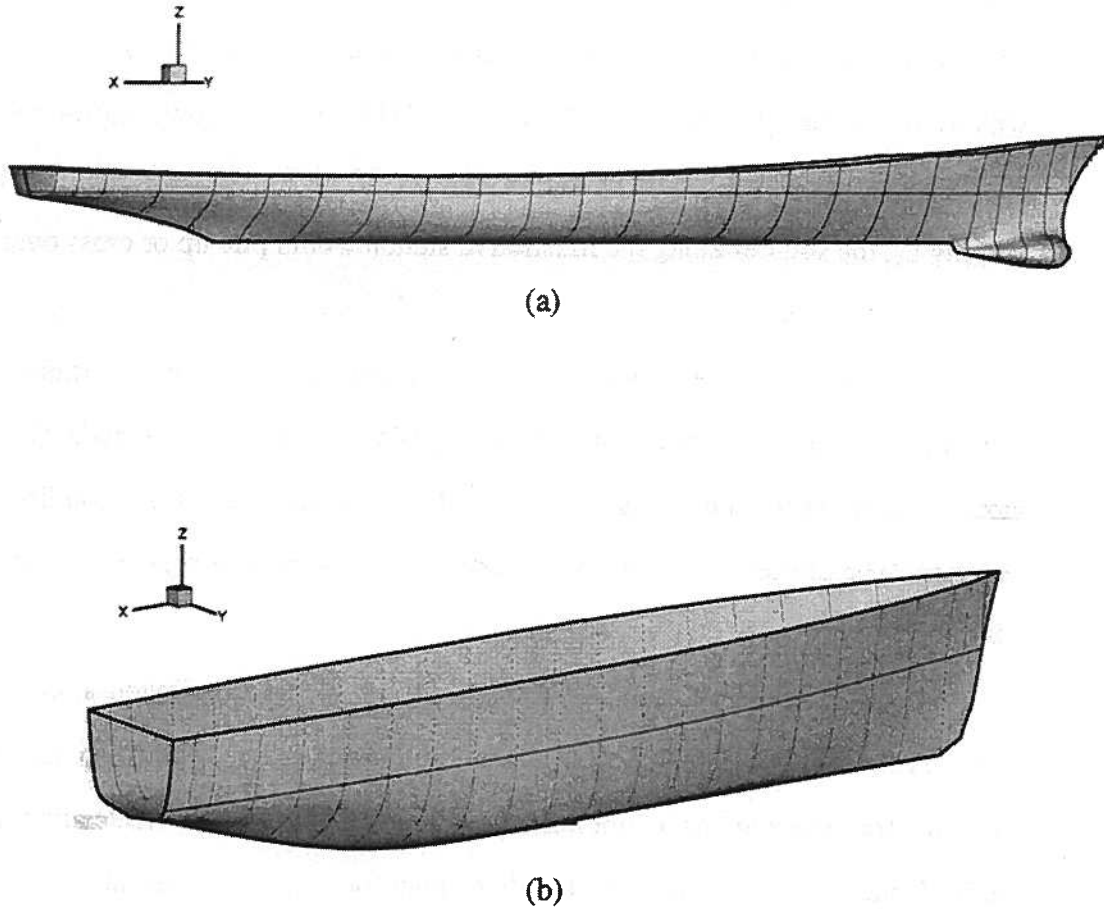
Figure 5.18: Perspective view of: (a) the DDG5415 combatant and (b) the D1 fast monohull

5.3.1 Treatment of bulbous bows, transom sterns, and the free surface

Distinguishing features of the two models are that the DDG5415 has a bulbous-bow-like sonar dome while the D1 has a raked stem. Both, of course, also have a transom stern and an aft profile that slopes gently along the centerline. Some of the

issues that were covered in section 5.2.1, regarding the gridding of the body and the treatment of the stagnation points, apply to the present hulls too. For instance, the sources corresponding to body nodes along a station are not prescribed a constant desingularization distance but one that varies smoothly from 0.01 to 1.0 L_d. Figure 5.1, which shows the discretization of the DDG5415 model's bow, shows the improved source distribution that results from this change. If not for the prescribing of a smoothly varying L_d, the sources along the illustrative station would pile up or cross over.

Also, the stem rakes of both hulls are closed off in a manner similar to how the stem rake of the Series 60, C_B=0.6 hull is gridded: using a point node that climbs up along the stem as the hull picks up speed and the free-surface intersection line rises along the stem. The presence of a transom, in addition, calls for further special treatment.

Figure 5.19 shows how additional body nodes are distributed along the transom face. The nodes are initially at z=0, the calm-water level. Note that the body nodes along the transom edge have unit normals that point into the hull while almost entirely in the Y-Z plane (i.e., negligible n_x for these body nodes). As a result, there is open the possibility that the sources corresponding to these edge body nodes may get unfavorably close to the transom face body nodes. To avoid this scenario, the transom edge body nodes' sources are prescribed a much-reduced L_d of 0.05. The sources corresponding to the transom face body nodes too are given a reduced L_d (again, of 0.05), lest they collide with the sources corresponding to body nodes along the station immediately forward of the transom face. In figure 5.19, the sources appear to be almost co-incident with the nodes, due to the very small desingularization distance.

The free-surface grid is also set up in a special way for transom stern calculations. With the hull ending abruptly at the transom, rather than closing back in towards the

centerline as in cruiser-sterned hulls, the first free-surface path wraps around the hull and continues on downstream along a straight line. The portion of the free-surface lying in the wake of the transom is then gridded using additional (straight) paths that originate at the transom. A typical grid is shown in figure 5.20, with a mesh plotted over the discrete free-surface nodes. The node density in both, the transverse and longitudinal directions is kept consistent with the "main" free-surface grid. Spatial free-surface derivatives are computed separately on this rectangular grid, using simple central-differencing and second-order-accurate one-sided differences. The additional free-surface nodes in the transom wake are, however, retained as part of the existing tree structure in the setting up of the matrix preconditioner for the entire free surface.
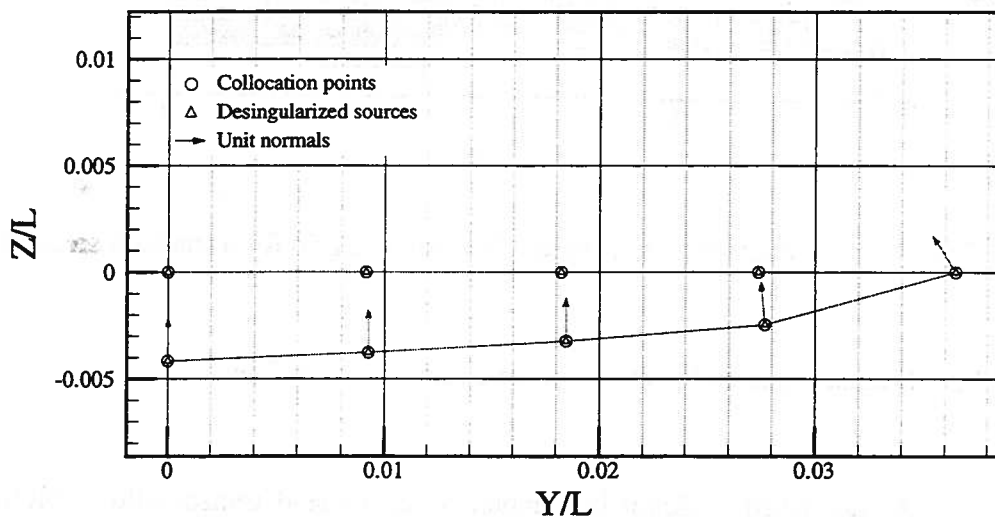
Figure 5.19: Distribution of nodes and sources along the DDG5415 model's transom face and edge

One additional change was made, involving the positions of the nodes and positions for the first row of free-surface nodes in the wake of the transom: the free-

surface nodes were held fixed in the plane of the transom, for reasons of numerical stability in the ensuing calculations.
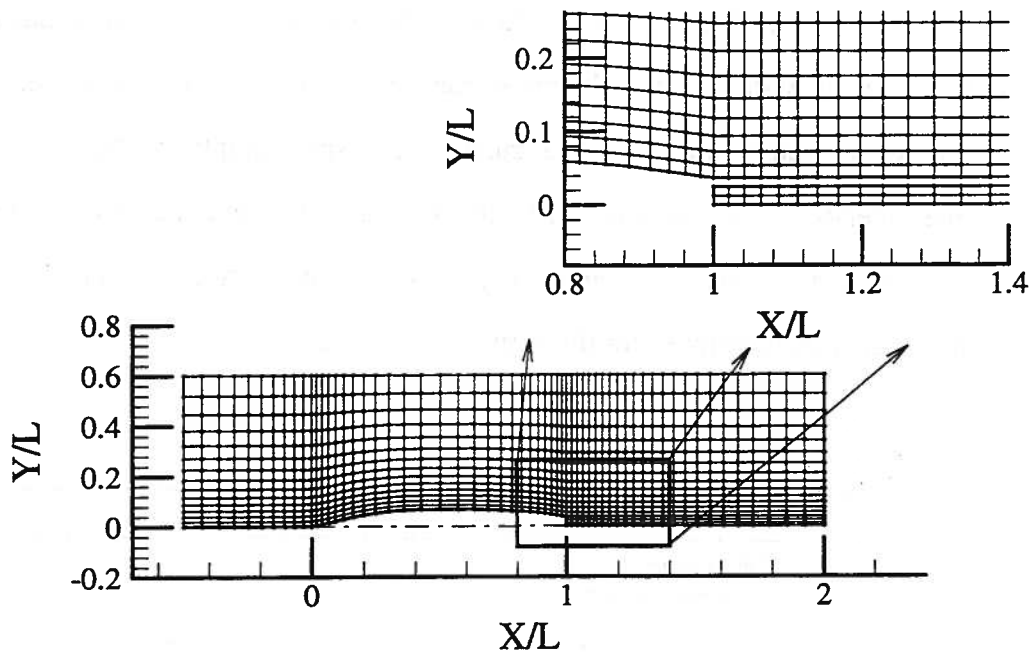
Figure 5.20: Plan view of a typical free-surface grid for a transom stern calculation

5.3.2 Stagnation and cleanly-separating transom stern flow

As described in detail in Chapter 4, an inviscid transom-flow solution naturally tends towards stagnation flow (or solution A), as the hull is accelerated from rest up to its steady forward speed. However, in reality, the flow behaves like solution A at low Froude number and transitions to cleanly-separating flow (or solution B) as the Froude number increases. Numerical artifices, therefore, have to be devised in order to effect a transition from a transom wetted to a transom dry state. In this section, the technique

developed to effect such a transition—as successfully demonstrated for two-dimensional transom stern flows in Chapter 4—is applied to the three-dimensional DDG5415 model.

First, however, the stagnation flow results are described. Calculations were initiated for the DDG5415 accelerated from rest (with acceleration parameter, α=0.05) and advancing straight ahead in calm water at Fr=0.28. [The simulation of the DDG5415 in calm water at Fr=0.28 is, in fact, one of the selected test cases for an upcoming CFD in Ship Hydrodynamics workshop (Gothenburg, 2000).] The hull was fixed, restrained to float at its design water line. Experimental data have been obtained for the hull at this model speed, albeit with the model in the free-to-sink-and-trim condition.

Exploiting symmetry, as before, the calculations are restricted to the half domain, Y>0. A coarse, 35-stationed body grid was selected, with a cross-sectional node density of 9 nodes along a length equal to the ship draft. The total number of nodes on the body was 327. The domain of the numerical wave tank was bounded by an upstream end 0.5 times the ship length ahead of the bow, with the tank extending for 1.0 L downstream of the stern and measuring 0.6 L across (on the side, Y>0). The free-surface discretization was 60 nodes in the longitudinal direction and 15 nodes in the transverse direction, not counting the wake of the transom, where there were three additional nodes in the transverse direction. The number of free-surface nodes ahead of the body, across the body, and downstream of the body were, respectively, 10, 26, and 24. The total number of nodes in the free-surface was 975. The time-step size was to be chosen 0.1, based again on the previously described considerations related to the use of the bridging technique at the bow and stern. The spray-zone length for this run was in accordance with an l_s of 2.0.

Figure 5.21 shows a perspective view of the free-surface at steady state. Note that the free-surface nodes have climbed up the transom face.

Figure 5.21: Perspective view of the steady-state free surface and free-surface contours for the DDG5415 at Fr=0.28—stagnation flow

Next, the calculation was repeated but with the use of the new technique for cleanly-separating flow (involving equations 4.8 and 4.9) described in Chapter 4. One additional modification was made, given the complexities inherent in three dimensions. In obtaining solution A, the body nodes on the DDG5415's transom face were continually re-gridded (at the end of each full time step) so as to track the climbing free-surface. However, this natural means of updating the positions of the body nodes would run into complications in the case of cleanly-separating flow. As the free-surface nodes close in on the transom edge, there would be little room on the transom edge to

accommodate the already existing body nodes on that station as well as the transom face body nodes that descend from above.

While this is chiefly a body-regridding issue (this is discussed further in the sections to follow) which calls for improved regridding strategies, the recourse presently adopted was a simple one: the transom face body nodes were simply retained at the benign, calm-water level through-out the simulation. (Due to this change, the sources corresponding to the first row of free-surface nodes in the transom wake were moved slightly downstream of the transom face—by 20% of the node spacing in the longitudinal direction—lest the descending sources run into the body nodes at z=0.) This would normally result in at least perceptible differences in the solution. The differences would also be noticed in the solution at the nearest free-surface nodes, namely the first row of free-surface nodes in the transom wake. However, with the transom face body sources being prescribed a very small desingularization distance (L_d=0.05), these body sources have negligible influence at any node other than their corresponding nodes. In addition, the elliptical nature of the problem ensures that the solution is little changed at the first row of free-surface nodes in the transom wake.

Following a successful coarse-grid calculation, calculations were undertaken on finer grids: a medium grid consisting of 47 stations and a fine grid consisting of 68 stations. In fact, all three grids—the coarse, medium, and fine grids—were extracted as subsets of a still-finer 140-stationed grid. The different body grids are shown (drawn to scale) in figure 5.22. The node density along a station, in terms of nodes along a girth equal to the ship draft, was 13 for the medium grid and 18 for the fine grid. The total number of nodes on the body was 652 for the medium grid and 1328 for the fine grid.

(a) Coarse grid (35 stations)

(b) Medium grid (47 stations)

(c) Fine grid (68 stations)
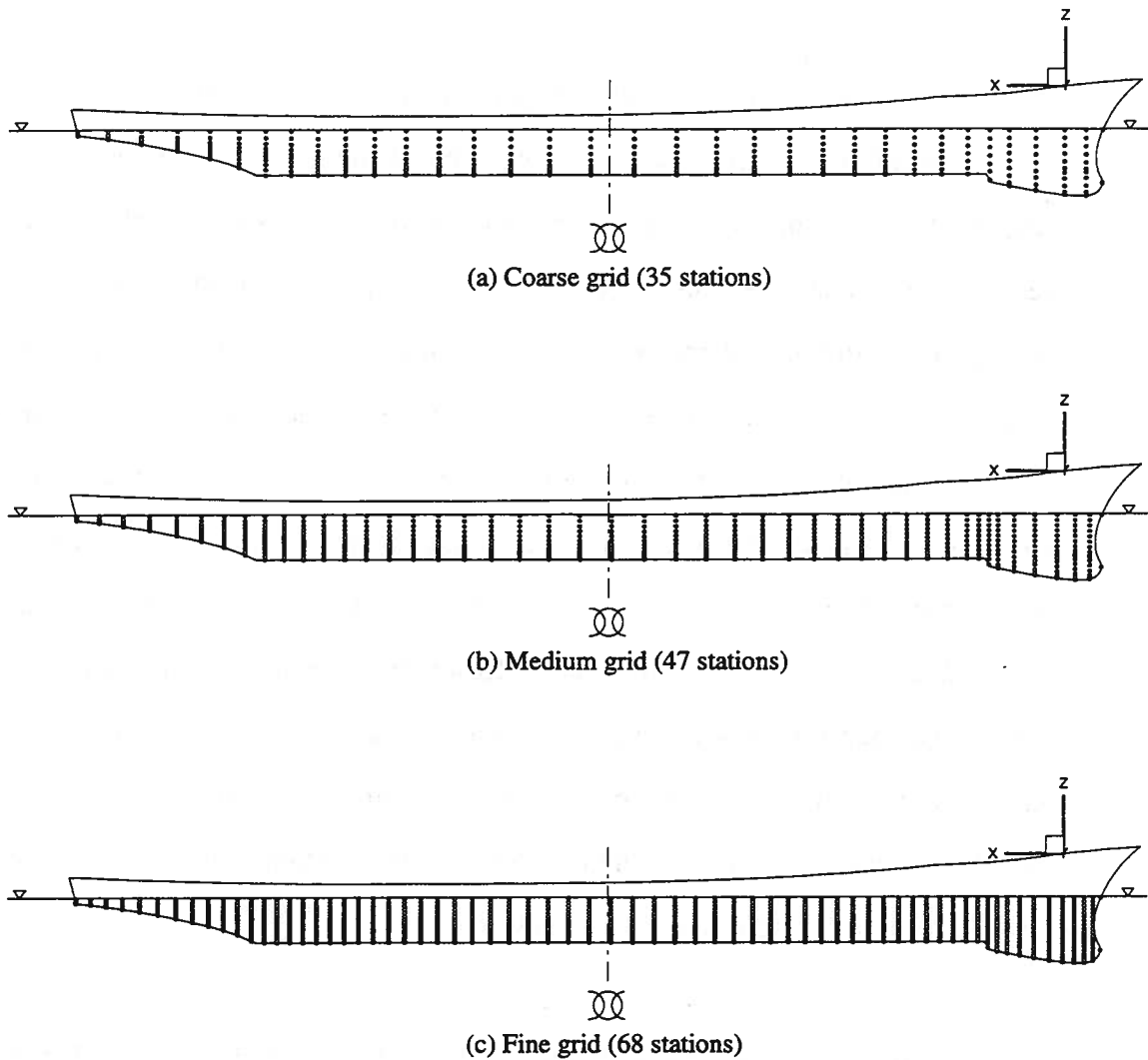
Figure 5.22: DDG5415 body grids, as subsets of a 140-stationed grid

The dimensions of the numerical wave tank were unchanged from the coarse grid calculation. The free-surface discretization, however, was increased to 85x21 for the medium grid, with three additional free-surface tracks in the transverse direction in the

transom wake. For the fine grid, the free-surface grid was 120x30, with four additional transom wake free-surface tracks. For the medium grid, the number of free-surface nodes ahead of the body, across the body, and downstream of the body were, respectively, 14, 36, and 35; for the fine grid, the corresponding distribution was 20, 50, and 50. The total number of free-surface nodes was 1893 for the medium grid calculation and 3804 for the fine grid.

Figure 5.23 shows a perspective view of the free-surface and wave elevation contours at steady state, with the free-surface separating cleanly from the transom edge.

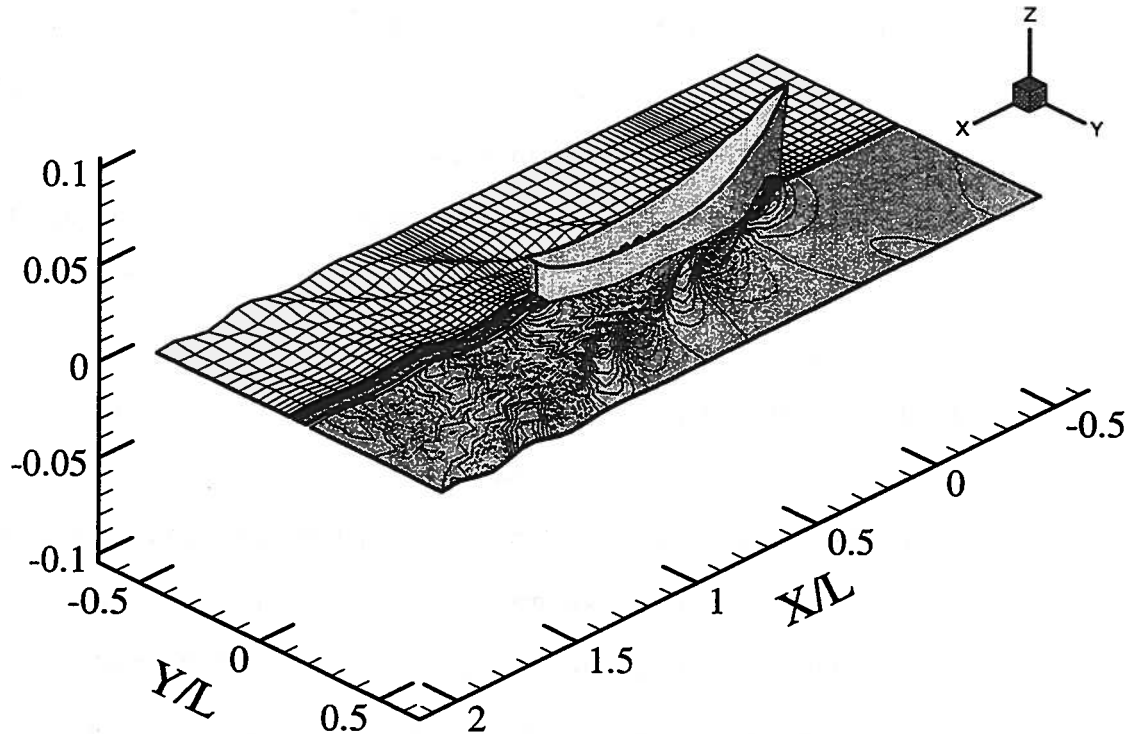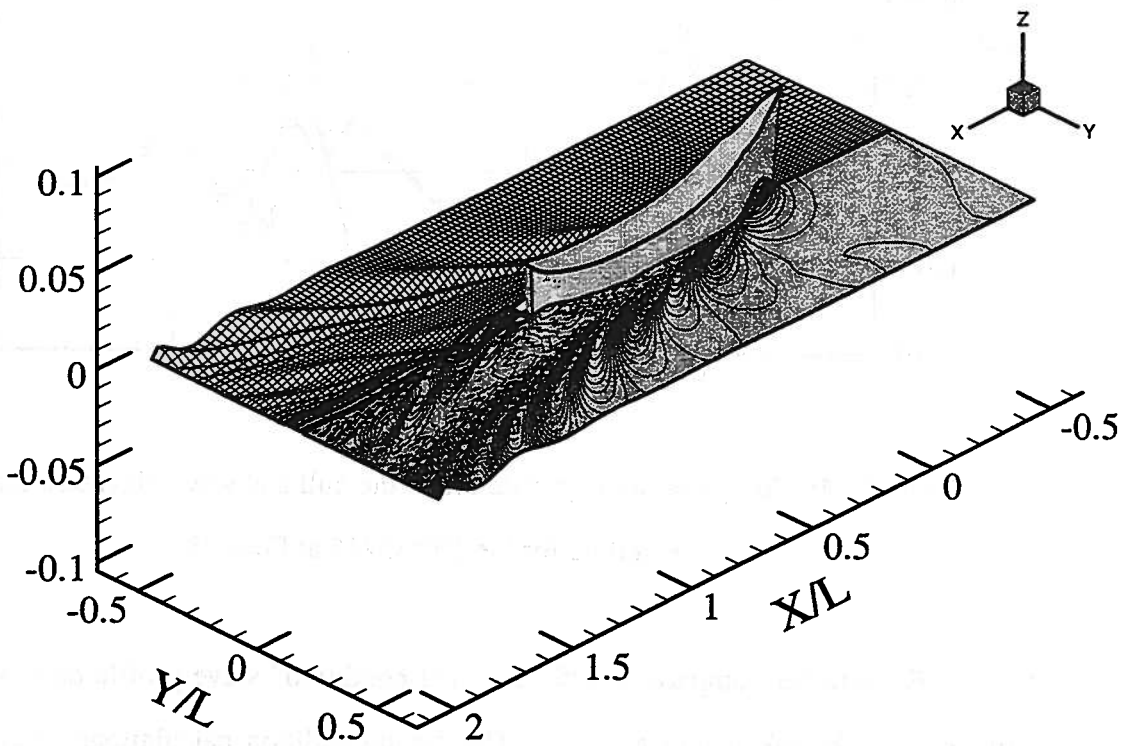

Figure 5.23: Perspective view of the steady-state free surface and free-surface contours for the DDG5415 at Fr=0.28—cleanly-separating flow

Figure 5.24 shows the wave profile along the hull and the wave elevation along the centerline as computed on the three different grids. The convergence between the grids is quite good, although the coarse grid calculation differs perceptibly from the other two calculations near the stern.
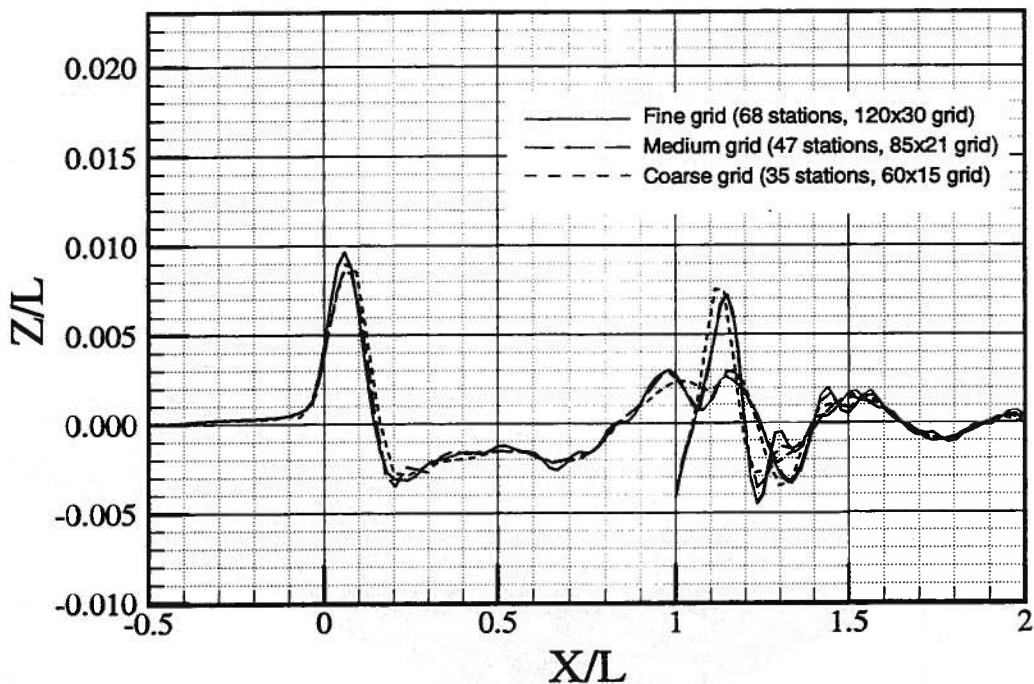
Figure 5.24: Computed wave profile along the hull and wave elevation along the centerline for the DDG5415 at Fr=0.28

For a better comparison with the "free condition" wave profile data, sinkage and trim need to be taken into account. The fixed-condition calculations (measured with respect to the undisturbed free surface) were, therefore, vertically shifted and rotated by the experimental sinkage and trim values. These are, at Fr=0.28, a sinkage of 0.00185 L and a trim (by the bow) of 0.0019 L. Figure 5.25 presents a comparison between the shifted wave profile calculations (now, as measured with respect to the design water line)

and the free-condition data. The calculation captures the features of the data well; however, there is a significant underprediction of the bow wave crest. A part of the underprediction is surely due to the use of the bridging technique over a "spray zone" at the bow, as evidenced by the differences seen in figure 5.13. However, for the differences between the calculation and the data for this hull to be much more significant is indicative of the steep breaking wave that exists at the bow in reality. The significant differences between the two independent data sets shown, especially in the bow shoulder region, are probably a measure of the complex nature of the flow. Longo and Stern (1998) present a photo of the bow flow that shows clearly the nature of the spilling breaker bow wave. The present calculations merely find the bridging technique fulfilling its role of suppressing the breaker, albeit more effectively than may be desired.
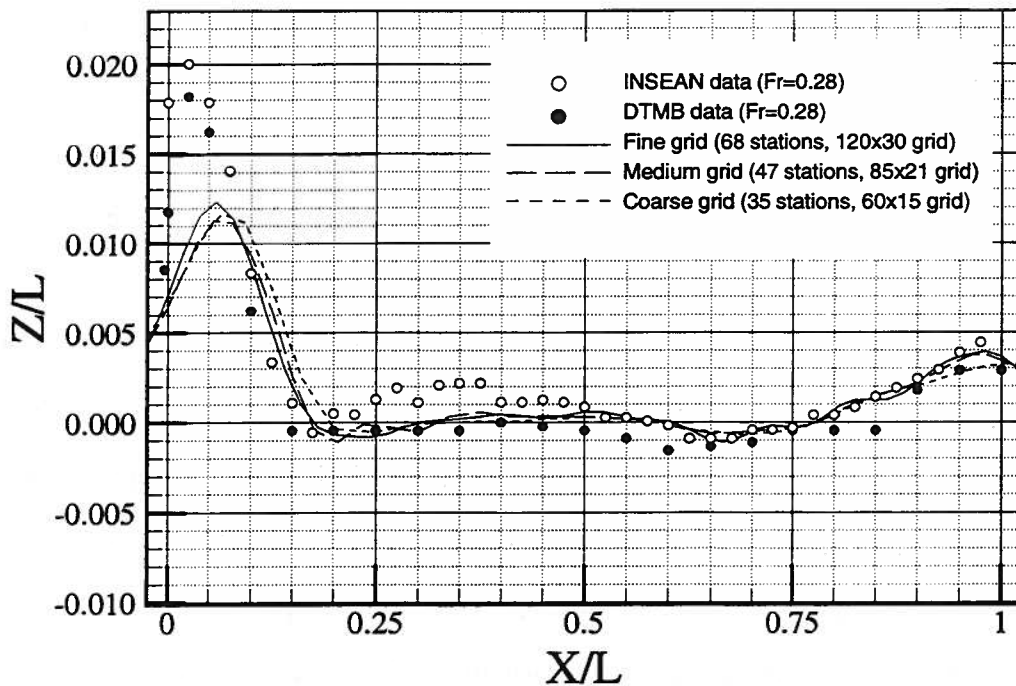
Figure 5.25: Validation of the computed wave profile along the hull for the DDG5415 at Fr=0.28

It is also important to note that some of the differences between the calculations and the data, especially over the bow shoulder, may be due to sinkage and trim. In a recent study, Subramani et al. (2000) reported Reynolds-averaged Navier Stokes calculations for a similar naval combatant model (the FF1052 model) in both, the fixed and free-to-sink-and-trim conditions. Their calculations highlighted the effects due to sinkage and trim. In particular, their Fr=0.29 wave profile calculations for the FF1052 in the free condition captured the mid-body hump better than the fixed-condition calculations was able to (even with a shifting by the appropriate amounts of sinkage and trim).

In figures 5.26 and 5.27, the computed wave field is compared to the data. As is evident from figure 5.26, which compares maps of the wave elevation contours, the calculated wave field is in good agreement overall with the data. The contours are spaced $\Delta(Z/L) = 0.0005$ apart.

Figure 5.27 presents a comparison of the longitudinal wave cuts at Y/L=0.0965 and 0.172. The wave cuts agree reasonably well across the length of the hull up to the transom. There is a slight phase shift, however, in the wave trough at about X/L=0.25 (Y/L=0.0965) and the wave crest at about X/L=0.5 (Y/L=0.172). The differences are more pronounced, however, downstream of X/L=1.0. There is a significant underprediction of the wave crest at about X/L=1.15 (Y/L=0.0965); the calculation also shows a substantial phase shift, with the crest actually present at about X/L=1.25. This underprediction and phase shift is apparent at Y/L=0.172 too, although the differences are smaller. These differences arise as a result of the way in which the method captures the smoothly-separating flow around the corner of and behind the transom. It is, to that

extent, reflective of the limitations of the inviscid model in accurately calculating the highly turbulent wake behind transom sterns.
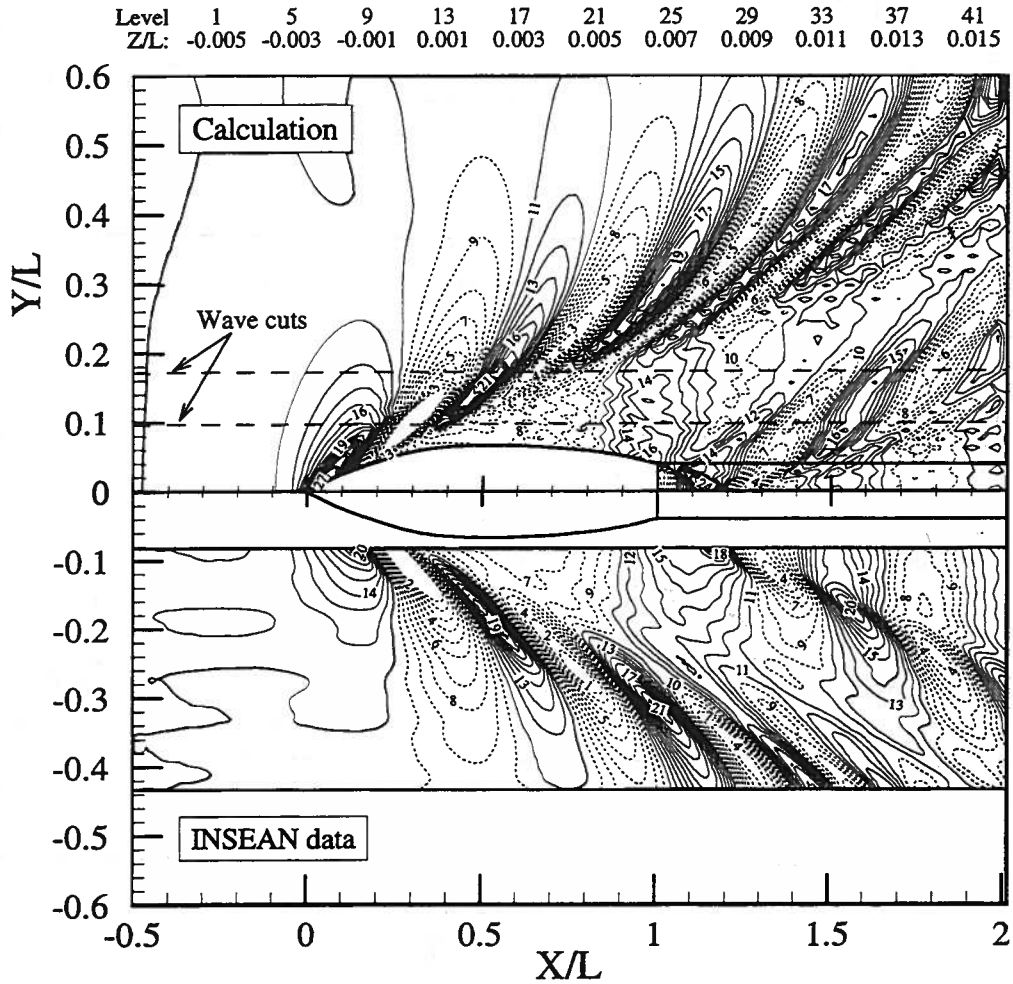
Figure 5.26: Comparison of the wave elevation contours for the DDG5415 model at
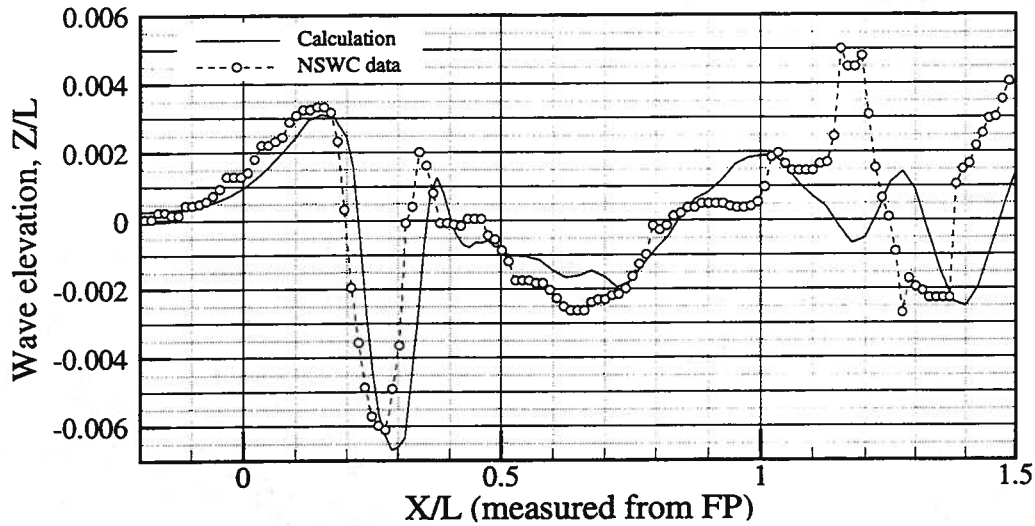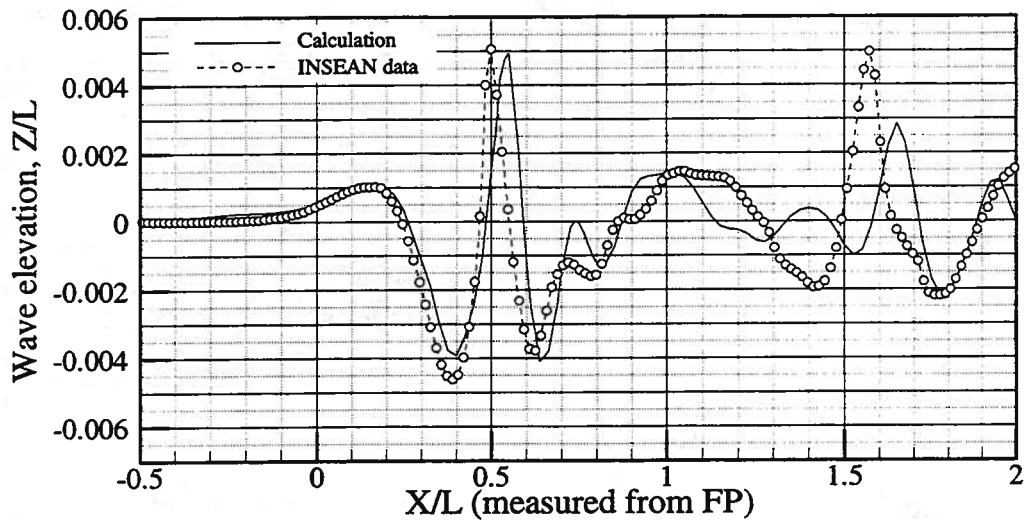
Fr=0.28

Figure 5.27: Validation of the computed wave cuts for the DDG5415 at Fr=0.28

Lastly, the computational requirements for these calculations were as follows. The coarse grid calculation required about 9 MW of memory and 26 minutes (while clocking 248 MFLOPS) on a CRAY SV-1. The medium grid calculation required about 17 MW of memory and 38 minutes (while clocking 350 MFLOPS) on a CRAY T-90.

The fine grid calculation required about 43 MW of memory and 1.88 hours (while clocking 450 MFLOPS) on a CRAY T-90.

5.3.3   Suppression of wave breaking

The next transom stern calculation undertaken was that of the D1 fast monohull at the high Froude number of 0.433. Numerous experiments have been performed, at the Technical University of Berlin, for the D-Series of hull forms at this Froude number. The studies have been part of efforts to evaluate and to optimize hull forms based on the observed hydrodynamic characteristics. Calculations with this additional transom-sterned model were originally undertaken to test the robustness of the method. Interestingly, a preliminary calculation of cleanly separating transom stern flow for the D1 hull at Fr=0.433 showed a very steep, breaking rooster-tail wave crest behind the transom. This provided a suitable case for the testing of the bridging technique in suppressing a three-dimensional breaker (not counting the suppression of spray by the bow).

Calculations were undertaken on a medium-sized body grid consisting of 44 stations. Along a station, the number of nodes corresponded to a density of 12 nodes over a girth equal to the ship draft. The total number of nodes on the body was 901. The dimensions of the numerical wave tank were kept the same as the previously described results. The free-surface discretization for this calculation was 80 nodes in the longitudinal direction and 20 nodes in the transverse direction, with five additional free-surface tracks in the transom wake. The number of free-surface nodes ahead of the body, across the body, and downstream of the body were, respectively, 12, 36, and 32. The total number of free-surface nodes was 1765.

The acceleration parameter, α (in equation 5.2) was taken to be 0.05 again; l_s, the spray zone length parameter was taken to be 1.75, and the time step size chosen was 0.1. Figure 5.28 shows an elevation view of the free-surface at about t=14.7s, shortly before the calculation failed because of numerical problems brought about by the steep, breaking rooster-tail wave crest aft of the transom. Note that the vertical length scale has been exaggerated. Nonetheless, the steepness of the rooster-tail crest is apparent. The calculations were then repeated, but with the turning on of the bridging technique (and the consequent inspection for likely breaking) over each and every one of the free-surface tracks. The two-dimensional curvatures were inspected along each track and incipient breaking faired through. The wave breaking was then successfully suppressed, as also plotted in figure 5.28.

The successful calculation required about 18 MW of memory and about 96 minutes of CPU time on the CRAY-T90, while clocking 324 MFLOPS. Figure 5.29 shows the wave profile on the hull at steady state. For comparison, the available results from the Calypso Project (Nowacki et al., 1999) are also plotted. The Calypso results were obtained using the commercial software, SHIPFLOW (version 2.3), which features a zonal approach consisting of potential flow, boundary layer, and RANS equations calculations. The two sets of results show similar features; however, there exists a slight phase shift between the two calculations—the Calypso calculation of the bow wave crest and the stern shoulder wave trough are a little downstream of the present calculation. Interestingly, notwithstanding the use of the bridging technique at the bow, the present calculation suffers a much less loss of bow wave height than the Calypso calculation apparently does. The differences seen in the wave profile over the stern shoulder region may be the direct effect of differences in the modeling of the transom stern flow. However, information on the transom boundary condition used in the Calypso project's calculations is not available.

Successful suppression of wave breaking
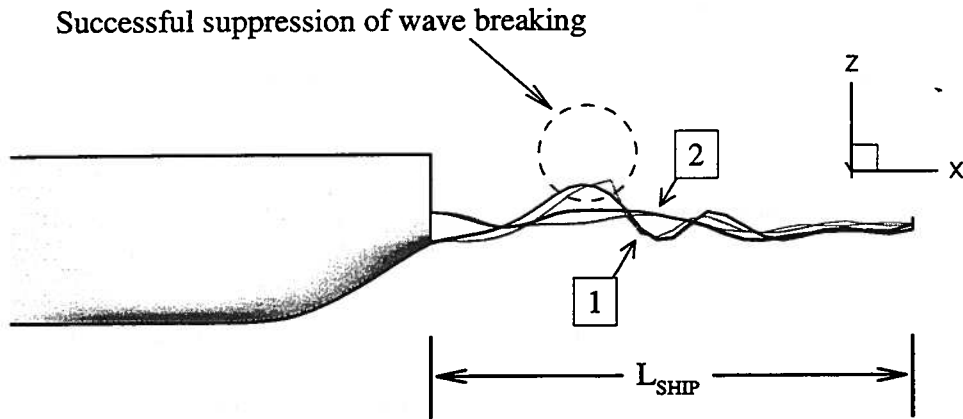
1: Centerline of wake; 2: Outer edge of transom wake

Figure 5.28: Elevation view of the D1 hull at Fr=0.433, showing the breaking

rooster-tail wave crest and its successful suppression
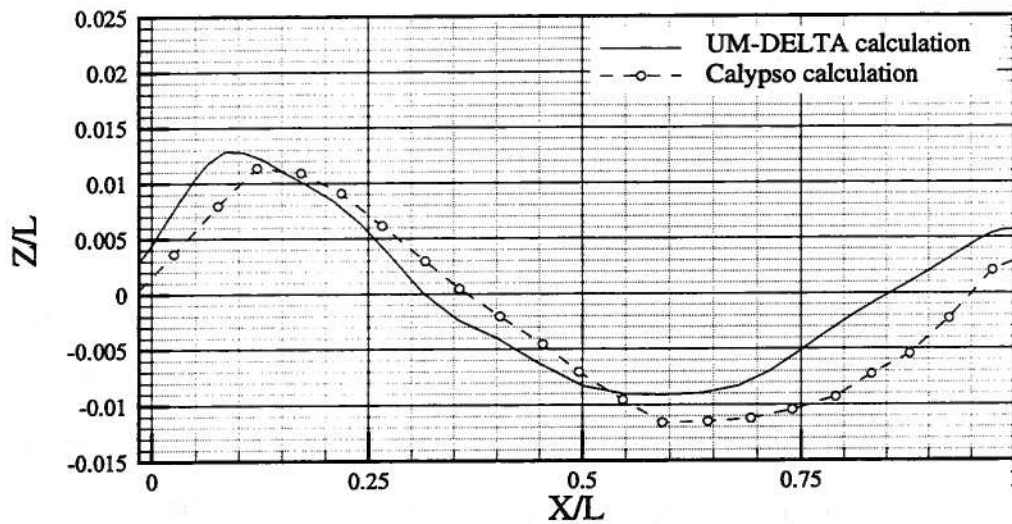
Figure 5.29: Wave profile on the hull for the D1 hull at Fr=0.433

With calm-water calculations for arbitrary and complex hull forms thus successfully enabled within the method, the issues involved in the planned subsequent extension of the method for seakeeping computations were briefly assessed.

5.4. Seakeeping computations

One of the advantages of the UM-DELTA method is that it is a time domain method and, therefore, lends itself easily for seakeeping analysis. The extension of the method for a seakeeping analysis of naval combatant models is also a stated long-term objective of the current research program.

Successful computations using the UM-DELTA method have been performed, in the past, for the forced heave and pitch motions of the modified Wigley hull (Beck et al., 1994) and for the modified Wigley hull in head seas (Scorpio, 1997). Following a successful extension for calm-water calculations for realistic and complex hull forms, the method was tested for a fixed Series 60, C_B=0.6 hull (restrained to float at its design water line) sailing into incident waves.

Calculations were undertaken using a Series 60, C_B=0.6 body grid consisting of 26 stations. The dimensions of the tank were the same as those in the calm-water calculations described in section 5.2.2. The hull was gradually accelerated from rest and first brought to a steady forward speed, at Fr=0.25. The acceleration parameter, α in equation 5.2 was taken to be 0.10, and the time-step size chosen was also 0.10. Once the hull was near its steady forward, at t=25, incident waves were introduced into the three-dimensional numerical wave tank in the form of appropriate boundary conditions at the upstream boundary. This was done using the approach described in Scorpio (1997). The

incident waves had an amplitude of about 0.006 L and a wavelength of about 1.0 L. A snapshot from this successful calculation is presented in figure 5.30.

The calculation cannot, however, be currently performed on finer body grids, because of existing limitations related to body panelization and regridding. In fact, the amplitude of the incident waves in the above calculation was intentionally chosen to be a small 0.006L. The reasons for this choice, and the body regridding issues, are explained with reference to figure 5.31, which shows the panelization of the stern rake.
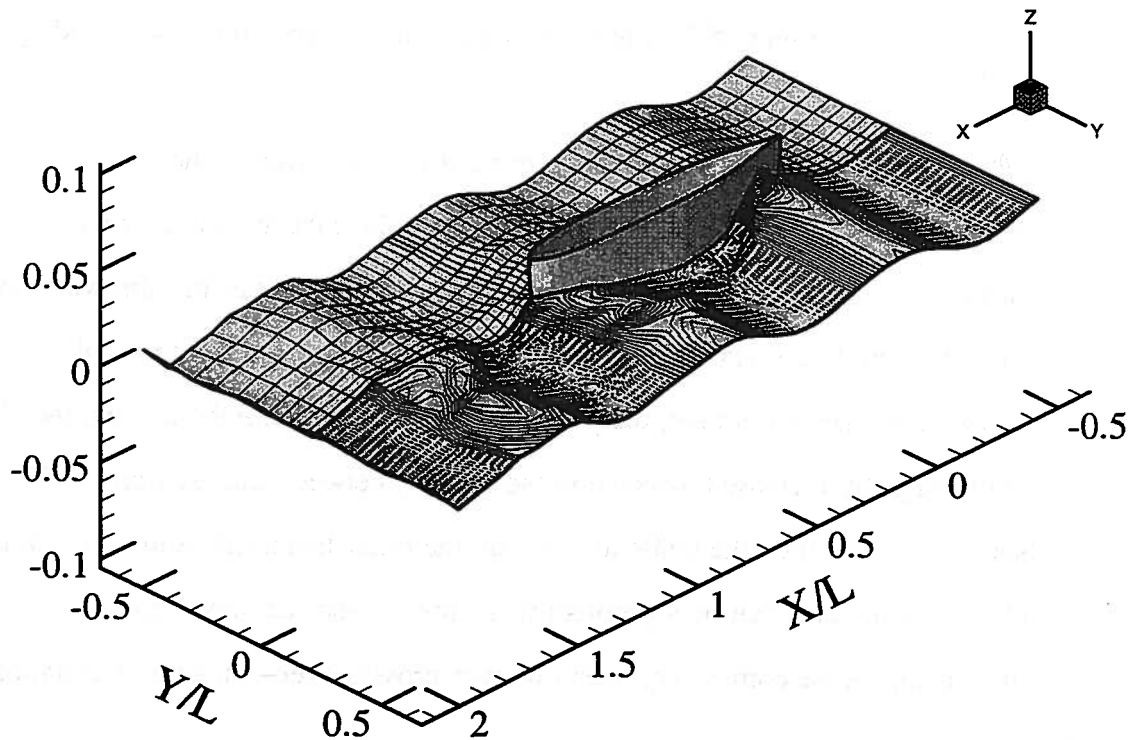
Figure 5.30: Free-surface contours and perspective view of the Series 60, C_B=0.6 advancing into incident waves of amplitude, 0.006L and wavelength, 1.0L
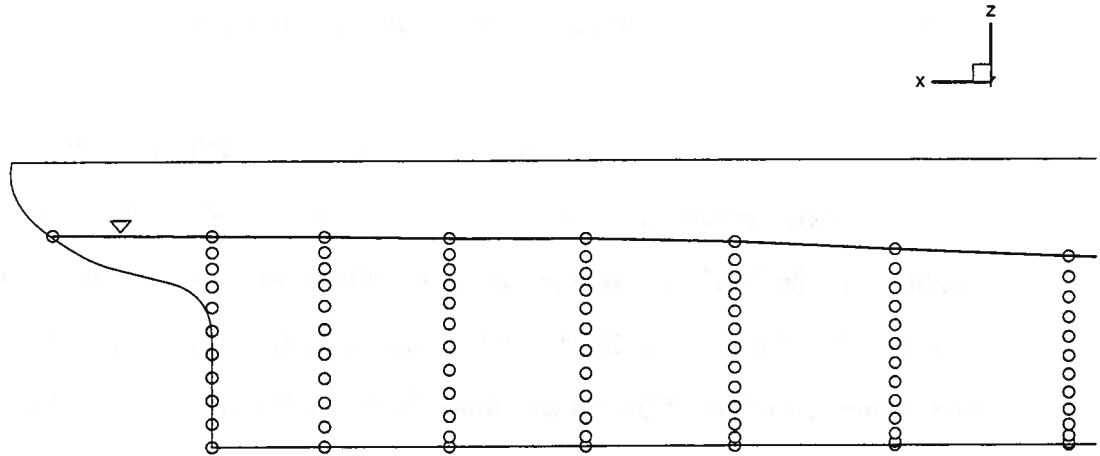
Figure 5.31: Stern rake region of the Series 60, C_B=0.6 body grid

As previously described and apparent from the figure, the stern rake is closed off using a point node that is free to move along the rake in a tracking of the rake–free-surface intersection point. This works without any difficulties in calm-water calculations, for which the free-surface tends to rise along both, the stem and stern rakes. As the free-surface level rises at a rake, the point node there simply climbs up, and the difference is only a slightly increased distance in the spacing between the "stations." When the free-surface level at the rake tends to drop, on the other hand, the point node would have to climb down. This can be a problem when the free-surface level drops to such an extent that the rake node comes very near—or even crosses over—an adjoining station.

For the coarse-grid calculation shown in figure 5.30, the incident wave amplitude and the station spacing in the body grid was such that there was ample room for the stern rake to climb down along the rake without crossing over an adjoining station. This would not, however, be the case were a finer body grid used (as sketched in figure 5.7) or waves of higher amplitude used.

That said, the limitations are chiefly a body-regridding issue. Currently, in the UM-DELTA method the body grid consists of nodes at stations that remain at the same x-location (not counting the point nodes at the rakes). It is possible, of course, to subtract and add body nodes—and even whole stations—if there is a significant immersion or emergence of the hull. What this would entail, however, is an expensive setting up of the matrix preconditioner each time there is a change in the number of body nodes or a change in the number of stations. There is also the issue of additional, complicated body-regridding logic.

A possible solution to these difficulties was briefly explored: the panelization of the body not up to the free-surface but up to the deck. While such an approach may carry the burden of increased computational expenses (on account of an increased number of nodes on the body surface), it would do away with the need for complicated body-regridding logic. The approach was tested for the calculation of incident waves diffracted by a stationary, truncated vertical cylinder and for a modified Wigley hull in calm water. The preliminary calculations for these wall-sided geometries were successful and the approach, consequently, appeared to be promising for seakeeping computations. However, the approach ran into problems next in the case of the Series 60, C_B=0.6 hull form. The problems were on account of the flared cross-sections (in the Y-Z plane) of the hull above the calm-water line and the difficulties in positioning the desingularized sources appropriately.

This exploratory study and the limitations of the body-gridded-upto-deck approach are covered in Appendix E. As discussed therein, the successful extension of the method for seakeeping computations calls for further work on body panelization and

regridding, with particular attention to be given to the placement of the desingularized sources.

CHAPTER 6

CONCLUSIONS AND FUTURE WORK

Fully nonlinear computations in the time domain have been widely performed for marine hydrodynamics problems using the popular Euler-Lagrange approach. The vast majority of applications have, however, been limited to simplified body geometries such as cylinders, spheroids, and the mathematical Wigley hull, or for water wave problems involving no body at all. In addition to geometry modeling, there has existed a major difficulty constraining the calculations of ship hydrodynamic flows: wave breaking. The flow around realistic hull forms are highly nonlinear, and the occurrence of spray and wave breaking are ubiquitous features of such flows. Most of the prevalent methodologies for the study of wave-body interaction problems fail when wave breaking is encountered. With the present work, a desingularized boundary integral method based on the Euler-Lagrange time-domain approach—the UM-DELTA method—has been successfully extended and applied to calm-water calculations for arbitrary and complex hull forms.

Studies on wave breaking, especially on ways to suppress the disruptive occurrence of spray and wave breaking, were reported in Chapter 3. A criterion for the likely occurrence of wave breaking was devised as a means for detecting incipient numerical wave breaking. Once detected, a breaking wave is suppressed though a new, *bridging* technique that simply fairs through the free-surface nodes that are likely to break. The technique was successfully applied to gravity waves in two dimensions and also extended for forward speed calculations, including in three dimensions.

Two-dimensional inviscid transom stern flows were studied in Chapter 4, as a prelude to an undertaking of three-dimensional transom stern computations. Specifically, numerical artifices to effect cleanly-separating transom stern flow within the inviscid flow model were tested. A stable technique was successfully devised and retained for use in three dimensions. The two-dimensional transom stern calculations were also used to study the feasibility of the bridging technique in suppressing wave breaking in forward-speed calculations. Calculations were undertaken (using three different grids, with a doubling in the grid size across the grids) in which a steep, breaking wave was seen aft of the transom stern; the bridging technique was shown to suppress such wave breaking successfully.

Three-dimensional forward-speed calculations for arbitrary and complex hull forms were reported in Chapter 5. The geometry processor that enabled a modeling of realistic hull forms was described. Calm-water results at representative Froude numbers were then presented for the Series 60, C_B=0.6 parent hull (typifying arbitrary hull forms) and for two transom-sterned vessels—the D1 fast monohull and the DDG5415 combatant (which also has a bulbous bow). The calculations were verified through grid convergence and also compared to the available experimental data.

Specifically, the measures adopted for a handling of stagnation points, bilges, bulbous bows, and transom sterns were described. Wave resistance was determined for the Series 60, C_B=0.6 at Fr=0.316 using two different approaches: (a) wholly by an integration of the pressure over the hull, and (b) by incorporating a wedge-flow approximation at the bow and stern. The results agreed well with each other and were also in good agreement with the experimental data. The three-dimensional transom stern calculations featured a successful demonstration of cleanly separating flow, for the

DDG5415 model at Fr=0.28, and grid convergence was also shown. The ability of the bridging technique to suppress wave breaking in three-dimensional forward speed calculations was also shown, through an application to the breaking rooster-tail wave crest seen behind the D1 hull at Fr=0.433.

Future work lies in three main areas. The first lies in the development of an approach to simulate in detail an actual wave breaking event. While the bridging technique is very useful in suppressing most instances of wave breaking adequately and thereby in enabling the fully nonlinear water wave computations to proceed, there are inherent limitations to this approach. When severe wave breaking occurs, the post-breaking flow is influenced in ways that cannot be accurately modeled using the present approach. Moreover, with a model that can resolve breaking waves and spray, the accuracy of the computations may not be compromised – as seen in the computed wave profile along the hull when the bridging technique is used to suppress spray-sheet-related numerical difficulties at the bow and stern. A promising methodology is Smoothed Particle Hydrodynamics, featuring the simulation of discrete fluid particles.

Another area for future research springs from the fact that, while inviscid calculations are useful in the design process, they omit some important features of ship hydrodynamic flows, as was seen in a validation of the computed wave field for the DDG5415 model at Fr=0.28. In order to capture the important viscous effects—while recognizing that the bulk of the flow in the far field is irrotational—a viscous-inviscid interaction approach may be pursued in order to obtain an accurate solution inexpensively. In fact, work on one such approach has already been initiated under the aegis of the present research program. The approach consists of blending the potential flow UM-DELTA solution with a Reynolds-averaged Navier-Stokes equations solution in the near field.

Lastly, in order to realize the full benefits of the inviscid UM-DELTA method as a design tool, further extensions need to be made so that seakeeping computations for complex hull forms are enabled. The placement of sources in the desingularized method had originally been seen by many to be a stumbling block, especially in the case of complex hull forms. However, the use of innovative strategies has helped to overcome the perceived obstacles, in bringing the method to its current state of development. With calm-water calculations successfully realized for practical hull forms, further work is now called for on improved ways to handle body panelization and regridding. Two options appear worthy of consideration:

(1) a further pursuit of the promising "grid body up to the deck" approach tested, but with the incorporation of "intelligent logic" in the positioning of the desingularized sources (intelligent in the sense of a three-dimensional searching of node and source neighbors and vacancies)

(2) the pursuit of a body-regridding scheme that involves the easy adding and dropping of nodes and stations as necessary (with the immersion and emergence of the hull)

Such work would also facilitate the incorporation of a body motion solver.

APPENDICES

APPENDIX A

COMPONENT VELOCITIES OF FREE-SURFACE NODES ALONG A PATH

Consider one of the free-surface paths, as sketched in figure A.1. Let the path be defined by y=f(x). The tangent vector to the path is then

$$\vec{t} = (t_1, t_2) = \left(\frac{1}{\sqrt{1 + (f'(x))^2}}, \frac{f'(x)}{\sqrt{1 + (f'(x))^2}} \right) \tag{A.1}$$

As is evident, this formula would theoretically break down when the path is at 90° to the x-axis; however, the problem is avoided by computing the derivatives using a parametric spline (based on curve length) along the path.
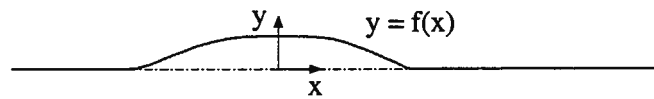
Figure A.1: An illustrative free-surface path

The fluid velocity vector in the X-Y plane is

$$\vec{V} = (U_o + \phi_x, \phi_y) \tag{A.2}$$

The magnitude of the velocity in the path direction is

$$\vec{V} \cdot \vec{t} = \left(U_o + \phi_x\right)t_1 + \phi_y t_2 \tag{A.3}$$

The Cartesian components of the path velocity are then

$$v_x = \left(\left(U_o + \phi_x\right)t_1 + \phi_y t_2\right)t_1$$

$$\tag{A.4}$$

$$v_y = \left(\left(U_o + \phi_x\right)t_1 + \phi_y t_2\right)t_2$$

These are the component velocities with which the free-surface nodes are prescribed to move along their respective paths.

APPENDIX B

CALCULATION OF SPATIAL FREE-SURFACE DERIVATIVES

The spatial free-surface derivatives, $\nabla\eta = \left(\dfrac{\partial\eta}{\partial x}, \dfrac{\partial\eta}{\partial y}\right)$ are computed as follows.

First, free-surface derivatives are computed in the parametric direction, u along each track. Specifically, referring to figure B.1, $\partial\eta/\partial u$ at node i along path j is determined using Lagrange polynomials:

$$\left.\frac{\partial\eta}{\partial u}\right|_{i,j} = \frac{(\eta_{i-1}-\eta_i)(u_{i+1}-u_i)^2 - (\eta_{i+1}-\eta_i)(u_{i-1}-u_i)^2}{(u_{i-1}-u_i)(u_{i+1}-u_i)^2 - (u_{i+1}-u_i)(u_{i-1}-u_i)^2} = F(u_i,\eta_i) \qquad (B.1)$$
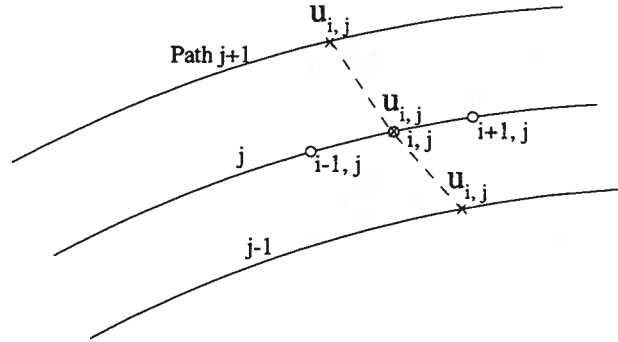
Figure B.1: Computing of free-surface derivatives

Next, on paths, j-1 and j+1, η is determined by interpolation at locations corresponding to the parametric distance, $u_{i,j}$. Let these values by denoted by $\hat{\eta}_{j-1}$ and $\hat{\eta}_{j+1}$, respectively, with the corresponding coordinates being $(\hat{x}_{j-1}, \hat{y}_{j-1})$ and $(\hat{x}_{j+1}, \hat{y}_{j+1})$.

Next, with track j-1 as reference, cross-track distances, v are measured as follows:

$$v_{j-1} = 0.$$

$$v_j = v_{j-1} + \sqrt{(x_{i,j} - \hat{x}_{j-1})^2 + (y_{i,j} - \hat{y}_{j-1})^2} \qquad \text{(B.2)}$$

$$v_{j+1} = v_j + \sqrt{(\hat{x}_{j+1} - x_{i,j})^2 + (\hat{y}_{j+1} - y_{i,j})^2}$$

Next, $\left.\dfrac{\partial \eta}{\partial v}\right|_{i,j} = F(v_j, \eta_j)$ is computed as in (B.1), as are $\partial u/\partial x$, $\partial u/\partial y$, $\partial v/\partial x$, and $\partial v/\partial y$.

Finally, the required derivatives at node (i,j) are computed using:

$$\frac{\partial \eta}{\partial x} = \frac{\partial \eta}{\partial u} \cdot \frac{\partial u}{\partial x} + \frac{\partial \eta}{\partial v} \cdot \frac{\partial v}{\partial x}$$

$$\text{(B.3)}$$

$$\frac{\partial \eta}{\partial y} = \frac{\partial \eta}{\partial u} \cdot \frac{\partial u}{\partial y} + \frac{\partial \eta}{\partial v} \cdot \frac{\partial v}{\partial y}$$

APPENDIX C

CALCULATION OF TWO-DIMENSIONAL CURVATURE USING A LOCAL THREE-POINT FORMULA

If the curvature is required at a free-surface node, consider that node and its two nearest neighbors, as sketched in figure C.1.
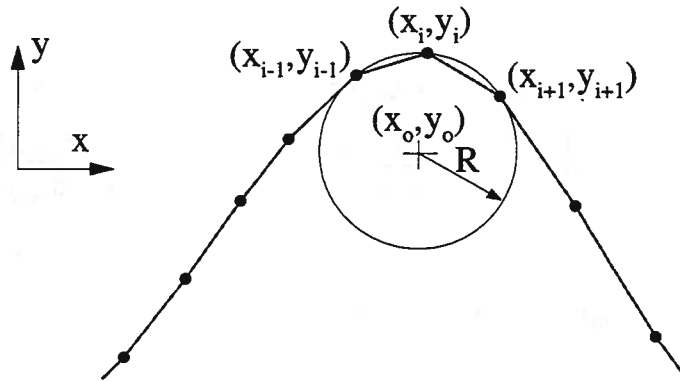
Figure C.1: Fitting of a circle through three consecutive free-surface nodes

The curvature is computed by first determining the radius of the circle that fits through these three consecutive free-surface nodes. The three nodes, (x_{i-1}, y_{i-1}), (x_i, y_i), and (x_{i+1}, y_{i+1}) satisfy the equation of the circle:

$$(x_{i-1} - x_o)^2 + (y_{i-1} - y_o)^2 = R^2$$

$$(x_i - x_o)^2 + (y_i - y_o)^2 = R^2 \tag{C.1}$$

$$(x_{i+1} - x_o)^2 + (y_{i+1} - y_o)^2 = R^2$$

where (x_o, y_o) is the center of the circle and R, the radius.

This system of nonlinear equations was solved for the three unknowns, x_o, y_o, and R using the mathematical software, MAPLE:

$$x_o = \frac{1}{2} \cdot \frac{\begin{aligned}(-x_i^2 y_{i+1} + x_i^2 y_{i-1} - x_{i-1}^2 y_i + x_{i+1}^2 y_i - y_{i-1}^2 y_i + x_{i-1}^2 y_{i+1} \\ + y_i^2 y_{i-1} + y_{i+1}^2 y_i - y_{i+1}^2 y_{i-1} + y_{i-1}^2 y_{i+1} - x_{i+1}^2 y_{i-1} - y_i^2 y_{i+1})\end{aligned}}{-x_i y_{i+1} + x_i y_{i-1} + x_{i-1} y_{i+1} + x_{i+1} y_i - x_{i+1} y_{i-1} - x_{i-1} y_i}$$

$$y_o = -\frac{1}{2} \cdot \frac{\begin{aligned}(x_{i+1} x_{i-1}^2 + x_{i+1} y_{i-1}^2 + x_i x_{i+1}^2 + x_i y_{i+1}^2 - x_i x_{i-1}^2 - x_i y_{i-1}^2 \\ - x_{i+1} y_i^2 - x_{i-1} x_{i+1}^2 - x_{i-1} y_{i+1}^2 - x_{i+1} x_i^2 + x_{i-1} x_i^2 + x_{i-1} y_i^2)\end{aligned}}{-x_i y_{i+1} + x_i y_{i-1} + x_{i-1} y_{i+1} + x_{i+1} y_i - x_{i+1} y_{i-1} - x_{i-1} y_i} \qquad (C.2)$$

$$R = \sqrt{(x_i - x_o)^2 + (y_i - y_o)^2}$$

Finally, the curvature at a node (i,j) other than the end points (the curvature is, in any case, not really needed at the end points) is given by:

$$\kappa_{i,j} = \begin{cases} -\dfrac{1}{R}, \text{if } \dfrac{y_{i+1} - y_{i-1}}{x_{i+1} - x_{i-1}} \le \dfrac{y_i - y_{i-1}}{x_i - x_{i-1}} \\[3mm] +\dfrac{1}{R}, \text{if } \dfrac{y_{i+1} - y_{i-1}}{x_{i+1} - x_{i-1}} > \dfrac{y_i - y_{i-1}}{x_i - x_{i-1}} \end{cases} \qquad (C.3)$$

APPENDIX D

CALCULATION OF WAVE RESISTANCE USING WEDGE-FLOW APPROXIMATION

Consider the bow of the Series 60, C_B=0.6 hull to be a vertical stack of two-dimensional wedges, with the flow past a wedge illustrated in figure D.1 (a). This wedge flow, in the X-Y plane, may be transformed into uniform, free-stream flow in a complex U-V plane [sketched in figure D.1 (b)] using the Schwarz-Christoffel transformation (see, e.g., Hildebrand, 1965, sec. 10.20):

$$z = w^{\frac{\alpha}{\pi}}$$

or   (D.1)

$$w = z^{\frac{\pi}{\alpha}}$$

z-plane   w-plane
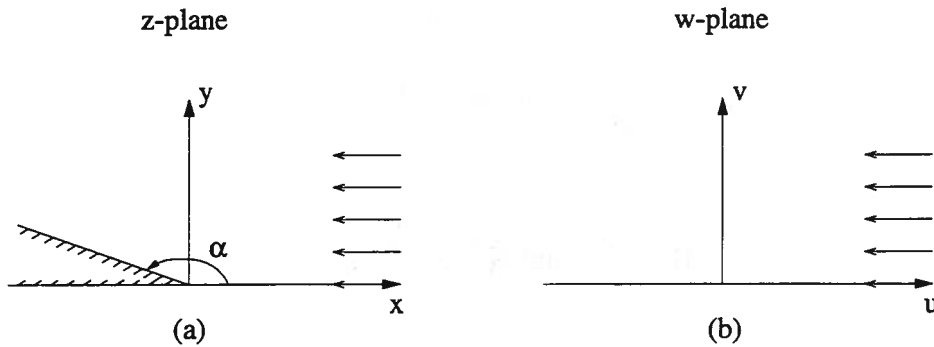
Figure D.1: (a) Uniform flow past a two-dimensional wedge, and (b) its transformation into uniform, free-stream flow in the complex plane

If $z = re^{i\theta}$ and $w = \bar{\rho}e^{i\omega}$, then

$$\bar{\rho} = r^{\frac{\pi}{\alpha}}$$

$$\omega = \frac{\pi\theta}{\alpha} \tag{D.2}$$

The complex potential is then given by

$$T = \phi + i\psi = -U_o w = -U_o z^{\frac{\pi}{\alpha}} \tag{D.3}$$

and the complex velocity is

$$\frac{dT}{dz} = u - iv = -U_o \frac{\pi}{\alpha} z^{\frac{\pi}{\alpha}-1} \tag{D.4}$$

That is,

$$u = -U_o \frac{\pi}{\alpha} r^{\frac{\pi}{\alpha}-1} \cos\left(\theta(\frac{\pi}{\alpha}-1)\right)$$

$$v = U_o \frac{\pi}{\alpha} r^{\frac{\pi}{\alpha}-1} \sin\left(\theta(\frac{\pi}{\alpha}-1)\right) \tag{D.5}$$

These velocities may then be used in an integration of the fluid pressure over the wedge. As previously described (in sec. 5.2.2.3), the components in equation (2.11) that were difficult to estimate accurately using a regular pressure integration were $\frac{1}{2}|\nabla\phi|^2$ and

$U_o \dfrac{\partial \phi}{\partial x}$. (The third term involving $\dfrac{\partial \phi}{\partial x}$, in $\bar{v}.\nabla\phi$, was too small in magnitude to be of any

significance.) It is these terms that were then integrated analytically, as follows.

$$\frac{\partial \phi}{\partial x} = u - U_o = U_o \left(\frac{\pi}{\alpha} r^{\frac{\pi}{\alpha}-1} \cos\left(\theta(\frac{\pi}{\alpha}-1) \right) - 1 \right) \tag{D.6}$$

such that

$$\frac{1}{2}|\nabla\phi|^2 + U_o \frac{\partial \phi}{\partial x} = \frac{1}{2}(u^2 + v^2) - \frac{1}{2}U_o^2 \tag{D.7}$$

Using equation (2.13), the resistance due to these pressure components is then

$$F = \rho \int\limits_{z=-T}^{\eta} dz \int\limits_{r=0}^{R} \frac{1}{2} U_o^2 \left(\left(\frac{\pi}{\alpha} \right)^2 r^{2\left(\frac{\pi}{\alpha}-1\right)} - 1 \right) n_j dr \tag{D.8}$$

This integration was carried out over the portion of the Series 60, C_B=0.6 hull's

bow extending from the forward perpendicular to the second station, as sketched in figure

5.16. A similar integration was carried out for the wedge-like portion at the stern.

APPENDIX E

PANELIZATION OF BODY SURFACE UP TO THE DECK

In this study, calculations were undertaken (with due modifications to the method) with the body surface gridded up to the deck. This approach was first tested for the calculation of incident waves diffracted by a stationary, vertical cylinder and subsequently for three-dimensional forward-speed calculations.

E.1   Wave diffraction by a vertical cylinder

Wave loads on a vertical cylinder have been computed using the UM-DELTA method by Scorpio and Beck (1998). The formulation of this problem is as described in Chapter 2, and the calculation is performed in a manner similar to that described in section 5.4. The problem set up is sketched in figure E.1.
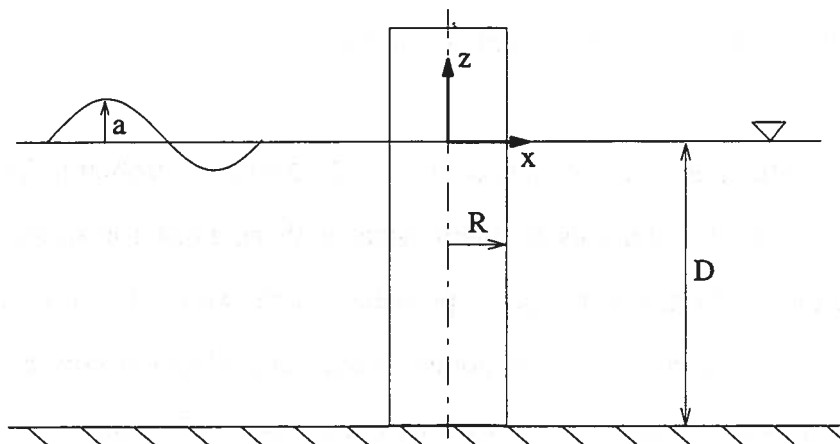

Figure E.1: Problem set-up: wave diffraction by a vertical cylinder

Calculations were initiated for two cases: one in which the problem was tackled in the usual way (with the body gridded up to the free surface) and another in which the problem had a body that was gridded up to the deck. In the first problem, the number of nodes along the body's draft (10 m) was 18. In the second problem, the body was gridded up to a deck that was at two meters above the calm-water level. The number of nodes along the body in the z-direction for this problem was set at 27. In either problem, however, the body grid consisted of 11 stations. Therefore, the total number of body nodes in the two problems were 198 and 297 respectively.

The dimensions of the tank and the size of the free-surface grid were the same for either problem and were as follows. The upstream boundary was two body lengths (the body length being 2 m) upstream, the downstream boundary was 3.5 body lengths downstream, and the tank (the simulation being restricted to the half domain, Y>0) was two body lengths wide. The free-surface grid consisted of 54 nodes in the longitudinal direction and 15 nodes in the transverse direction (total of 810 nodes). This was distributed as: 16 free-surface nodes upstream of the body, 11 nodes across the body length, and 27 nodes downstream of the body.

The time-step size chosen was 0.125 for either problem. The bridging technique was not invoked for this problem, what with no need for suppressing spray or wave breaking. (In the zero-speed problem, there were also no numerical instabilities encountered at the stagnation points as encountered at the bow and stern in a forward-speed problem.) Apart from how the body was gridded, there was one main difference between the two problems, and this was in the placement of the desingularized sources for free-surface nodes on the innermost track (the track that wraps around the body). Usually, the sources are desingularized such that they have the same x and y locations as

their respective nodes. For the case in which the body gridded up to the deck, there would arise the problem of free-surface sources colliding with the body nodes that lie above the free-surface level. Therefore, alternative locations would have to be found for the sources on the innermost track. The solution adopted was simply to displace the sources outward at little, by 20% of the node spacing in the transverse direction.

The calculations using the two different approaches are illustrated in figure E.2, which shows the perspective view of the free-surface at $t=10$. (Note that the scale has been exaggerated in the z-direction.) Not only does the body-gridded-upto-deck approach result in a stable numerical simulation, the results compare with the usual approach to almost graphical accuracy, as shown in figure E.3. It is important, though, to note that the number of nodes along the draft had to be sufficiently large (in the case of a body gridded up to the deck) to enable a successful calculation. This is because, with no body nodes necessarily along the body–free-surface intersection line, the node density in the vertical direction would have to be fine enough for the right boundary condition to be induced along the body–free-surface intersection line. Nevertheless, the burden of 99 extra body nodes in the second problem resulted in an increase in computational expenses of only about 2 minutes on a CRAY-T90 (while the method clocked close to 500 MFLOPS).
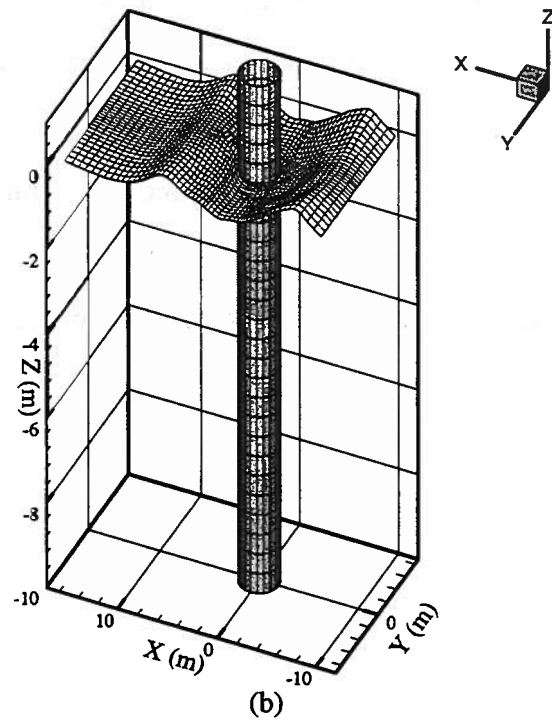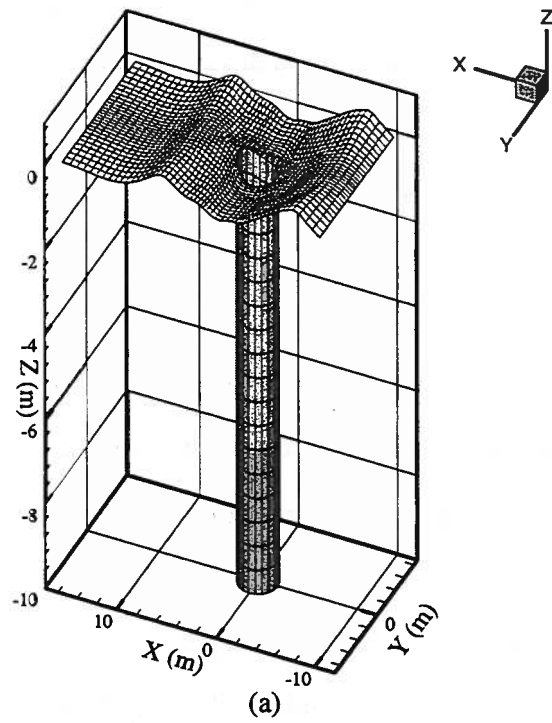
Figure E.2: Perspective view of the free-surface at t=10 for incident waves diffracted by a vertical cylinder gridded up to: (a) the free-surface; (b) the deck
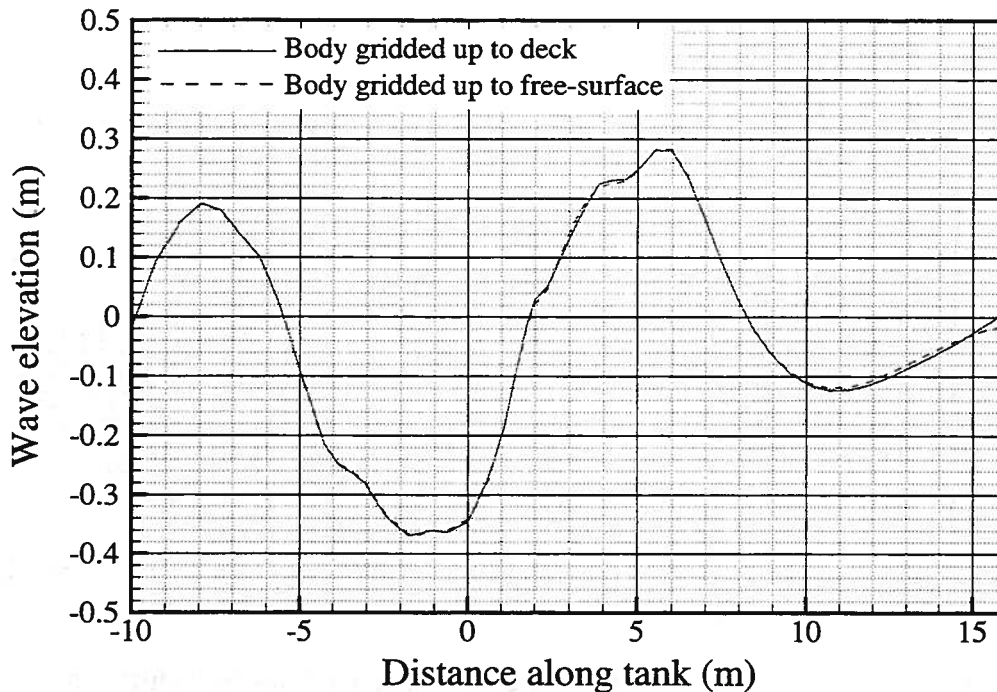
Figure E.3: Comparison of calculations obtained with cylinder gridded up to the free surface and up to the deck: wave profile on the body

E.2 Three-dimensional forward-speed calculations

Following the successful test for the zero-speed problem, the new approach of gridding the body up to the deck was tested for the three-dimensional forward-speed problem. Again, however, the calm-water calculations were first tested on the Wigley hull, which is wall-sided above the design water line, before a test on the Series 60, C_B=0.6 parent hull. One variation adopted in the test on the Wigley hull was that the hull was shifted downward by a small amount. For a Wigley hull whose design water line is at z/L=0, the keel is at z/L=–0.0625; in the present case, the hull was immersed to float at the z/L=0.0175 line in calm water (the keel was at –0.08). This was done so that the

tested approach benefited from a true wall-sided nature at the level of the free-surface, as would be apparent from figure E.4.
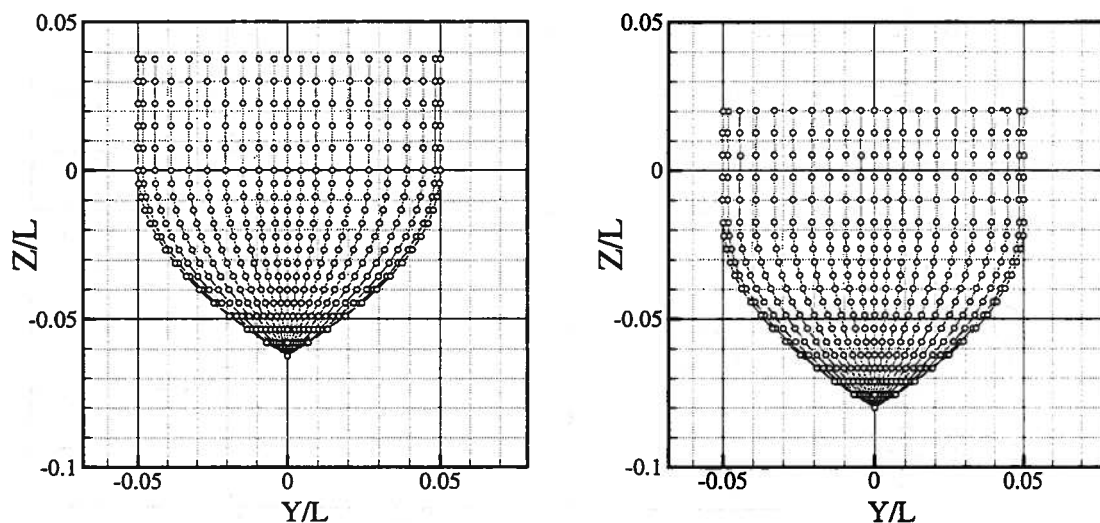
Figure E.4: Body plan for the Wigley hull and a Wigley hull shifted downward by z=0.0175L

As in the previous test, the free-surface sources along the innermost track were displaced outward from the tracks by a small amount. As before, calculations were undertaken using both approaches (at Fr=0.30): a hull gridded up to the free surface and a hull gridded up to the deck (here, 0.02L). A 21-stationed Wigley hull grid was used for either calculation. A node density of 16 nodes for a girth equal to the draft was used; as a result, the total number of nodes on the body was 366 for the first problem and 437 for the second. The free-surface grid consisted of 45 nodes in the longitudinal direction and nine nodes in the transverse direction (a distribution of 10 nodes ahead of the hull, 20 nodes along the hull, and 15 nodes downstream of the hull).

The adequacy of the vertical node density in inducing the right boundary condition on the hull is indicated in figure E.5, which shows the computed perturbation velocities along the hull using the two approaches to compare well.
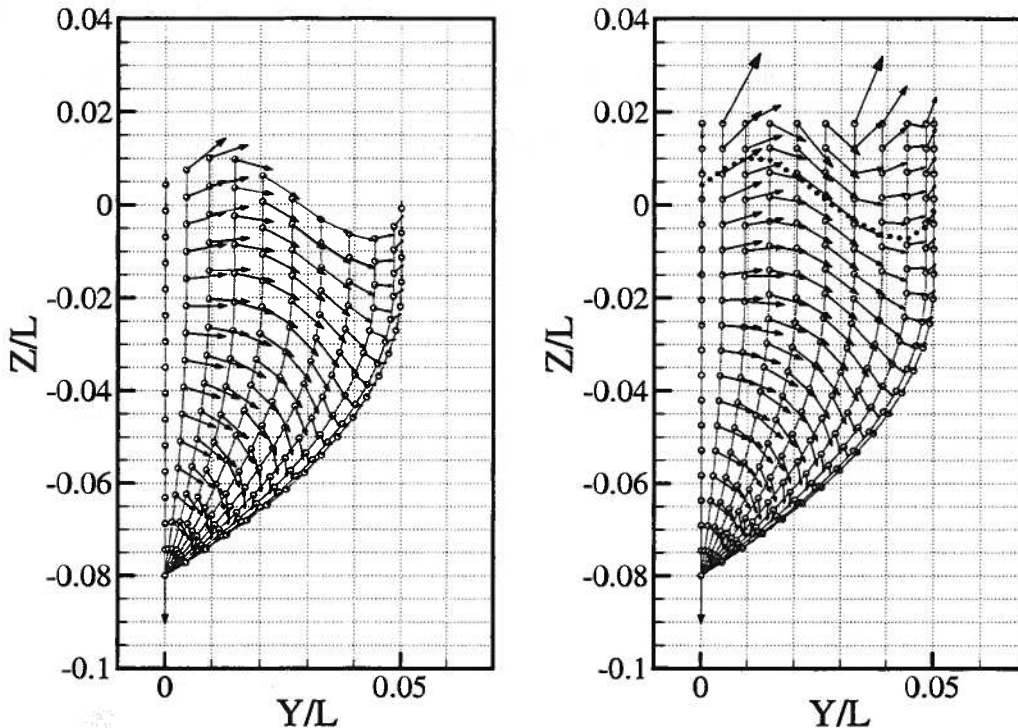
Figure E.5: Comparison of computed perturbation velocities along the hull: (a) Wigley gridded up to the free surface, (b) Wigley gridded up to the deck

A comparison of the steady-state wave profile on the hull (at t=25, with the acceleration parameter and time step both being 0.1) is presented in figure E.6. Again, the solutions compare well, although there is a slight underprediction of the bow wave trough when the hull is gridded up to the deck. Both calculations required a little over 10 minutes on a CRAY T-90; however, the first calculation was performed while the supercomputer clocked 318 MFLOPS, while the second calculation was done at 368 MFLOPS. In effect, the larger problem resulted in a 15% increase in CPU time.

This approach, thus, showed much promise for seakeeping computations. However, it ran into difficulties in the case of the Series 60, C_B=0.6 hull form. Unlike the Wigley hull which is wall-sided above the design water line, the Series 60, C_B=0.6 has a noticeable amount of flare in the forward region and – the troublesome part – a considerable flare at the stern. What the flare does is to take away the room that would have existed for a "safe" positioning of the innermost free-surface track's sources. This is illustrated in figure E.7.
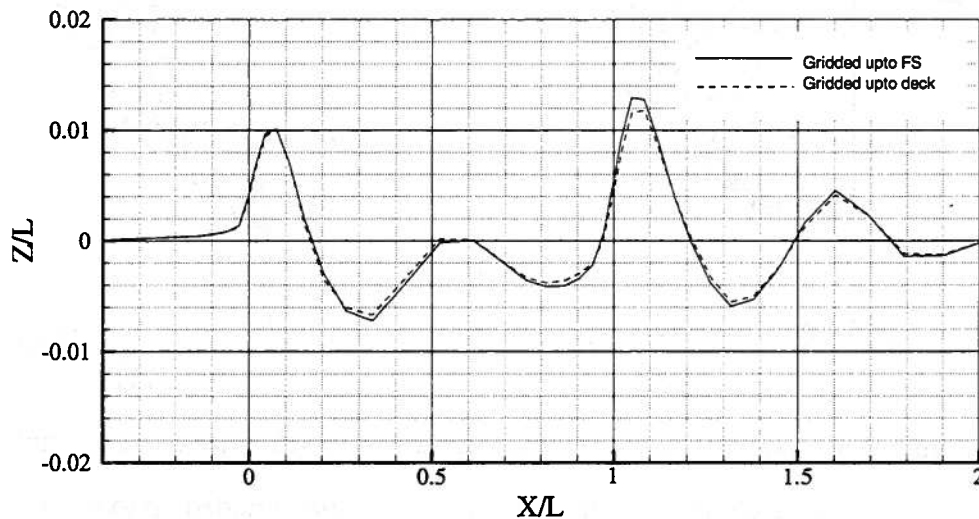
Figure E.6: Comparison of the steady-state wave profile for a modified Wigley hull at Fr=0.30: (a) hull gridded up to the free surface, (b) hull gridded up to the deck

The figure shows a plan view of a 26-stationed Series 60, C_B=0.6 hull that has nodes (represented as hollow circles in the figure) distributed up to the deck. Also shown is the free-surface grid, with the free-surface nodes at the intersection points of the mesh. Due care needs to be given, within the UM-DELTA method, to position the sources such that they do not coincide with or lie very close to each other or collocation points.

However, notice that, in the stern region the body nodes extend outward (in the transverse direction) to as far as the second free-surface track. This makes it very difficult to position the innermost free-surface track's sources by simply displacing it outward by a small amount. As a possible alternative, these sources were raised upward – instead of being displaced outward – to a level safely above the body nodes and sources. However, a stable arrangement of nodes and sources was difficult to realize for this problem, for the calculations failed as a result of numerical instabilities.

Figure E.7: Relative positions of the body and free-surface nodes for a Series 60 hull gridded up to the deck

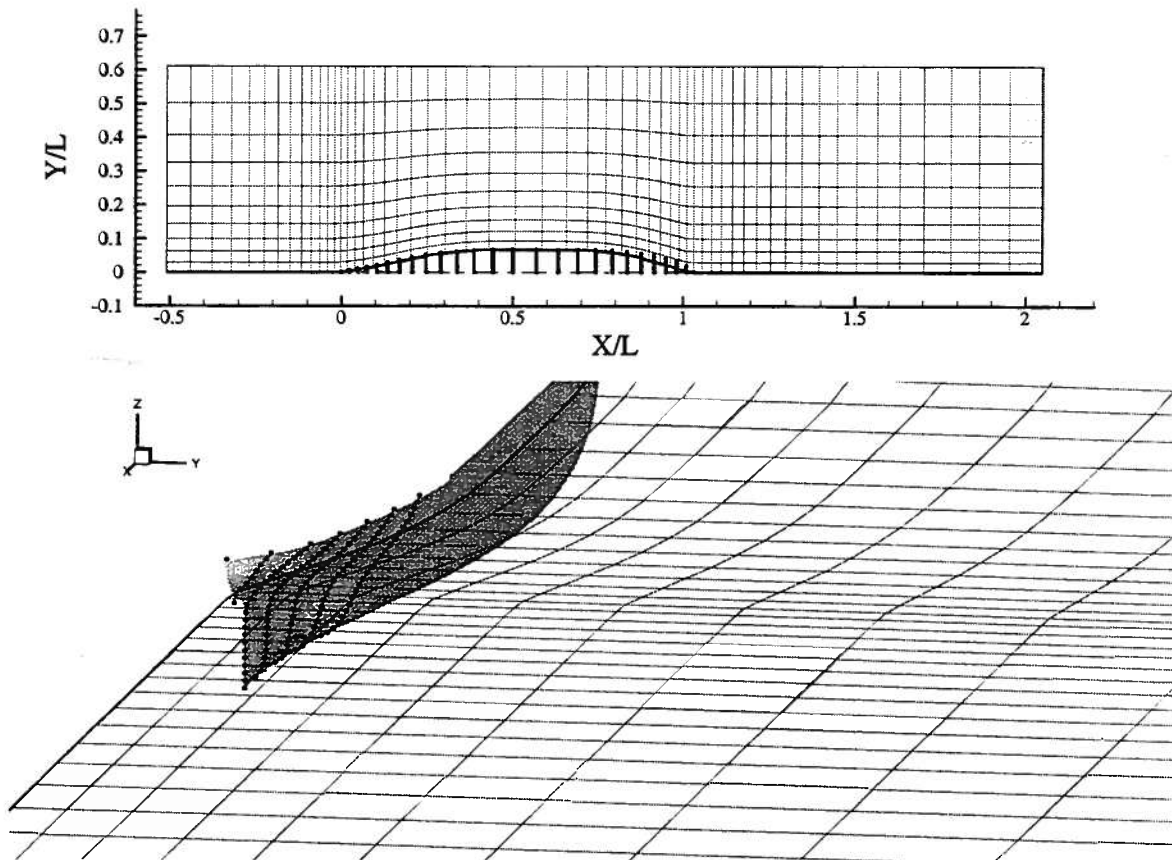This calls for further studies, as research continues on the extension of the method into a viable seakeeping analysis tool for the ship designer.

REFERENCES

REFERENCES

Baker, G.R., Meiron, D.I., and Orszag, S.A., "Generalized Vortex Methods for Free-Surface Flow Problems," Journal of Fluid Mechanics, Vol. 123, 1982, pp. 477–501.

Beck, R.F., "Fully Nonlinear Water Wave Computations Using a Desingularized Euler-Lagrange Time-Domain Approach," Nonlinear Water Wave Interaction, International Series on Advances in Fluid Mechanics, U.K., 1998.

Beck, R.F., Cao, Y., Scorpio, S.M., and Schultz, W.W., "Nonlinear Ship Motion Computations Using the Desingularized Method," Proceedings, 20th Symposium on Naval Hydrodynamics, Santa Barbara, California, 1994, pp. 227–246.

Bonmarin, P., "Geometric Properties of Deep-Water Breaking Waves," Journal of Fluid Mechanics, Vol. 209, 1989, pp. 405-433.

Cao, Y., Schultz, W.W., and Beck, R.F., "Three-Dimensional Desingularized Boundary Integral Methods for Potential Problems," International Journal for Numerical Methods in Fluids, Vol. 12, 1991, pp. 785–803.

Cao, Y., Beck, R.F., and Schultz, W.W., "Numerical Computations of Two-Dimensional Solitary Waves Generated by Moving Disturbances," International Journal of Numerical Methods in Fluids, Vol. 17, 1993, pp. 905–920.

Cao, Y., Beck, R.F., and Schultz, W.W., "An Absorbing Beach for Numerical Simulations of Nonlinear Waves in a Wave Tank," Proceedings, 8th International Workshop on Water Waves and Floating Bodies, Newfoundland, Canada, 1993b.

Celebi, M.S. and Beck, R.F., "Geometric Modeling of Fully Nonlinear Ship-Wave Interactions," Journal of Ship Research, Vol. 41, No. 1, 1997, pp. 17–25.

Celebi, M.S., Kim, M.H., and Beck, R.F., "Fully Nonlinear 3-D Numerical Wave Tank Simulation," Journal of Ship Research, Vol. 42, No. 1, 1998, pp. 33–45.

CFD Workshop Tokyo, Proceedings, Vol. 1 and 2, Ship Research Institute, Ministry of Transport, Ship and Ocean Foundation, Japan, 1994.

Chan, J.L.K. and Calisal, S.M., "A Numerical Procedure for Time Domain Nonlinear Surface Waves Calculations," Ocean Engineering, Vol. 20, No. 1, 1993, pp. 19–32.

Cointe, R., Geyer, P., King, B., Molin, B., and Tramoni, M., "Nonlinear and Linear Motions of a Rectangular Barge in a Perfect Fluid," Proceedings, 18th Symposium on Naval Hydrodynamics, Ann Arbor, Michigan, 1990, pp. 85–99.

DiMascio, A., Landrini, M., Lalli, F., and Bulgarelli, U., "Three-Dimensional Nonlinear Diffraction Around a Fixed Structure," Proceedings, 20th Symposium on Naval Hydrodynamics, Santa Barbara, California, 1994, pp. 477–486.

Dommermuth, D.G. and Yue, D.K.P., "Numerical Simulations of Nonlinear Axisymmetric Flows With a Free Surface," Journal of Fluid Mechanics, Vol. 178, 1987, pp. 195–219.

Faltinsen, O.M., "Numerical Solution of Transient Nonlinear Free-Surface Motion Outside or Inside Moving Bodies," Proceedings, 2nd Conference on Numerical Ship Hydrodynamics, Berkeley, California, 1977, pp. 347–357.

Gentaz, L., Guillerm, P.E., Alessandrini, B., and Delhommeau, G., "Three-Dimensional Free-Surface Viscous Flow Around a Ship in Forced Motion," Proceedings, 7th International Conference on Numerical Ship Hydrodynamics, Nantes, France, 1999.

Gothenburg 2000: A Workshop on CFD in Ship Hydrodynamics, http://www.iihr.uiowa.edu/gothenburg2000, Gothenburg, Sweden, 14–16 September, 2000.

Greaves, D.M., Borthwick, A.G., Wu, G.X., and Eatock-Taylor, R., "A Moving Boundary Finite Element Method for Fully Nonlinear Wave Simulations," Journal of Ship Research, Vol. 41, No. 3, 1997, pp. 181–194.

Griffin, O., Peltzer, R., Wang, H., and Schultz, W., "Kinematic and Dynamic Evolution of Deep Water Breaking Waves," Proceedings, 20th Symposium on Naval Hydrodynamics, Santa Barbara, California, 1994.

Grosenbaugh, M.A. and Yeung, R.W., "Nonlinear Bow Flows – An Experimental and Theoretical Investigation," Proceedings, 17th Symposium on Naval Hydrodynamics, The Hague, The Netherlands, 1998, pp. 195–214.

Grue, J., Bjorshol, G., and Strand, O., "Higher Harmonic Wave Exciting Forces on a Vertical Cylinder," Pre-Print Series, Department of Mathematics, University of Oslo, 1993.

Haussling, H.J., "Two-Dimensional Linear and Nonlinear Stern Waves," Journal of Fluid Mechanics, Vol. 97, part 4, 1980, pp. 759-769.

Haussling, H.J. and Coleman, R.M., "Nonlinear Water Waves Generated by an Accelerated Circular Cylinder," Journal of Fluid Mechanics, Vol. 92, part 4, 1979, pp. 767–781.

Haussling, H.J., Miller, R.W., and Coleman, R.M., "Computation of High-Speed Turbulent Flow About a Ship Model With a Transom Stern," Proceedings, ASME Fluids Engineering Division Summer Meeting, Vancouver, Canada, 1997.

Hildebrand, F.B., "Advanced Calculus for Applications," Prentice-Hall, 1965.

Jensen, G., Bertram, V., and Soding, H., "Ship Wave-Resistance Computations," Proceedings, 5th International Conference on Numerical Ship Hydrodynamics, Hiroshima, Japan, 1989, pp. 593–606.

Kang, C.-G. and Gong, I.Y., "A Numerical Solution Method for Three-Dimensional Nonlinear Free Surface Problems," Proceedings, 18th Symposium on Naval Hydrodynamics, Ann Arbor, Michigan, 1990, pp. 427–438.

Kim, Y.-H and Jenkins, D., "Trim and Sinkage Effects on Wave Resistance With Series 60, C_B=0.6," DTNSRDC Report/SPD-1013-01, September, 1981.

Kim, Y.-H and Lucas, T., "Nonlinear Ship Waves," Proceedings, 18th Symposium on Naval Hydrodynamics, Ann Arbor, Michigan, 1990, pp. 439–452.

Kim, Y.-H. and Lucas, T., "Nonlinear Effects on High Block Ship at Low and Moderate Speed," Proceedings, 19th Symposium on Naval Hydrodynamics, Seoul, Korea, 1992, pp. 43–52.

Larsson, L., Patel, V.C., and Dyne, G., "Ship Viscous Flow—Proceedings of the 1990 SSPA-CTH-IIHR Workshop," FLOWTECH International Report No. 2, 1991.

Lin, W.M., Newman, J.M., and Yue, D.K., "Nonlinear Forced Motions of Floating Bodies," Proceedings, 15th Symposium on Naval Hydrodynamics, Hamburg, Germany, 1984, pp. 33–49.

Longo, J. and Stern, F., "Yaw Effects on Model-Scale Ship Flows," Proceedings, 21st Symposium on Naval Hydrodynamics, Trondheim, Norway, 1996, pp. 312–327.

Longo, J. and Stern, F., "Resistance, Sinkage and Trim, Wave Profile, and Nominal Wake and Uncertainty Assessment for DTMB Model 5512," Proceedings, 25th American Towing Tank Conference, Iowa City, Iowa, 1998.

Longuet-Higgins, M.S. and Cokelet, E.D., "The Deformation of Steep Surface Waves on Water: I. A Numerical Method of Computation," Proceedings, Royal Society of London, Vol. A350, 1976, pp. 1–26.

Nowacki, H., Fliege, F., Zimmermann, S.-H., and Prieske, H., "D 1.4.2 Simple Shapes," Deliverable Report D 1.4.2 for Brite EuRam III BRPR-CT96-0208 (BE95-1721), Reference No. 980515-1, Technical University of Berlin, Berlin, 1999.

Olivieri, A. and Penna, R., "Uncertainty Assessment in Wave Elevation Measurements," Proceedings, ISOPE'99, Brest, France, 1999.

Park, J.-H. and Troesch, A.W., "Numerical Modeling of Short-Time Scale Nonlinear Water Waves Generated by Large Vertical Motions of Non-Wallsided Bodies," Proceedings, 19th Symposium on Naval Hydrodynamics, Seoul, Korea, 1992.

Ratcliffe, T., "Validation of Free Surface Reynolds Averaged Navier Stokes and Potential Flow Codes," Proceedings, 22nd Symposium on Naval Hydrodynamics, Washington, D.C., 1998, pp. 964–980

Raven, H.C., "A Practical Nonlinear Method for Calculating Ship Wavemaking and Wave Resistance," Proceedings, 19th Symposium on Naval Hydrodynamics, 1992, pp. 349–370.

Saad, Y. and Schultz, M.H., "GMRES: A Generalized Minimal Residual Algorithm for Solving Nonsymmetric Linear Systems," SIAM Journal of Scientific and Statistical Computing, Vol. 7, 1986, pp. 856–869.

Schultz, W.W. and Hong, S.W., "Solution of Potential Problems Using an Overdetermined Complex Boundary Integral Method," Journal of Computational Physics, No. 84, 1989, pp. 414–440.

Scorpio, S.M., "Fully Nonlinear Ship-Wave Computations Using a Multipole Accelerated, Desingularized Method," Ph.D. Dissertation and Report No. 334, Department of Naval Architecture and Marine Engineering, University of Michigan, 1997.

Scorpio, S.M. and Beck, R.F., "Two-Dimensional Inviscid Transom Stern Flow," Proceedings, 12th International Workshop on Water Waves and Floating Bodies, Carry-le-Rouet, France, 1997.

Scorpio, S.M. and Beck, R.F., "A Multipole Accelerated Desingularized Method for Computing Nonlinear Wave Forces on Bodies," Journal of Offshore Mechanics and Arctic Engineering, 1998.

Scorpio, S.M., Beck, R.F., and Korsmeyer, F.T., "Nonlinear Water Wave Computations Using a Multipole Accelerated, Desingularized Method," Proceedings, 21st Symposium on Naval Hydrodynamics, Trondheim, Norway, 1996, pp. 69–74.

Scullen, D.C., "Accurate Computation of Steady Nonlinear Free-Surface Flows," Ph.D. Thesis, Department of Applied Mathematics, University of Adelaide, 1998.

Scullen, D.C. and Tuck, E.O., "Nonlinear Free-Surface Flow Computations for Submerged Cylinders," Journal of Ship Research, Vol. 39, No. 3, 1995, pp. 185–193.

Sen, D., "Numerical Simulation of Motions of Two-Dimensional Floating Bodies," Journal of Ship Research, Vol. 37, No. 4, 1993, pp. 307–330.

Stern, F., Longo, J.F., Zhang, Z., and Subramani, A.K., "Detailed Bow-Flow Data and CFD for a Series 60, C_B=0.6 Ship Model at Froude Number 0.316," Journal of Ship Research, Vol. 40, No. 3, 1996, pp. 193–199.

Subramani, A.K. and Beck, R.F., "Suppression of Wave Breaking in Nonlinear Water Wave Computations Including Forward Speed," Proceedings, 15th International Workshop on Water Waves and Floating Bodies, Caesarea, Israel, 2000, pp. 170–173.

Subramani, A.K., Beck, R.F., and Schultz, W.W., "Suppression of Wave-Breaking in Nonlinear Water Wave Computations," Proceedings, 13th International Workshop on Water Waves and Floating Bodies, Alphen aan den Rijn, The Netherlands, 1998a, pp. 139–142.

Subramani, A., Beck, R., and Scorpio, S., "Fully Nonlinear Free-Surface Computations for Arbitrary and Complex Hull Forms," Proceedings, 22nd Symposium on Naval Hydrodynamics, Washington, D.C., 1998b, pp. 390–402.

Subramani, A.K., Paterson, E.G., and Stern, F., "CFD Calculation of Sinkage and Trim," Journal of Ship Research, Vol. 44, No. 1, 2000, pp. 59–82.

Toda, Y., Stern, F., and Longo, J., "Mean-Flow Measurements in the Boundary Layer and Wake and Wave Field of a Series 60, C_B=0.6 Ship Model – part 1: Froude Numbers 0.16 and 0.316," Journal of Ship Research, Vol. 36, No. 4, 1992, pp. 360–377.

Todd, F.H., "Series 60 – Methodical Experiments with Models of Single-Screw Merchant Ships," Report No. 1712, David Taylor Model Basin, Washington, D.C., 1963.

Vanden-Broeck, J.-M., "Nonlinear Stern Waves," Journal of Fluid Mechanics, Vol. 96, No. 3, 1980, pp. 603–611.

Vanden-Broeck, J.-M. and Tuck, E.O., "Computation of Near-Bow or Stern Flows, Using a Series Expansion in the Froude Number," Proceedings, 2nd International Conference on Numerical Ship Hydrodynamics, Berkeley, California, 1977, pp. 371–381.

Vinje, T. and Brevig, P., "Nonlinear Ship Motions," Proceedings, 3rd International Symposium on Numerical Ship Hydrodynamics, Paris, France, 1981, pp. 257–268.

Wang, P., Yao, Y., and Tulin, M.P., "Wave Group Evolution, Wave Deformation, and Breaking: Simulations Using LONGTANK, a Numerical Wave Tank," International Journal of Offshore and Polar Engineering, Vol. 4, No. 2, 1994.

Wu, G.-X. and Eatock-Taylor, R., "Transient Motion of a Floating Body in Steep Water Waves," 11th International Workshop on Water Waves and Floating Bodies, Hamburg, Germany, 1996.

Wu, G.-X., Ma, Q.-W., and Eatock-Taylor, R., "Analysis of Interactions Between Nonlinear Waves and Bodies by Domain Decomposition," Proceedings, 21st Symposium on Naval Hydrodynamics, Trondheim, Norway, 1996, pp. 110–119.

Xu, H. and Yue, D., "Computations of Fully Nonlinear Three Dimensional Water Waves," Proceedings, 19th Symposium on Naval Hydrodynamics, Seoul, Korea, 1992, pp. 177–201.

Zhou, Z. and Gu, M., "A Numerical Research of Nonlinear Body-Wave Interactions," Proceedings, 18th Symposium on Naval Hydrodynamics, Ann Arbor, Michigan, 1990, pp. 103–118.